DOE/NV/13609-54
DOE M/1522 2007

Tritium Transport at the Rulison Site, a Nuclear-Stimulated Low-Permeability Natural Gas Reservoir

Publication No. 45224

September 2007

U.S. Department of Energy

Office of Legacy Management

Work Performed Under DOE Contract Numbers DE-AC01-02GJ79491, DE-AC52-00NV13609, and DE-AC52-06NV26383 for the U.S. Department of Energy Office of Legacy Management.

DOE/NV/13609-54
DOE M/1522 2007

Tritium Transport at the Rulison Site, a Nuclear-Stimulated Low-Permeability Natural Gas Reservoir

Publication No. 45224

September 2007

Work Performed Under DOE Contract Numbers DE-AC01-02GJ79491, DE-AC52-00NV13609, and DE-AC52-06NV26383 for the U.S. Department of Energy Office of Legacy Management.

THIS PAGE INTENTIONALLY LEFT BLANK

EXECUTIVE SUMMARY

The U.S. Department of Energy (DOE) and its predecessor agencies conducted a program in the 1960s and 1970s that evaluated technology for the nuclear stimulation of low-permeability natural gas reservoirs. The second project in the program, Project Rulison, was located in west-central Colorado. A 40-kiltoton nuclear device was detonated 2,568 m below the land surface in the Williams Fork Formation on September 10, 1969. The natural gas reservoirs in the Williams Fork Formation occur in low permeability, fractured sandstone lenses interbedded with shale. Radionuclides derived from residual fuel products, nuclear reactions, and activation products were generated as a result of the detonation. Most of the radionuclides are contained in a cooled, solidified melt glass phase created from vaporized and melted rock that re-condensed after the test. Of the mobile gas-phase radionuclides released, tritium (^{3}H or T) migration is of most concern. The other gas-phase radionuclides (^{85}Kr, ^{14}C) were largely removed during production testing in 1969 and 1970 and are no longer present in appreciable amounts. Substantial tritium remained because it is part of the water molecule, which is present in both the gas and liquid (aqueous) phases.

The objectives of this work are to calculate the nature and extent of tritium contamination in the subsurface from the Rulison test from the time of the test to present day (2007), and to evaluate tritium migration under natural-gas production conditions to a hypothetical gas production well in the most vulnerable location outside the DOE drilling restriction. The natural-gas production scenario involves a hypothetical production well located 258 m horizontally away from the detonation point, outside the edge of the current drilling exclusion area. The production interval in the hypothetical well is at the same elevation as the nuclear chimney created by the detonation, in order to evaluate the location most vulnerable to tritium migration.

A three-dimensional geologic model was developed of the local Williams Fork Formation at the Rulison site that includes a sequence of sandstone and shale lenses conditioned on observations at two site wells. The dominant flow and transport direction is east-west, in agreement with the direction of regional fractures in the area. The average sandstone lens length is approximately 161 m, and mean thickness is 7.5 m. The sandstone lenses are characterized by very low intrinsic permeability in core measurements (on the order of 10^{-18} m^2), while reservoir tests often indicate higher permeabilities (up to 10^{-16} m^2) presumably as a result of fractures encountered at the field scale. Porosity of Williams Fork sandstone units is generally reported as being between 0.01 and 0.1. Shale units are considered barriers to flow, with intrinsic permeability of 10^{-20} m^2.

A conceptual flow and transport model for the area around the emplacement well (where the nuclear device was located) was developed to investigate the rates of tritium transport in the subsurface away from the chimney. Tritium is transported as the tritiated water molecule ^{3}HHO in both the gas and liquid phase from the nuclear chimney (located in Lot 11) radially outward under a chemical concentration gradient for 38 years (the time from the nuclear test until 2007). At this time the hypothetical gas production well was placed in the model 258 m directly to the west, in Lot 12, and gas production was simulated for 30 years. During this time, transport was enhanced by the pressure gradient created by the production well.

The geologic and conceptual models were implemented in the numerical simulator TOUGH2, which solves for two-phase flow of gas and liquid, as well as transport of a compound in both phases. An equivalent porous medium approximation was used to simulate the fractured environment. Permeability and porosity distributions were developed based upon a statistical analysis of core data. Distributions were also developed for fracture permeability and hydrofracture length based on a multiple of the core permeability data, and literature values, respectively. Five hundred realizations were solved in TOUGH2, each representing one equally likely combination of sandstone-shale geometry and parameter values. Each model realization was simulated to determine the most likely length and time scales of tritium transport away from the chimney.

The simulator allows for partitioning between phases as well as radioactive decay. Results show that for the first 38 years following detonation of the nuclear device, tritium transport is controlled by gas diffusion and radioactive decay. The shape of the tritium plume is not dependent on the permeability field, as diffusion is controlled by tortuosity, which is in turn controlled by gas saturation and porosity. Based on the 50^{th} percentile of the 500 Monte Carlo simulations, the maximum travel distance of tritium was approximately 80 m from the nuclear detonation point during the 38 year period of diffusion. This is essentially the distance fractured by the nuclear detonation.

Production from the hypothetical gas well begins 38 years after the nuclear detonation (in the year 2007). Results of the Monte Carlo simulations suggest that tritiated water vapor above background concentrations will not reach the production well at the 95^{th} percentile. The peak mass fraction of tritium (mass of tritiated water in the gas phase to mass of the gas phase per unit volume) in the gas phase at the 95^{th} percentile is 1.01×10^{-21} g^{THO} g_{gas}^{-1}, as compared to the background mass fraction of tritium prior to nuclear testing, estimated at 10^{-20} (mass of tritiated water vapor to mass of gas, estimated from the background atomic ratio of 10^{-18} atoms of tritium to atoms of hydrogen). Breakthrough at the pumping well above background concentration is observed at the 99^{th} percentile, with a peak mass fraction of 2.33×10^{-19} g^{THO} g_{gas}^{-1}, occurring 68 years after the nuclear test. Partitioning of tritium between the gas and liquid phases results in liquid phase mass fractions approximately two times higher than those in the gas phase. The model only replicates subsurface processes and does not account for additional factors such as mixing and dilution in the production wellbore, nor does it account for exposure scenarios (e.g., transmission and dilution in a pipeline, inhalation routes from gas use) required to assess either exposure limits or doses.

Models are limited by the data used in them, as well as assumptions in their implementation. The results of this study are highly dependent on a combination of uncertain spatial features. A significant source of uncertainty is lack of knowledge regarding the three-dimensional spatial relationships of sandstone bodies in the subsurface, and the location and permeability of natural fractures in those sands. Porosity is another parameter that significantly controls transport. Additional uncertainty is introduced by lack of knowledge regarding the extent of hydrofractures and the permeability of these features, a limitation compounded by the hypothetical nature of the simulated production well. These sources of uncertainty (sand-shale geometry, permeability, porosity, hydrofracture length) are included within the Monte Carlo framework of the model and their impact on the results assessed by considering various confidence intervals. Only one gas-production scenario is examined by the Monte Carlo analysis and it is hypothetical and designed to represent production from the

location most vulnerable to transport. Other production scenarios (different well locations and different production rates) and other conditions (such as a regional pressure gradient, lower hydrofracture porosity, or nonisothermal conditions) could undergo Monte Carlo analysis if risk calculations suggest additional analysis is warranted. These features were examined for a single realization, the one at the 78th percentile of the Monte Carlo results, but did not alter the outcome of essentially no breakthrough of tritium at the production well(s) above background conditions.

ACKNOWLEDGEMENTS

The authors acknowledge the insightful comments provided by the Technical Working Group *ad hoc* review committee chaired by Andy Tompson (LLNL) and consisting of Mavrik Zavarin and Jeff Daniels (LLNL), Andy Wolfsberg and Dave Finegan (LANL), Richard Waddell (Geotrans, Inc.), and James Paces (USGS), and provided by Bruce Crowe (Stoller-Navarro Joint Venture), Rex Hodges, Rick Hutton, Dave Peterson, Rick Findlay, and John Duray (Stoller Grand-Junction) and Mary Picel, Kurt Picel, and Eugene Yan (ANL). An earlier phase of this work benefited greatly from conversations with Dave Prudic (USGS) and Greg Pohll (DRI). Finally, we thank David Gillespie for his careful interpretation of the geophysical logs and Lisa Wable for drawing many of the figures.

THIS PAGE INTENTIONALLY LEFT BLANK

CONTENTS

LIST OF FIGURES

LIST OF TABLES

LIST OF ACRONYMS

AEC	U.S. Atomic Energy Commission
CDF	cumulative distribution function
Ci	Curies
COGCC	Colorado Oil and Gas Conservation Commission
DOE	U.S. Department of Energy
DQO	data quality objective
EPA	U.S. Environmental Protection Agency
ERDA	U.S. Energy Research and Development Agency
IAEA	International Atomic Energy Agency
LHS	Latin Hypercube Sampling method
MCFD	thousand cubic feet per day
MCFQ	thousand cubic feet of gas
mD	milliDarcy
MMSCF	million standard cubic feet
MPa	megapascals
MWX	Multiwell Experiment
NTS	Nevada Test Site
Psia	pounds per square inch absolute
TOUGH2	Transport of Unsaturated Groundwater and Heat
T-PROGS	Transition Probability Geostatistical Software
	GAMEAS subroutine of T-PROGS modeling program
	GRAFXX subroutine of T-PROGS modeling program
	MCMOD subroutine of T-PROGS modeling program
	TSIM subroutine of T-PROGS modeling program
TU	tritium unit
TRUST	Capillary Pressure Function used in TOUGH2
TVD	true vertical depth
USGS	U.S. Geological Survey

1.0 INTRODUCTION

The U.S. Department of Energy (DOE), and its predecessor agencies, have been responsible for nuclear weapons research and development as part of the national defense program. In addition to atmospheric and underground testing of nuclear weapons, the government conducted Project Plowshare to investigate peaceful uses of nuclear devices. One Plowshare effort was a joint program between industry and government to develop technology for nuclear stimulation of low-permeability gas reservoirs to increase production of natural gas. Project Rulison was the second experiment under the gas-stimulation program and was run in conjunction with the Austral Oil Company of Houston, Texas.

The Rulison site is located in west-central Colorado, approximately 40 miles from Grand Junction (Figure 1-1). A 40-kiloton nuclear device was detonated in the Williams Fork Formation of the Mesaverde Group on September 10, 1969 (DOE, 2000a). The device was detonated 2,568 m below the ground surface in emplacement hole Hayward 25-95A, also known as Well R-E (Figure 1-2). The surface elevation at the emplacement hole is 2,485 m above mean sea level, and it is located within Lot 11, NE ¼, SW ¼ of Section 25, T7S, R95W, 6th Principal Meridian, Garfield County, Colorado. This is at latitude 39.40566 and longitude -107.948631, relative to North American Datum 1983. A site evaluation hole, Hayward 25-95, also known as Well R-EX, is located 95 m to the southeast.

Natural gas production testing was conducted in 1970 and 1971 to evaluate the success of the nuclear stimulation. Four separate production tests were conducted, and a total of 455 million standard cubic feet (MMSCF) of gas were produced. In 1971, the production test well was shut in (valves closed to stop production) and the site placed on stand-by status. General site cleanup operations commenced in summer 1972. The R-E and R-EX wells were plugged and abandoned in 1976. Descriptions of site deactivation and abandonment activities can be found in AEC (1973b) and ERDA (1977). Nonvolatile radioactive debris in the chimney remains classified material (AEC, 1973a). The nuclear detonation cavity is protected by over 2,400 m of overburden and a restriction on subsurface access. This restriction is as follows:

"No excavation, drilling, and/or removal of subsurface materials below a depth of 6,000 ft is permitted within Lot 11, NE ¼ SW ¼ of Section 25, Township 7 South, Range 95 West, 6th Principal Meridian, Garfield County, Colorado, without U.S. Government permission."

Annual sampling of wells, springs, and streams in the Rulison area has been conducted by the U.S. Environmental Protection Agency (EPA) since the time of the test as part of a long-term radiological surveillance program (DOE, 1984), with no radionuclides detected above background. No other significant activities occurred at the site until the Environmental Management Program of the U.S. DOE began a voluntary remediation of a surface mud pit in 1995. The Environmental Management Program systematically evaluates and remediates U.S. DOE sites having contamination related to Cold War activities. Subsequent to cleanup and closure of the surface mud pit, attention shifted to evaluating the subsurface contamination at Rulison (DOE, 2005).

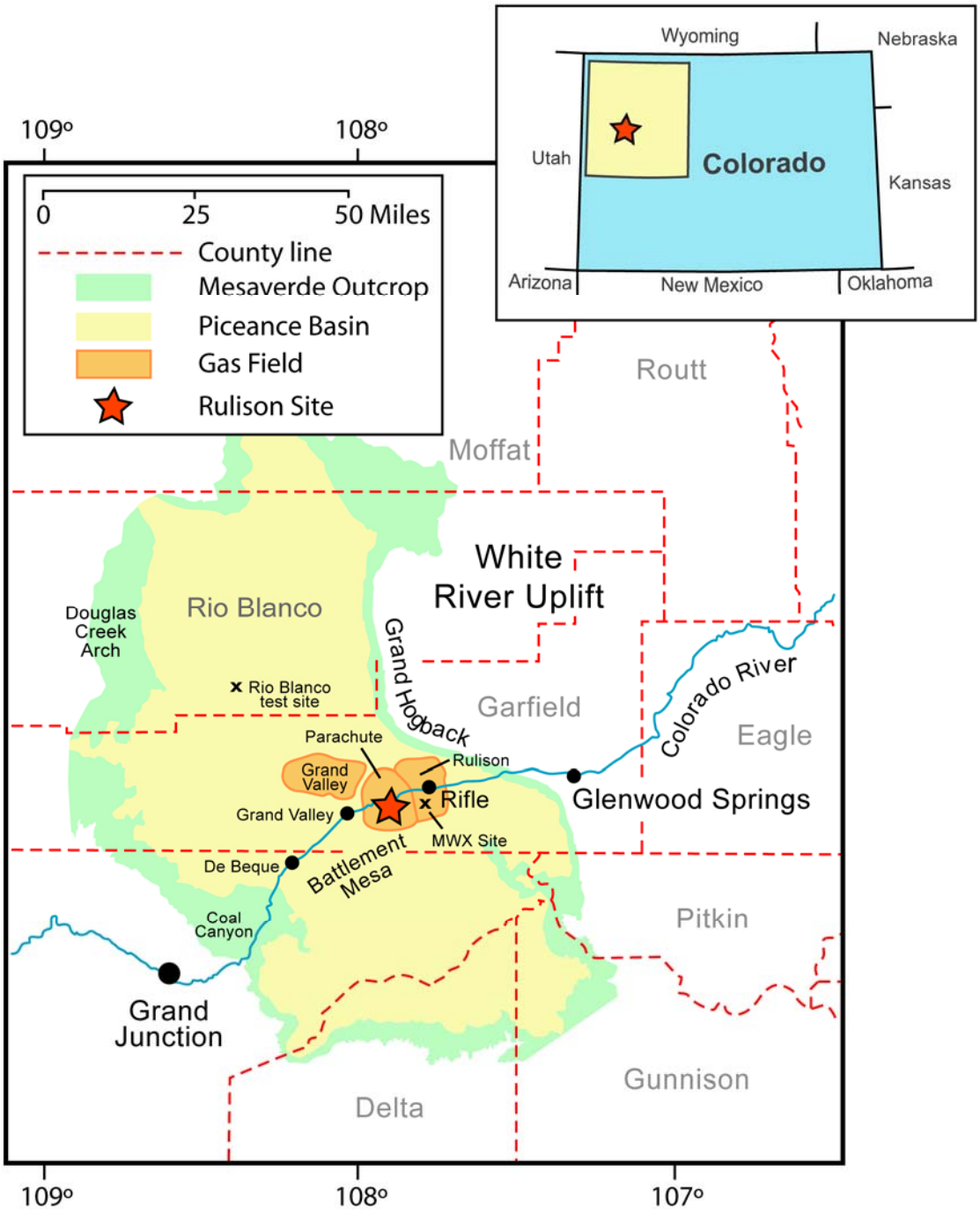

Figure 1-1. Location map showing the Piceance Basin in northwestern Colorado. The Rulison nuclear test site is located in the Battlement Mesa area.

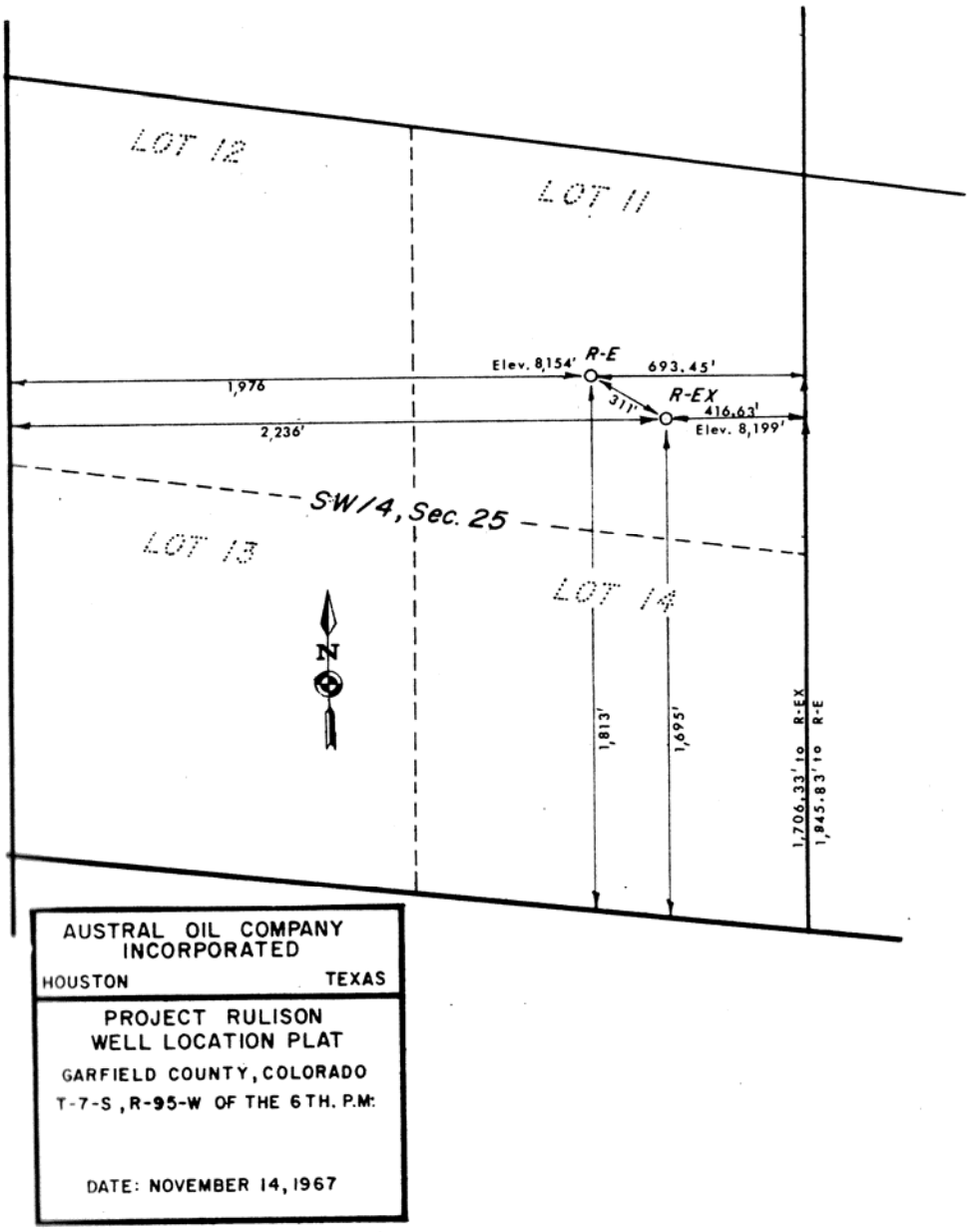

Figure 1-2. Surveyed location of Well R-E (Hayward 25-95A) and Well R-EX (Hayward 25-95). From Austral Oil Co. and CER Geonuclear, 1969. Distances to the quarter-section boundary are shown.

The purpose of the subsurface investigation at the Rulison Site is to obtain part of the information needed to achieve a site closure that is protective of human health and the environment. This entails evaluating if the existing subsurface restriction is adequately protective or needs to be modified, because there is no technically feasible method to remove the contamination existing in the nuclear cavity. The modeling reported here is a major part of the Rulison subsurface investigation.

This introduction continues by describing the Rulison project in more detail. This is followed by a description of the constituents of potential concern and conceptual site model that lead to the objectives of the model investigation. The introduction concludes with synopsis of the model approach for meeting the objectives.

After the introduction, subsequent sections provide the details of the model itself. The natural geologic and hydrogeologic setting being simulated is described, followed by the conditions resulting from the nuclear test. This information provides the foundation for the conceptual flow and transport models described next. The formulation of the numerical model occupies much of the report, describing the simulator, boundary conditions, and parameterization. Finally, the model results are presented and several alternative scenarios analyzed, followed by discussion and conclusions.

1.1 Project Rulison Operational History

Project Rulison was part of a program conducted by the U.S. Atomic Energy Commission (a predecessor of the U.S. DOE) to pursue peaceful uses of nuclear explosives, sometimes referred to as the Plowshare Program. Multiple uses were investigated, such as earth moving and excavation, and included using nuclear explosives to stimulate production from low-permeability gas reservoirs. The concept for gas stimulation was based on exploiting the large quantity of natural gas known to exist in very low-permeability reservoirs in sedimentary basins throughout the Rocky Mountain states. Creating a large effective wellbore and fractures in the adjacent formation with a nuclear explosive was proposed as possibly more efficient than using chemical explosives or hydraulic fracturing techniques (Rubin *et al*., 1972).

Three gas stimulation nuclear experiments were completed, with others in planning stages before the end of the Plowshare Program in 1977. The first was the Gasbuggy test in the San Juan Basin in northwestern New Mexico. The second was the Rulison test. The last was the Rio Blanco test, conducted to the north of Rulison, also in the Piceance Basin of Colorado. In all cases, production tests were conducted to evaluate the effectiveness of the stimulation, but the gas was flared (burned on site) and not introduced into any distribution system or otherwise used.

This accounting of activities related to Project Rulison relies primarily on the Project Manager's Report (AEC, 1973b). The Rulison project was a joint industry-government partnership. The industry sponsor was Austral Oil Company, which acquired gas leases in the project area and conducted a feasibility study in cooperation with the company CER Geonuclear. There were five objectives of the project: 1) to measure the changes in gas production caused by the nuclear explosion, 2) to measure the effective flow capacity of the nuclear fracture zone, 3) to determine the gas quality in regard to contamination by radioactivity and techniques for reducing contamination, 4) to identify the effective height and volume of the chimney and effective fracture zone radius as determined by production testing, and 5) to evaluate seismic effects of the detonation.

The Rulison project was conducted in three phases. Phase I included drilling a pretest exploratory hole (R-EX) and the device emplacement hole (R-E); performing pretest gas-production tests; and conducting geological, hydrological, and other studies for technical and safety consideration. Phase II focused on the nuclear explosive itself; its emplacement, detonation, and immediate effects. The explosive was placed at a depth of 2,568 m through a

10 ¾-inch steel casing that was then filled to the surface with stemming materials for containment purposes. Re-entry drilling occurred seven months after the detonation. This time allowed the radioactivity in the underground cavity created by the explosion to decay to less than a thousandth of that present immediately after the detonation. Phase III of the experiment, began in April 1970, involved drilling back into the chimney through the previously plugged R-EX well, with directional drilling to intercept the nuclear chimney (Figure 1-3), followed by flow testing to determine the cavity size and post-test production characteristics.

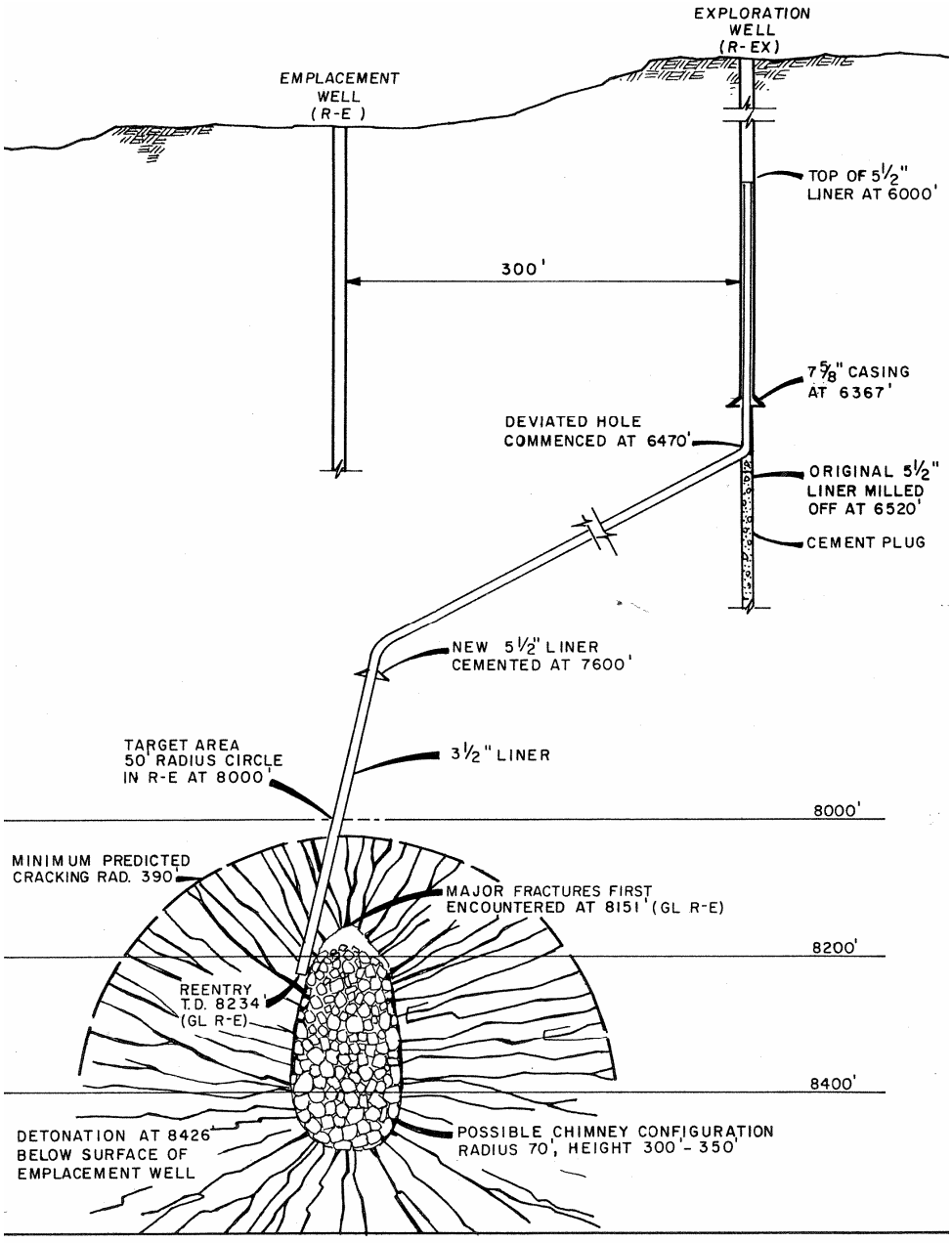

Figure 1-3. Schematic diagram of Rulison cavity and re-entry well. From AEC, 1973b.

Gas was produced from the Rulison chimney during an initial short-term calibration test and three subsequent flow tests. During all of these tests, the gas was flared (burned) to the atmosphere. The first attempts to perform the calibration test, on August 18 and 22, 1970, revealed the hole to be plugged. A drill rig was brought back to clean out the R-EX well, an operation that was completed on October 4, 1970. The calibration flaring was then conducted between October 4 and 7, 1970 and involved the production of 13 MMSCF of gas (Figure 1-4).

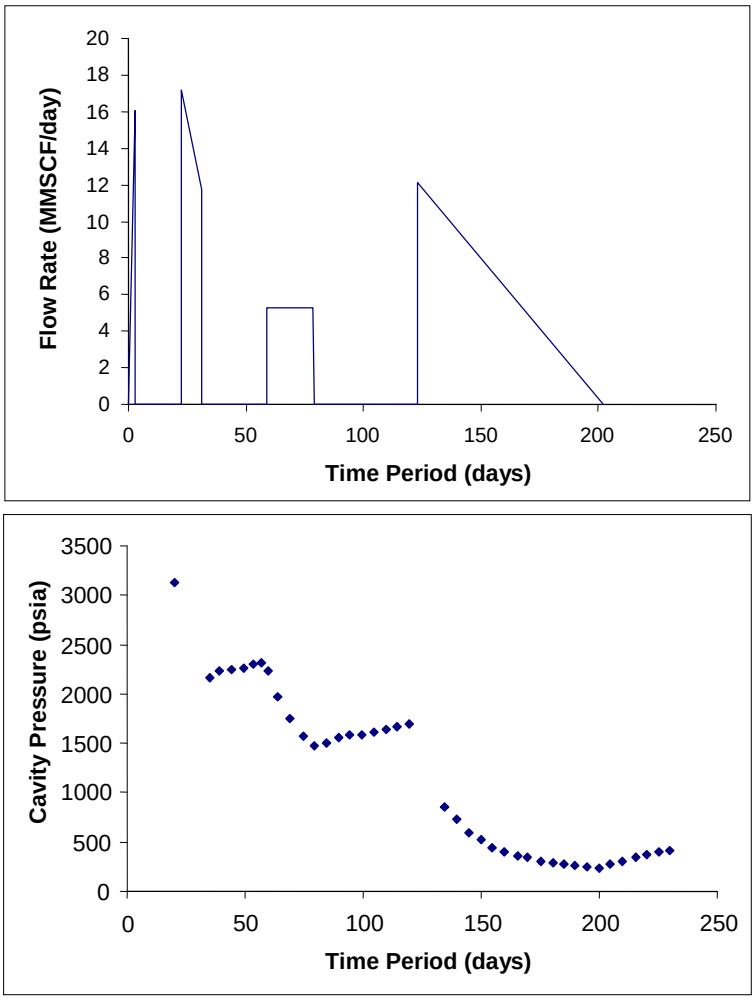

Figure 1-4. (a) Flow rates for the calibration and three production flow tests. Day zero is the commencement of testing on October 4, 1970. (b) Cavity pressure measurements during testing. The formation pressure at the start of testing was 3,200 psia (22 MPa). From AEC, 1973b.

A high flow-rate production test occurred between October 26 and November 3, 1970. A total of 109 MMSCF were produced during this test. After a short build-up period, an intermediate flow-rate production test was conducted from December 1 to 20, 1970. This test produced 100 MMSCF of gas. The final flow test ran from February 2 until April 23, 1971, and released 234 MMSCF. The approximately 456 MMSCF produced during the 108 days of flow testing was considered, at that time, to be equivalent to approximately 10 years of production from a conventionally stimulated well.

Cavity pressures were measured during low flow-rate testing and estimated for high flow-rate periods, and show a stair-step pattern of pressure reduction during testing, and build-up during shut-in periods, imposed on an overall pressure decline (Figure 1-4). The maximum flowing subsurface temperature recorded in the flow string at 2,499 m depth was 226° C. The loss of heat from the chimney as a result of the flowing gas and water and expansion of gas was indirectly observed by a decline in water production as water reached its vapor pressure and flashed into steam. The proportion of methane in the gas increased during production, while the relative amount of carbon dioxide and hydrogen gas declined, and was interpreted as reflecting the increasing production of native formation gas and discharge of non-hydrocarbon gases created by the explosion. Concentrations of tritium, ^{85}Kr, and ^{14}C declined throughout production testing (Figure 1-5).

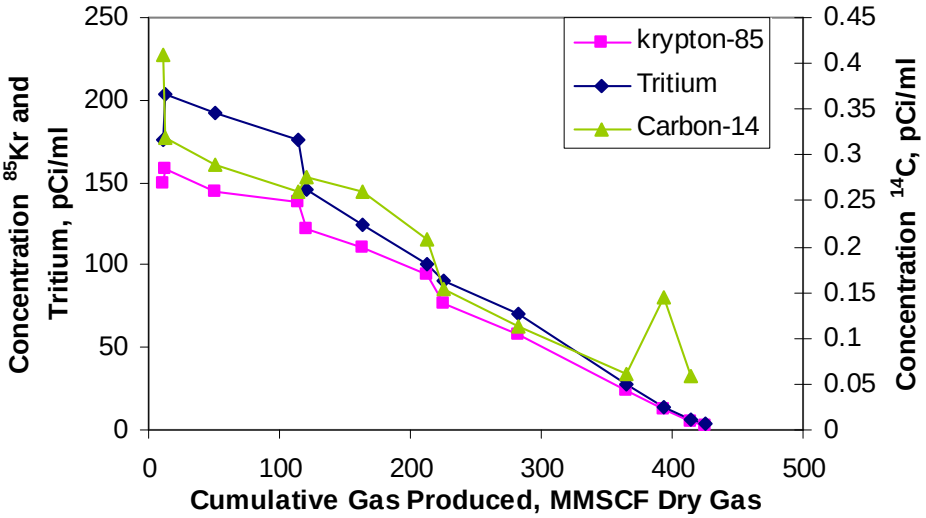

Figure 1-5. Radiochemical analyses of gas samples collected during Rulison production tests (from data in Smith, 1971). All concentrations are decay corrected to the time of detonation. Tritium is the total tritium activity summed for hydrogen gas and hydrocarbon gases (HT, CH_3T, C_2H_5T, and C_3H_7T).

1.2 Constituents of Potential Concern and the Conceptual Site Model

Radionuclides associated with an underground nuclear test are present in three basic forms: gases, surface deposits, and volume deposits (Smith *et al*., 1995), the proportions of which change with time after the detonation. Immediately after the detonation, essentially all of the radionuclides are part of a superheated, expanding gas (Borg *et al*., 1976). When the temperature and pressure begin to drop, many of the gases condense. The condensation occurs based on the boiling point of the nuclide, with the higher-boiling points (first to condense) referred to as refractory nuclides, and the lower-boiling point species referred to as volatile. The refractory species are primarily trapped in the solidifying melt, much of which collects at the base of the cavity as "puddle glass." These are the volume deposits, whose release is controlled by dissolution of this glass. Nuclides with somewhat lower boiling points remain volatile longer. Some portion of these is included in the puddle glass, but a portion is also deposited as coatings on chimney rubble surfaces. These surface deposits are more susceptible to dissolution by groundwater than the puddle glass. Once dissolved in

groundwater, surface and volume deposited radionuclides react with aquifer minerals, often exhibiting strong sorption properties that retard their movement.

As discussed in more detail in later sections, the subsurface environment at the Rulison test is within partially saturated, very low permeability rock. As a result of this environment, coupled with a slow glass dissolution rate and strong sorptive properties, volume and surface deposited radionuclides are not considered to pose a risk through a groundwater pathway at the Rulison site. These contaminants could pose a risk if materials from the cavity were brought to the surface, necessitating the existing drilling restriction surrounding the nuclear cavity through perpetuity.

Noncondensable radiogenic gaseous species with half-lives greater than a few minutes produced by a nuclear test include isotopes of argon, xenon, and krypton. Tritium and ^{14}C can occur in both gas and liquid phases. Assessments of potential biological hazards from Rulison operations (reentry, testing, flaring) (Robison and Anspaugh, 1969; Anspaugh *et al*., 1970) and an evaluation of potential radiation exposure to consumers of nuclear-stimulated natural gas (Rubin *et al*., 1972) concluded that the only radionuclides of significance for radiation exposure were tritium and ^{85}Kr. The other gas-phase radionuclides either decayed rapidly and/or were produced in small amounts. A separate analysis of radiologic implications of commercial use of natural gas from nuclear-stimulated wells identified tritium as the only radionuclide of concern (Jacobs *et al*., 1970).

Estimates of radionuclide mass resulting from the Rulison nuclear detonation can be combined with measurements of radionuclides removed during gas-production testing to derive the mass remaining in the subsurface. In general, accuracies of radionuclide estimates for underground nuclear tests are reported as 10 to 30 percent for fission products, 300 percent or better for tritium, and a factor of 10 for activation products, though uncertainties are lower when post-test measurements are available, as in the case for Rulison (Bowen *et al*., 2001). The uncertainty in radiochemical analyses of Rulison gas was estimated to be less than ±10 percent of the values (Smith, 1971). As presented by Smith (1971), four separate estimates of ^{85}Kr production have been made, ranging from 1,005 to 1,112 Curies (Ci). Without decay-correcting the amounts produced during post-test production testing (which would only increase the relative mass removed), 1,065 Ci of ^{85}Kr were removed from the subsurface (AEC, 1972a). A similar evaluation was performed for ^{14}C. These results indicate that at Rulison, the majority of the ^{85}Kr and ^{14}C produced by the test were removed by flaring operations. As a result, tritium is the contaminant of concern in the subsurface model.

A conceptual site model developed for the Rio Blanco gas stimulation site (DOE, 2000b) identified the nuclear cavity as the contamination source, natural gas migration as the release mechanism, and combustion of natural gas as the pathway. However, measurements during the flaring activities after the Rulison test determined that most of the tritiated methane gas and tritiated hydrogen gas was removed during testing. Only 13 percent of the total tritium mass was gaseous in methane and hydrogen gas, such that the significant remaining tritium source is in the form of liquid water and water vapor. Thermodynamic considerations indicate that this tritium will remain associated with water and not exchange with methane. As a result, the conceptual site model for Rulison (Figure 1-6) does not consider tritiated natural gas as a pathway.

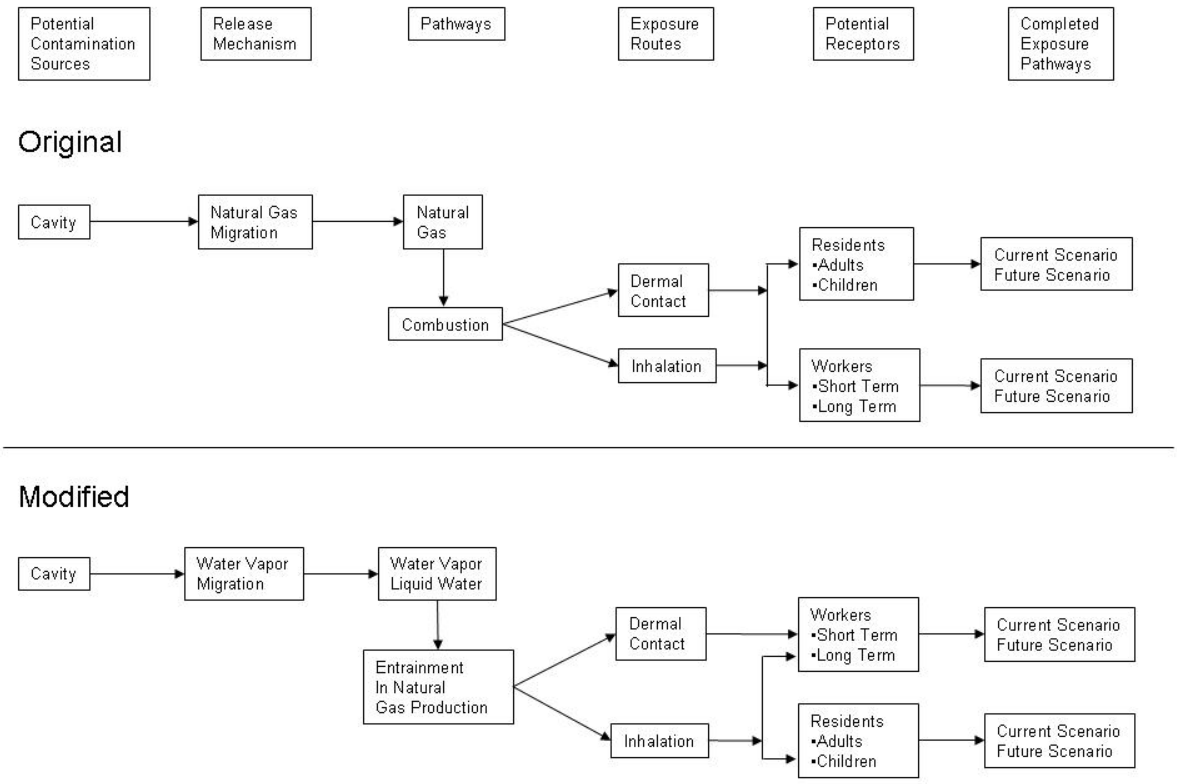

Figure 1-6. Conceptual site model for the Rulison subsurface with tritium in water as the contaminant of concern.

The Rulison conceptual site model identifies the cavity as the contamination source, but identifies water vapor migration as the release mechanism, and a pathway of water (vapor and liquid) entrainment with natural gas production. Exposure routes would be through dermal contact with tritiated liquid water by workers (especially during liquid separation processes), and inhalation of tritiated water vapor entrained with natural gas by workers or the public.

The model of gas flow and tritium transport presented here spans several hundred years, from the time of the Rulison test forward. The half-life of tritium is 12.32 years, resulting in essentially complete decay of the contaminant of concern to non-radioactive helium within a couple of hundred years after the nuclear test. Given that the tritium mass reduces as time proceeds, and given the current intensity of natural gas production in the area, the production scenario considers the worst case of immediate nearby gas production. The radionuclide volume and surface deposits in the chimney, described previously, include some very long-lived radionuclides that remain a hazard for many thousands of years. These non-gaseous radionuclides are not part of the analysis presented here.

1.3 Objective

The purpose of the subsurface investigation for Rulison is to obtain part of the information needed to achieve a site closure that is protective of human health and the environment. Determining if there could be contaminant transport from the Rulison test cavity into resources of value, either under existing conditions or during future resource development is an important part of the evaluation. This requires determining the nature and extent of contamination in the subsurface and how it changes with time, developing likely scenarios for future resource development and determining their possible impact on the extent of contamination, and evaluating the estimated contamination extent relative to the existing drilling restrictions.

The ability to define acceptable and unacceptable concentrations of radionuclides in the subsurface is limited until a human health risk assessment occurs. For example, numerical models are capable of calculating very low radionuclide concentrations such that though migration of mass may be predicted, it may not be of any practical significance. Similarly, contaminant mass predicted in the subsurface environment poses a threat to human health only after a series of processes involved in the exposure pathway, many of which can significantly change the exposure consequence. Recognizing these limitations for interpreting the results of the subsurface flow and transport model, the specific objectives for the model reported here are as follows:

- Calculate the nature and extent of tritium contamination in the subsurface from the Rulison test, from the time of the test to present day (2007). This involves gas-phase migration under natural conditions because no production wells have been active nearby during this time. Include the effect of parameter uncertainty in the calculations.
- Determine the most vulnerable natural-gas production well location, outside the DOE drilling restriction, in terms of inducing tritium migration from the Rulison test. Evaluate migration under gas production conditions to that well location, including assessing the uncertainty in the predictions.

After meeting these objectives in the work reported here, the results can be used in an exposure assessment to determine the significance of predicted contaminant migration, leading to assessment of the adequacy of current drilling restrictions. It is possible that the exposure assessment may require additional simulation of subsurface transport, for instance the evaluation of other hypothetical production well locations.

1.4 Approach

Numerical modeling is used to meet the specific model objectives. Mathematical models for subsurface liquid and vapor flow consist of a set of governing equations. Exact solutions to these equations can be obtained analytically, but only for certain conditions. Though simplifying assumptions are also required for numerical models, they are less restrictive than for analytical solutions. A numerical model allows a closer approximation of the true subsurface environment, although significant uncertainties are inherent.

For Project Rulison, major sources of uncertainty for a subsurface flow and transport model derive from the combined effects of natural variability in the structure and lithology of the rocks surrounding the detonation site, limited knowledge of the pre- and post-test

physical and hydraulic properties of the country rock, uncertainty in implementing the site conceptual model in a subsurface flow and transport model, and uncertainty in defining the conditions associated with future resource development. Some of these uncertainties are addressed by using a Monte Carlo modeling approach that produces a range of possible model outcomes by analyzing a large number of simulations with random quantities for uncertain variables. The variability in model outcomes provides decision makers with additional information for assessing and developing strategies for site management.

Knowledge of the natural subsurface conditions, and the effects of the nuclear test on that environment, were used to develop conceptual models of fluid flow and tritium transport. The conceptual flow model was sensitive to the distribution of sand and shale in the subsurface, so the numerical model was constructed to consider many of the geometries possible for these heterogeneous units. Additional sources of significant uncertainty were identified in the parameter values for porosity, intrinsic permeability, and anisotropy in intrinsic permeability. Parametric uncertainty in these characteristics was included in the model by running the model many times and selecting different parameter values from distributions suggested by the data. The length of hydraulic fractures (hydrofractures) in a hypothetical production well was also treated as uncertain, and permeability of hydrofractures was related to the intrinsic permeability selected for native sand in a given realization.

The extent of possible contaminant migration from the Rulison test to the present day (2006) was computed for 500 realizations of the flow and transport model. These not only address the first objective of determining transport under natural conditions, the realizations provide the starting point for an additional 500 realizations analyzing migration under conditions of a hypothetical gas production well located at the most vulnerable location relative to the nuclear test. This stochastic approach allows analysis of the outcome in terms of confidence intervals. Using a single permeability and porosity realization, several alternative scenarios are also analyzed for model features that do not lend themselves to Monte Carlo techniques, such as hypothetical well location.

THIS PAGE INTENTIONALLY LEFT BLANK

2.0 GEOLOGIC SETTING AND NUCLEAR EFFECTS

2.1 Regional Geologic Setting

2.1.1 Stratigraphy and Depositional Environment

The Piceance Basin is a large structural basin containing thousands of meters of sedimentary rocks principally deposited in association with the Cretaceous Western Interior Seaway. The basin trends northwest-southeast through northwestern Colorado. It is bounded by structural highs, such as the White River Uplift east of the Grand Hogback, and is generally defined by the outcrop of the Mesaverde Group (Figure 1-1). The Douglas Creek Arch, bounding the western edge, separates the Piceance and Uinta basins. The fossil fuel resource potential of the basin sediments has long been recognized, and as a result, the Piceance Basin has been extensively studied for resource development. Investigations focusing on the coal-bed deposits of the Green River Formation are less relevant, but work focused on basin-centered natural gas accumulations is of direct interest for the Rulison nuclear test. The Rulison nuclear test was conducted in the Parachute Gas Field, located approximately in the south-central Piceance Basin. The information presented here is summarized from the many research papers published regarding the basin, such as Lorenz (1990), Hettinger and Kirschbaum (2002), Johnson and Roberts (2003), Cumella and Ostby (2003), and Patterson *et al*. (2003).

The base of the stratigraphic sequence of interest is the Mancos Shale (Figure 2-1). The Mancos is largely comprised of mudrock deposited in offshore marine environments. It has hydrocarbon-producing units of its own and may be a source rock for hydrocarbons migrating upward, particularly in the upper part where the Mancos often intertongues with the Mesaverde Group.

The Mesaverde is generally considered a group, though some literature (particularly older works) refer to it as a formation. The nomenclature applied to members of the Mesaverde is complex and inconsistent, often reflecting regional usage. The Group is generally represented by two Formations. The lowermost Formation, overlying the Mancos Shale, is the marine Iles Formation. It contains laterally continuous blanket sandstones, such as the Corcoran, Cozzette, and Rollins. The uppermost Formation is the nonmarine Williams Fork. The Williams Fork is a thick sequence of sediments deposited in deltaic, coastal plain, and fluvial environments. The Rulison nuclear test occurred in the Williams Fork Formation.

From bottom to top, the Williams Fork Formation transitions from paludal to coastal to fluvial to paralic depositional environments. The paludal (marsh environment) interval lies above the Rollins Sandstone and contains abundant coal beds deposited in a lower delta plain environment. The Cameo-Fairfield coal zone is a prominent unit at the base of the Williams Fork. The coastal interval contains distributary channel sandstones deposited in an upper delta plain, interbedded with mudstones and siltstones. The fluvial interval is characterized by stacked point-bar sandstones, also interbedded with mudstones and siltstones. The distinction between the coastal and fluvial intervals is not made by many workers (they are usually lumped together as fluvial), but they were distinguished at the Multiwell Experiment (MWX) site where abundant core samples were collected. The MWX was a field laboratory developed in the Piceance Basin by DOE to characterize the low-permeability reservoirs in the Mesaverde Group and develop technology for their production (Sandia and CER, 1990).

The paralic interval (lagoonal; intertongued marine and continental deposits laid down on the landward side of a coast) contains more widespread sandstones, reflecting a return to a marine depositional environment.

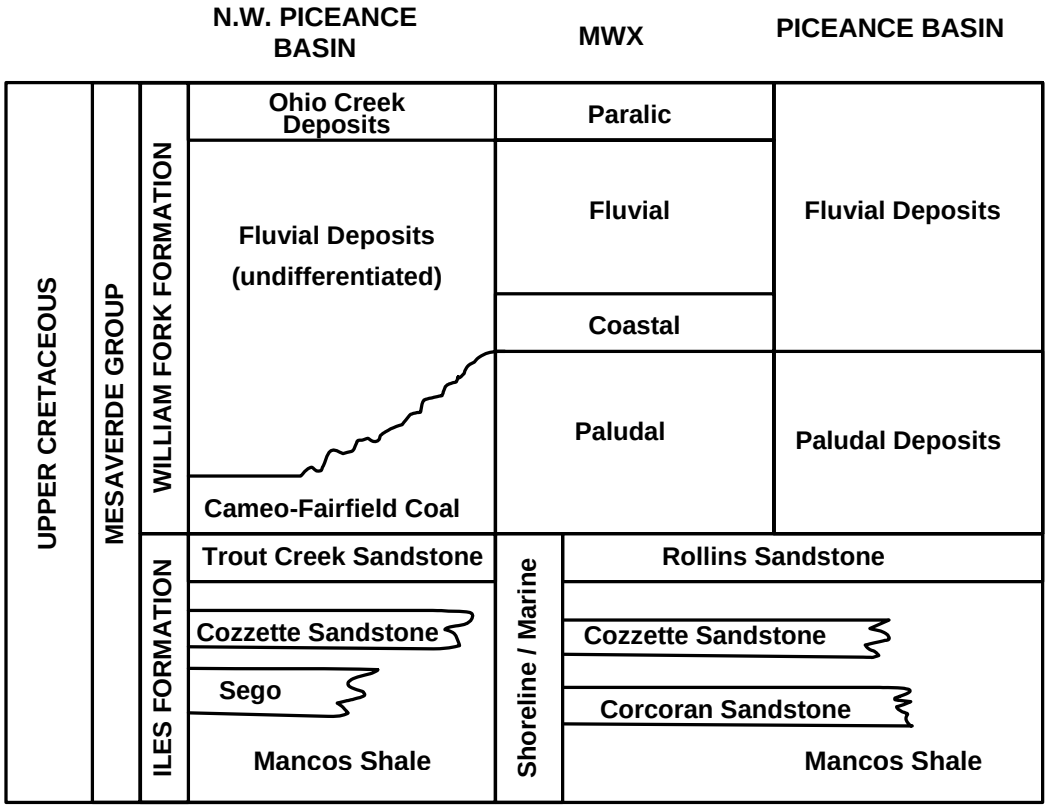

Figure 2-1. Stratigraphic nomenclature used by various workers in the area. Adapted from Myal *et al*. (1989).

Gas production in the Parachute Field is primarily from the fluvial section of the Williams Fork Formation. Gas is trapped in stacked, very low permeability (matrix permeability $<10^{-17}$ m^2), highly discontinuous sand bodies. This is an unconventional gas reservoir in that gas accumulations lack easily definable stratigraphic or structural seals, and water is found above gas (Figure 2-2). Interbedded coals and carbonaceous shales are believed to be the source rocks for most of the hydrocarbons. Distances of hydrocarbon migration, from source rocks to current location, are generally considered to be small as a consequence of extremely low permeabilities. At the water contents typically found in the basin (about 40 percent), permeability of gas may be lower than that of water such that gas is trapped by a relative permeability barrier as water is expelled during gas generation (Johnson, 1989).

The continuity of sandstone units present in the fluvial interval was evaluated between 13 wells in various combinations (Peterson and Kohout,1982). Seventy-five percent of the sand units with average thicknesses from 6 to 9 m were found to correlate across

518 m. Sand bodies in the lower fluvial interval at the MWX site have widths of 305 to 762 m (Sandia and CER, 1990), although Lorenz (1990) describes widths from 63 to 320 m for the lower fluvial interval. "Width" in the literature appears to essentially refer to the lateral dimension, as the arcuate geometry is not readily separated into a width and length. Recent investigations by Cole and Cumella (2004) report a range in sand body width of 12.2 to 850.7 m, with an average of 161 m. Cole and Cumella state that their studied outcrops in Coal Canyon (about 32 km southwest of Rulison) are stratigraphically equivalent to the productive intervals in the Parachute Field.

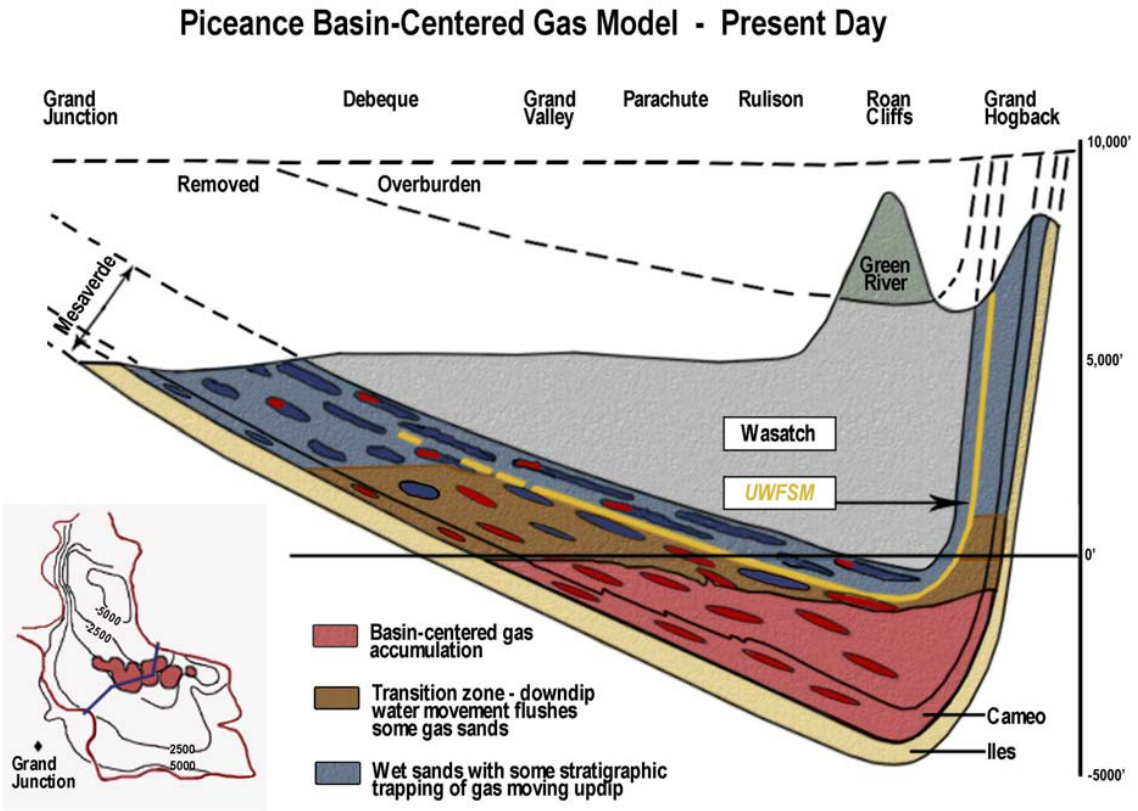

Figure 2-2. Basin-centered gas model for the Piceance Basin, as presented by Cumella and Ostby (2003). "UWFSM" is the Upper Williams Fork Shale Marker bed, and ovals represent low permeability, discontinuous sandstone reservoirs. The line of section is shown on the inset map. This section crosses the Parachute Field in the Colorado River valley, so that the Rulison test site is to the south and at higher elevation. Stratigraphically, the detonation occurred in the basin-centered gas accumulation (red) zone.

Depositional trends and well orientation were found by Peterson and Kohout (1982) to make little difference in terms of sand unit continuity because the long dimension of the point bars was considered random, despite the trend of a given meander belt. Conversely, Cole and Cumella (2004) examined paleocurrent data at outcrops in Coal Canyon and identified a unimodal distribution with a vector mean orientation of 75°, suggesting the channels tend to run northeast-southwest.

The Ohio Creek stratigraphic unit has been reported variously as the upper member of the Mesaverde Group, and as a separate formation between the overlying Wasatch Formation and underlying Mesaverde Group. It is comprised of thicker and more continuous sandstone deposits than occur in much of the underlying Williams Fork Formation. Lorenz (1990) interpreted the more widespread and uniform Ohio Creek sandstones as deposited in a paralic environment, a nonmarine coastal zone subject to marine invasion. Patterson *et al*. (2003) interpreted sand deposition in a fluvial environment containing braided channels.

Above the Ohio Creek Member is the Wasatch Formation, which correlates to the Fort Union Formation identified elsewhere in the basin (e.g., at the Rio Blanco nuclear test). The Wasatch Formation consists principally of clay and shale, though sandstone lenses are common. The overlying Green River Formation is comprised chiefly of shale and marlstone, with minor amounts of sandstone, siltstone, and limestone. In parts of the basin, the Green River Formation is exploited as a coal resource. Quaternary alluvial deposits occur along drainages in the region.

2.1.2 Structure

Though data regarding basement structures in the Piceance Basin are sparse, a northwest structural grain is reflected in monoclines and faults (Verbeek and Grout, 1997). Fracture strikes in the Mesaverde Group have been related to the westward thrusting of basement rocks in the White River Uplift, with the Grand Hogback Monocline as evidence of that thrust. Fractures in both outcrop and in the subsurface strike approximately east-west, but change systematically with the reconstructed Laramide stress trajectory as it fans out westward (Lorenz, 2003). Dominant extensional fractures were unidirectional in the MWX wells with very few high-angle orthogonal cross fractures; this supports the idea that in areas of the Piceance Basin lacking tectonic deformation, subsurface fractures are predominantly short, poorly interconnected, and unidirectional with very little cross-fracturing (Myal *et al*., 1989; Lorenz *et al*., 1989). This was taken to indicate that fractures of the Hogback system (those related to the Hogback Monocline) are unidirectional at depth and trend west-northwest to northwest (Myal *et al*., 1989).

Two dominant joint sets associated with the Grand Hogback Monocline are present at the MWX site. The older set has an average strike of N 80 W. Fractures within this set are abundant in the sandstones of the Mesaverde Group, but not higher in the stratigraphic section. The second group of fractures strikes N 10 E and occurs in the overlying Wasatch Formation. Vertical fractures with generally east-west orientations have been found from the Piceance Creek Dome, and from the Mamm Creek, Rulison, Parachute, and Grand Valley fields (Lorenz, 2003).

2.2 Site-specific Geologic Setting

The Rulison nuclear test site is located in the south-central Piceance Basin, near the structural axis. The MWX site is located about 11 km to the northeast. Beds penetrated by the exploratory and emplacement holes at Rulison are almost flat-lying, dipping northeastward at 2° or less.

Approximately 762 m of Mesaverde Group sediments were penetrated at the Rulison site (Voegeli and West, 1970), which is not the entire section (Figure 2-3). Peterson and Kohout (1982) identify the lower fluvial interval as extending from below the total depth of

well Hayward 25-95 (the Rulison exploratory hole, also referred to as R-EX) to a depth of 2,259 m, the middle fluvial zone as extending from a depth of 2,259 to 2,106 m, and the upper fluvial zone as extending from a depth of 2,106 to 1,942 m. Though Voegeli and West (1970) report the Ohio Creek Member as 11.2 m thick, Peterson and Kohout (1982) describe a 67-m thick zone of paralic sediments, equated with the Ohio Creek Member on their stratigraphic column, between the depths of 1,875 to 1,942 m. The overlying Wasatch is approximately 1,189 m thick, and the Green River Formation is about 518 m thick (Voegeli and West, 1970). Quaternary alluvial deposits near the site generally range in thickness from 6 to 12 m.

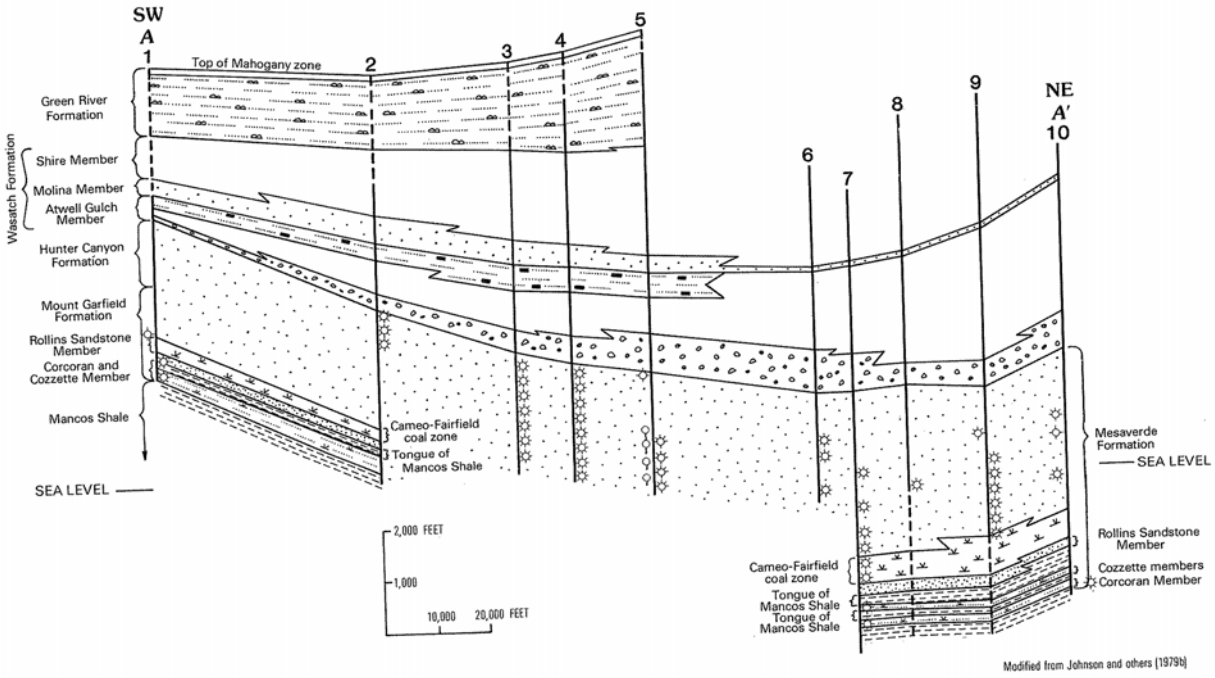

Figure 2-3. Cross section showing lithology and environment of deposition developed by Johnson *et al.* (1979) and presented in Johnson (1989). Well 5 is the Rulison exploratory hole, Hayward 25-95.

The lower fluvial zone of the Mesaverde Group identified by Peterson and Kohout (1982) includes the Rulison detonation horizon. The contact they identify between the lower and middle fluvial zones can be seen as a depositional change on the normalized neutron and gamma logs (Figure 2-4). Above the contact, sandstone units are less numerous, thinner and less continuous. Below the contact, the sandstone units are more numerous, thicker and more continuous. This lower fluvial zone in Hayward 25-95A (the Rulison nuclear emplacement well, also referred to as Well R-E) encounters 25 sandstone units within 378 m. These sandstones average 7.2 m in thickness and comprise about 45 percent of the section. The well log interpretations are supported by the few core samples available (Figure 2-5).

The gas reservoir in the lower fluvial interval occurs in discrete meander-belt sandstones composed of point bar sequences. They are irregular in shape and occur as

isolated sand bodies separated by siltstones and mudstones. Correlation of sand bodies between Hayward 25-95 and Hayward 25-95A, a distance of 86.9 m, is good (Figure 2-6). Peterson and Kohout (1982) found that 75 percent of sand bodies correlated between the two Rulison wells in the lower fluvial interval.

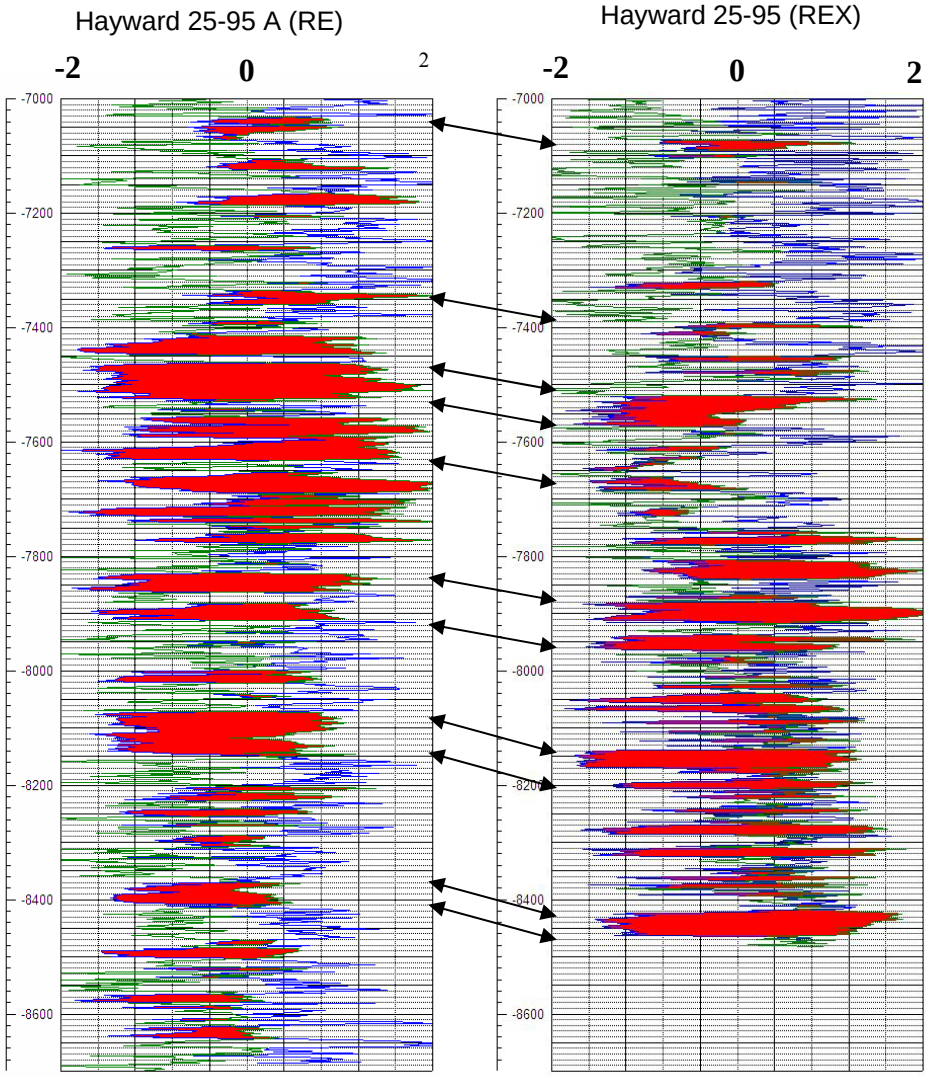

Figure 2-4. Normalized neutron logs (green) and normalized gamma logs (blue) for the Rulison emplacement and exploratory boreholes. Interpreted sandstone intervals are highlighted in red. Depth scale is in feet. Correlations are shown by arrows and are consistent with the land elevation difference. Contact between two distinct depositional facies is apparent at 2,274 m (7,461 ft) in Hayward 29-95A (R-E) and 2,292 m (7,518 ft) in Hayward 25-95 (R-EX).

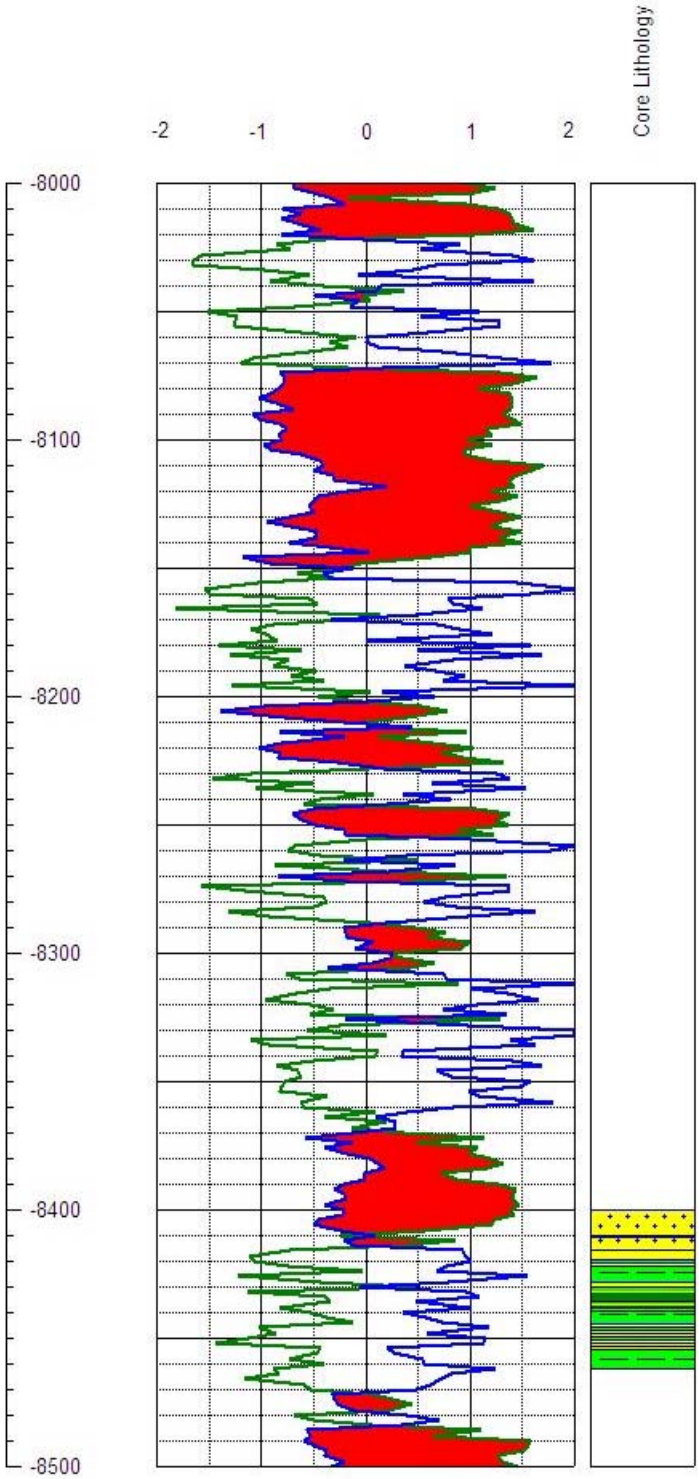

Figure 2-5. Comparison between lithology as interpreted from the neutron (green trace) and gamma (blue trace) logs in well Hayward 25-95A and core samples reported by Hill (1971). Sandstone intervals interpreted from the logs are highlighted in red. For the core, the yellow speckled pattern denotes sandstone; the green hachured pattern represents shale and siltstone. Depth scale is in feet.

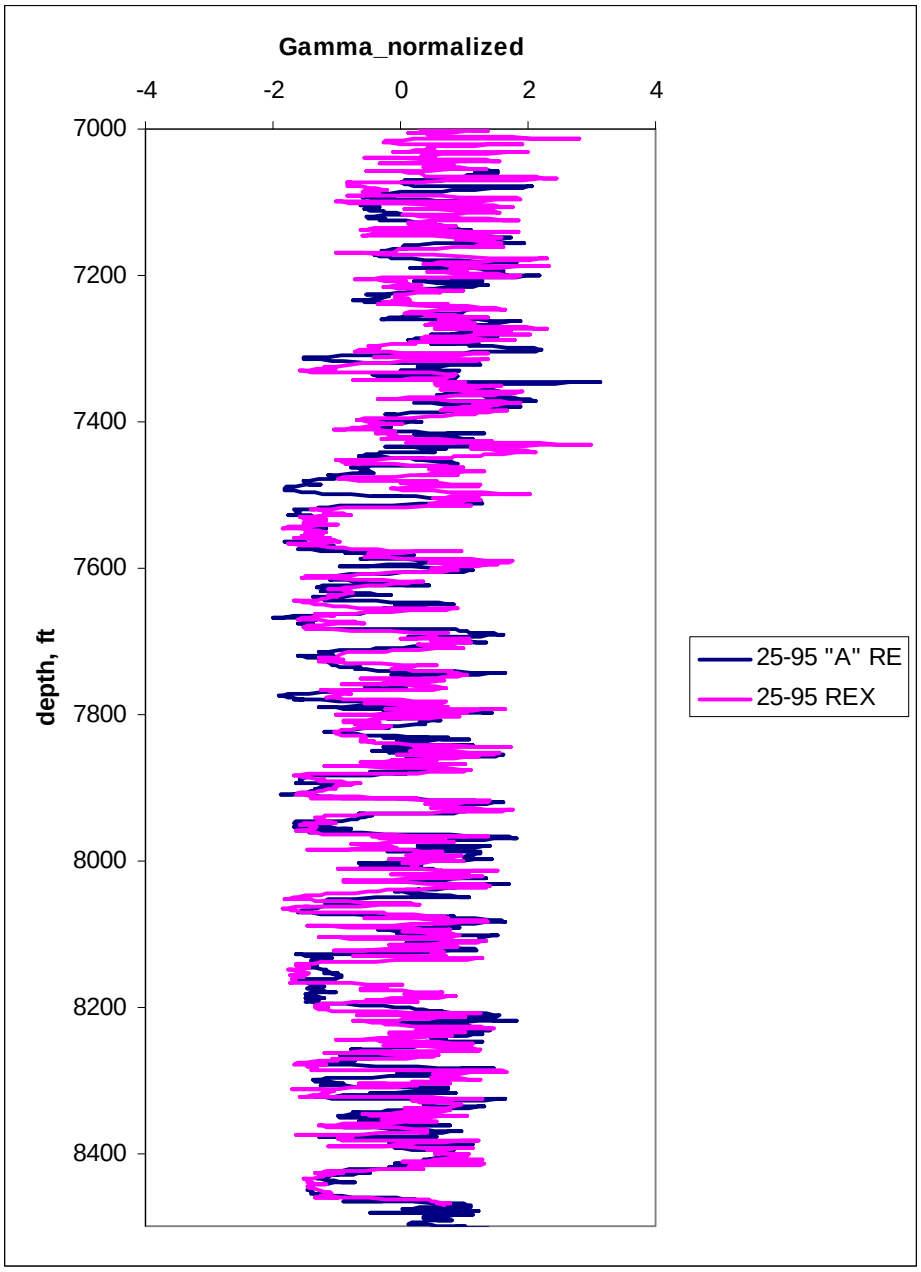

Figure 2-6. Correlation in normalized gamma logs between wells Hayward 25-95 (Well R-EX) and Hayward 25-95A (Well RE). The 25-95A log is shifted down 53 ft relative to the 25-95 log.

2.3 Explosive Phenomenology of the Rulison Nuclear Test

The Rulison nuclear device was detonated at a depth of 2,568 m. The pressure wave resulting from the detonation exceeded lithostatic pressure and caused fracturing of the surrounding Mesaverde Group sedimentary rock. The extreme temperature and pressure

vaporized rock, water, and gas in the vicinity of the device, resulting in formation of an underground cavity. The cavity created by the Rulison explosion has been reported as 23.2 to 23.8 m in radius, based on estimates derived from equation-of-state calculations, ^{85}Kr measurements, and pressure test analysis (AEC, 1973b). Geophones indicated prompt collapse of some of the overburden rock into the cavity between 48 and 150 seconds post-test (Frank, 1971). Seismometers also showed some noise up until 9 hours after the detonation. These observations are consistent with cavity collapse experience at the Nevada Test Site.

The first measurement of wellhead pressure in the emplacement well was measured 138 hours after the detonation and was recorded as 2.7 MPa (390 pounds per square inch gauge [psig]). The pressure increased to 17.2 MPa (2,500 psig) by December 14, 1969 (three months after the detonation). The bottom hole pressure on December 14 was estimated as 20.2 MPa (2937 psia [pounds per square inch referenced to atmospheric pressure]). The high wellhead pressures of the emplacement well suggested that re-entry drilling would require dealing with radioactive materials in both the liquid and gas phases. As a result, re-entry drilling was accomplished by sidetracking from the evaluation (R-EX) well (directional drilling out of the R-EX borehole).

Re-entry drilling was delayed for nearly 11 months after the detonation to allow the short half-life radionuclides of biological significance to decay. The sidetrack drilling commenced at 1,972 m in well R-EX; at a true vertical depth (tvd) of 2,484 m (84 m above the nuclear detonation point) below the land surface, circulation was lost. This was interpreted to be the top of the chimney. Drilling with loss circulation continued until a tvd of 2,510 m.

Three production tests were conducted on the sidetracked hole (DeGolyer and MacNaughton, 1971). The first lasted between October 26, 1970 and November 2, 1970. Approximately 11-15 thousand cubic feet of gas per day (MCFD) were produced. The well was shut in until November 30 while pressure and temperature data were recorded. The second test flowed between December 1 and 20, 1970, and produced approximately 5 MCFD. Following a shut-in period between Dec. 20, 1970 and February 1, 1971, the well was again allowed to flow between Feb. 2 and April 23, 1971. During this period, the gas flow rate dropped from 10.4 MCFD to less than 1 MCFD. Gas compositions measured at the beginning of the first test consisted of 30 percent methane, 15 percent hydrogen, 46 percent carbon dioxide (Frank, 1971). Aside from concentrations of tritium and krypton in the range of hundreds of pCi l^{-1} (picocuries per liter), the composition of the remaining 9 percent was not reported by Frank (1971). The Project Rulison Managers report (AEC, 1973b) reports that a total of 374 MMSCF (million standard cubic feet of gas) was produced, and that during the life of the production tests concentrations of hydrogen and carbon dioxide declined while that of methane increased. Downhole samples of water obtained on April 19, 1971, from 2,499 m were obtained and confirmed that both liquid water and steam existed in the cavity (AEC, 1973b). The cavity temperature at that time was estimated as 200ºC.

Systematic fracturing relationships have been observed at other nuclear test sites in a range of environments, as reported by Borg *et al*. (1976). A zone of highly crushed rock typically extends out 1.3 cavity radii (r_c), which for Rulison would be about 30.5 m. Beyond this is a region of pervasively fractured rock. The extent of this zone depends on the mechanical properties of the rock, but the outer limit is between 2.5 and 4 r_c (58.8 and 93.9 m at Rulison). Fractures on all scales are recognized in this region and detectable by a

variety of tests (Borg *et al*., 1976). Beyond this, fractures become widely spaced and less interconnected. At distances between 3.5 and 5.2 r_c (82.3 and 121.9 m for the Rulison cavity radius), depending again on the rock material properties, the compressive stress of the shock wave was too small to fracture the rock. This limit of shear failure is often observed to coincide with the height of the chimney for many tests. Beyond this, tensile fractures may have occurred, but would be widely spaced and would not contribute to an increase in overall permeability. Comparison of horizontal fracture radii with the limit of shear failure indicates that horizontal fracture radii are consistently smaller (Borg, 1973).

Fractures generated by nuclear tests are usually visualized as radial and tangential systems symmetrically located around the working point. Such fracture orientations are consistent with those expected in a brittle, mechanically isotropic medium, or in an anisotropic medium under large hydrostatic stress, as is typical of deeply buried nuclear tests (Borg *et al*., 1976). Many nuclear tests do not fit in either of the descriptive categories above, and fracture systems surrounding cavities are influenced by pre-existing heterogeneities such as bedding, joints, and faults. For example, both shock-induced fractures, and the shape of the chimney for the Pile Driver test, conducted in granite at a depth of 463 m, were influenced by pre-existing joint systems (Borg, 1970). Conversely, large stresses associated with the shock wave, and the repeated loading and unloading near cavity walls and to some distance beyond, can obliterate radially or tangentially oriented detonation induced fractures, as well as all traces of pre-existing fractures. Further away, it can be expected that explosion-produced fractures will mimic the joint and fault system of the bedrock.

At Rulison, major fractures were first noted at a depth of 2,484.4 m during re-entry drilling (AEC, 1973b). This indicates that the chimney height is 83.8 m above the working point. This coincides very well with the shear failure limit calculated based on rock properties of 80.2 m (Borg, 1973). The extent of the increased permeability zone around the test was a fitting parameter in two separate analyses of the Rulison gas production tests. Modeling by Lawrence Radiation Laboratory found the production data best fit with a 33-fold increase in permeability in a region from the chimney wall out to a radial distance of 2.75 r_c (63.7 m using their estimate of 23.2 m for r_c) (Rubin *et al*., 1972). DeGolyer and MacNaughton (1971) fit the production data with a different model using an outer fracture radius of 67.1 m and a chimney height of 82.3 m. Thus the observed post-test fractures and production modeling results are reasonably consistent in indicating that permeable, interconnected fractures generated by the Rulison test extend out from the working point some distance between 63.7 and 83.8 m. This distance is also consistent with the general fracturing relationships described earlier for nuclear tests.

3.0 CONCEPTUAL MODEL OF FLOW AND TRANSPORT

3.1 Conceptual Flow Model

At the Rulison site, the pore space in the Williams Fork Formation is filled with both gas (approximately 40 percent saturation) and water (approximately 60 percent saturation). Oil, if present, is disregarded as an active phase in the problem (it does not move or interact with the moving phases). Assuming the fracture aperture is typically larger than the characteristic pore diameter, the fractures will be filled with the gas-phase fluid, while the pore spaces contain both gas and liquid phases (Wang and Narasimhan, 1985). This distribution of phases in the rock is derived from considerations of capillarity in the Laplace-Young equation. Both phases are assumed to be continuous throughout the reservoir and capable of flowing in response to pressure gradients of each phase.

Typically, producing gas reservoirs are high-permeability sandstones sealed above and below by low-permeability rocks such as shale, siltstone, or evaporites (Hubbert, 1953; Law and Dickinson, 1985; Lerche and Thomsen, 1994; Dahlberg, 1995). The reservoir fluids are often stratified in the classic textbook manner where gas overlies water or brine with a discrete contact; sometimes a layer of petroleum (a third fluid phase) separates the gas and water. Figure 3-1a shows a typical hydrocarbon reservoir located within an anticline, trapped by low-permeability shale above. The figure shows that hydrocarbon migration is controlled by the liquid water phase. This is one example of a hydrodynamically and structurally controlled reservoir. If there was no groundwater flow, hydrostatic equilibrium would develop, resulting in gas overlying oil, which in turn would overlie water. The phases would separate by horizontal interfaces.

The gas reservoirs in much of the Piceance Basin do not conform to conventional reservoir models (Cumella and Otsby, 2003; Johnson and Roberts, 2003). They are frequently located in very low permeability reservoirs ($k<10^{-17}$ m^2) of fine-grained sandstone with porosity less than 10 percent, and commonly less than 2 to 3 percent. These reservoirs are often abnormally pressured (either above or below hydrostatic) and lack discrete stratigraphic or lithologic seals. The gas reservoir is often a zone with gas saturation less than 50 percent such that water and gas coexist at the same elevation with neither phase dominant. That is, in low-permeability gas reservoirs, often there does not appear to be a distinct zone largely saturated with gas. Instead, a large vertical section of perhaps hundreds of meters may be filled with gas and water. This type of reservoir is depicted in Figure 3-1b. Additionally, the gas phase transgresses stratigraphic units because the pressure field is not controlled by lithologic contacts or structures, as is common with higher-permeability gas reservoirs.

Sometimes a separate gas phase is located below the water phase (Dahlberg, 1995). The reason is thought to be that groundwater percolation from outcropping reservoir rocks at the land surface balances the buoyant gas lower in the reservoir. This trap/reservoir requires very low permeability host rock, which is common throughout much of the Overthrust belt in Colorado. The reservoir in the Williams Fork Formation at Rulison is consistent with this model. These gas “deposits” are considered immobile at the time scales considered here (tens to hundreds of years). The gas phase remains stable because buoyancy forces are balanced by the downward migration of recharge water entering through outcrops along the edge of the basin.

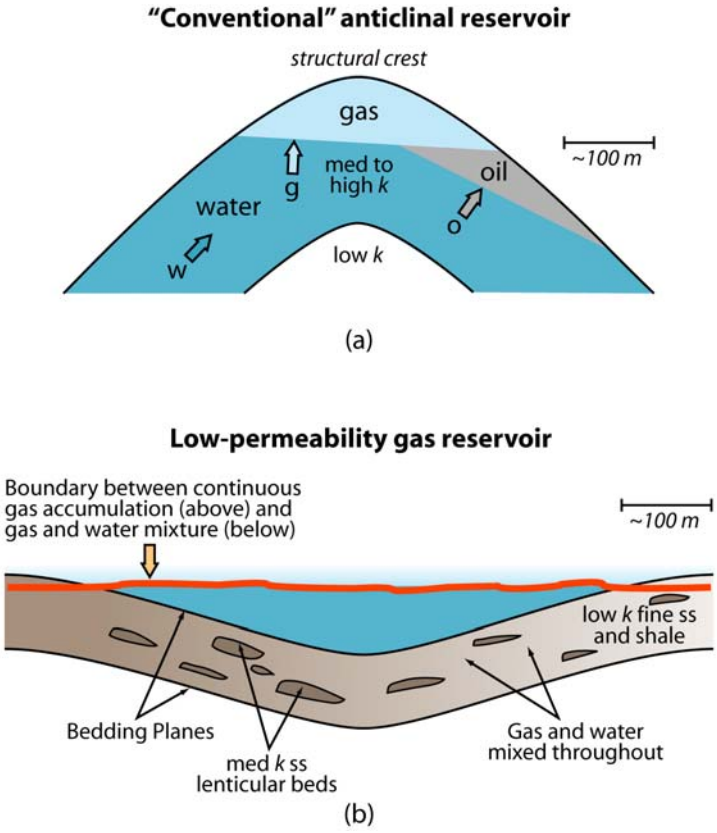

Figure 3-1. Example of a conventional gas reservoir located in an anticline (a) and one located in a low-permeability gas reservoir such as those found in the Piceance Basin (b). Both a structural and hydrodynamic trap are shown in (a), where the location of hydrocarbons is dependent upon both the permeability difference between formations and the direction and magnitude of subsurface water flow. In (b), the permeability of the "reservoir" is much lower than conventional reservoirs and is more typical of trap rock. The rate of production and transport of hydrocarbons is probably faster than the rate of fluid flow such that gas cannot escape at the same rate at which it is produced.

Despite this general immobility, gas will move through the reservoir by pressure-driven flow (e.g., in response to gas production wells). Components of the gas can also move by molecular diffusion, as well as exchange between phases. Aqueous phase diffusion is unimportant because diffusion coefficients are four orders of magnitude less than those in the gas phase. Low diffusion coefficients, coupled with low aqueous-phase velocities ($<10^{-11}$ ms^{-1}), are the reason that dispersion can be ignored in the aqueous phase. Movement of contaminants in the gas phase is almost always dominated by diffusion instead of mechanical dispersion, because the diffusion coefficient for gases, D, is approximately 10^{-5} m^2 s^{-1}. For gas flow through porous media, a maximum velocity could be 10^{-4} m s^{-1} (about 10 m day^{-1}), and a dispersivity (α) value (a characteristic pore diameter) for the Mesaverde Group sandstones could be 10^{-6} m. The mechanical dispersion coefficient, D_h, would be $D_h = \alpha u \sim 10^{-10}$ m^2 s^{-1}, which is five orders of magnitude smaller than the molecular diffusion coefficient for a typical gas. Gas dispersion is therefore not considered and is usually only of concern for very high velocity flow around boreholes.

Pressure-driven flow is mostly controlled by the permeability field in the Williams Fork Formation. Based on published outcrop studies, research and development projects (such as the Multiwell Experiment), and industry experience, four permeability zones are present in the gas reservoirs of the lower fluvial interval of the Williams Fork. These four zones are as follows: (1) siltstone/mudstone intervals, (2) sandstone intervals containing native fractures, (3) sandstone intervals with hydraulically generated fractures (hydrofracs), and (4) sandstone and siltstones containing fractures created by the nuclear explosion (Figure 3-2).

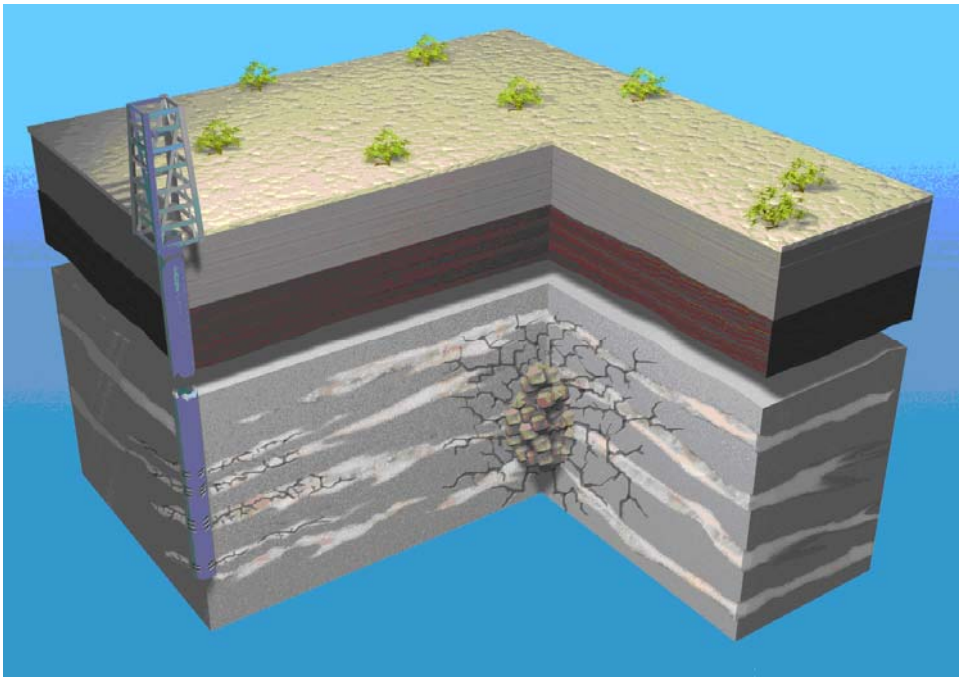

Figure 3-2. Conceptual model of the four permeability zones considered in the Rulison flow and transport numerical model. These zones are: impermeable shale (gray horizons), naturally fractured sandstone lenses (light tan layers), fractures caused by the nuclear test around the chimney, and hydrofractures from a simulated gas production well.

The first permeability zone consists of siltstone/mudstone layers that act as absolute confining intervals, which effectively isolate sandstone lenses from one another. Fractures in the sandstone, both natural and hydrofracs, terminate at the siltstone contact such that conductive pathways do not extend into the siltstone/mudstone layers.

The second permeability zone consists of the sandstone intervals imbedded in the siltstone/mudstone layers. Although more permeable than the siltstones/mudstones, they have very low matrix permeabilities such that in most environments they would not be considered conductive. Abundant permeability measurements on cores document sub-milliDarcy (less than 10^{-15} m^2) permeabilities (Sandia and CER, 1990). However, some sandstone lenses are fractured, which increases their permeability by an order of magnitude or more (Lorenz, 2003). Successful gas production depends on the presence of natural fractures. Because fracture patterns are not known for individual sand lenses, the conceptual model assumes that

all sandstones contain fractures, resulting in anisotropic permeability. The net reservoir permeability, as observed in producing gas wells in the basin, is related primarily to fracture anisotropy, which is assumed aligned with the stress field along a general east-west trend.

The predominant open natural fracture trend in the basin has a general east-west orientation (Cumella and Ostby, 2003), as do vertical fractures observed in the Parachute Field, where the Rulison nuclear test is located (Lorenz, 2003). In the adjacent Rulison field, the combined impact of permeability, anisotropy, and depositional direction result in reservoir drainage taking a preferential east-west direction (Kuuskraa and Ammer, 2004). Studies of the stress field at the MWX site found the preferred fracture orientation in that area to be N74 to 80°W (azimuth of 106 to 111°) (Myal *et al*., 1989; Koepsell *et al*., 2003; Warpinski *et al*., 1996). Few fractures are found with orientations other than a general east-west direction; outcrop studies indicate fracture strikes are within +/- 25 degrees of east-west, implying only one fracture set (Nelson, 2003).

The third permeability zone consists of hydraulically generated fractures in the sandstones. These fractures are created when wells are developed for production. The goal of hydraulic fracture treatments is to produce a long, highly conductive fracture along a single plane. Mahrer (1999), however, reviewed a variety of data regarding induced fracture geometry and concluded "that hydraulic fracture treatments are not pre-disposed to produce simple, clean, planar, bi-wing, fracture geometry in the far-field." Regardless of the complexity, hydraulic fracture azimuths should form in the same east-west direction of maximum stress as natural fractures. Fracture lengths that remain open and connected to the wellbore are uncertain, as are the hydraulic properties of the fractures. The conceptual model assumes the hydraulically fractured (hydrofrac) region is elongated in the east-west direction, has minimal width, has a height equivalent to the thickness of each sand lens penetrated in the stimulated well, and that fractures terminate at the contact between sand and siltstone.

The fourth permeability zone includes the fractures created by detonation of the nuclear device. The nuclear fracturing experiment in borehole Hayward 25-95A did not produce the focused stimulation pressure that an engineered hydraulic fracture can exert on a discrete sand lens. The concept of nuclear stimulation relied principally on the effective increase in "well" diameter represented by the nuclear chimney and the fact that the chimney would intersect multiple vertically stacked gas-bearing lenses (Rubin *et al*., 1972). Post-detonation drilling revealed a cylindrical, high-permeability nuclear chimney with a radius of 23.5 m and height of 83.8 m above the nuclear detonation point. Analysis of gas pressure during production indicated that the increased permeability region extended out to a radial distance of 2.75 chimney radii (about 63.7 m). Shear fractures extended 83.8 m, with the maximum extent of fracturing estimated at 132 m (AEC, 1973b). Production testing from a re-entry well revealed marginal enhancement in effective reservoir permeability (an increase of 0.01 milliDarcy (mD) [$10^{-17}m^2$] according to DeGolyer and MacNaughton, 1971).

As evidenced by the results of the Rulison nuclear test, the overall reservoir permeability is controlled by the naturally fractured sands. The hydrofracs serve as a pathway between the wellbore and the natural fractures, but long-term production is controlled by the character of the natural formation. Fractures are implemented in the model using an equivalent porous medium formulation, described in Section 4.

3.2 Conceptual Transport Model

The conceptual transport model can be considered in two parts. The first is the source of the radionuclides, including the manner in which they are released. The second part concerns the processes that occur during flow away from the source.

Radionuclides remaining after an underground nuclear test can be attributed to three sources (Borg *et al*., 1976): (1) residual nuclear material that has not undergone a nuclear reaction (unspent fuel), (2) direct products of the nuclear reactions (fission products and tritium), and (3) activation products produced by neutron capture in the immediate vicinity of the explosion. When the nuclear device is detonated underground, the cavity is initially filled with vaporized material derived from the rock and construction materials associated with the device and emplacement hole, as well as the radionuclide components. As the cavity cools, radionuclides are distributed into four phases: (1) in the nuclear melt glass, (2) as surface deposits on rubble in the cavity and chimney, (3) dissolved in water, or (4) as part of the gas phase (IAEA, 1998).

The total radiologic source term is not equally available for transport from the cavity. Most of the fission products are refractory (having low volatility) and are incorporated into nuclear melt glass. These will leach very slowly out of the glass as the glass itself slowly reacts with gases and liquids present in the subsurface. More volatile radionuclides, or those with a gaseous precursor (such as ^{137}Cs, which is produced by the decay of ^{137}Xe), occur both in the melt glass and as more easily dissolved deposits on rock surfaces. Though surface-deposited nuclides are more readily dissolved into groundwater than those in melt glass, many are reactive and tend to sorb strongly onto mineral surfaces. Several radionuclides are almost completely mobile in groundwater, with the most significant being tritium (^{3}H). Other highly mobile species are ^{85}Kr, ^{36}Cl, ^{129}I, ^{99}Tc, and ^{125}Sb (Smith *et al*., 1995).

At Rulison, the very low intrinsic permeability, coupled with significant gas-filled pore space, results in the liquid water phase being much less mobile than the gas phase. To the extent allowed by their solubility, radionuclides in the melt glass, in mineral phases, or sorbed onto surfaces will dissolve into the liquid phase. Some radionuclides can exist in the gas phase and therefore potentially move significant distances on the order of several hundred meters. The longer-lived of these radionuclides are ^{3}H, ^{85}Kr, ^{14}C, and ^{39}Ar (^{3}H and ^{14}C can also be found in liquid and solid phases). Investigations at the Gasbuggy nuclear gas-stimulation test identified that of these, ^{3}H and ^{85}Kr constitute the vast majority of gaseous radioactivity (Holzer, 1970). Tritium was the only radionuclide identified of concern in an assessment of the radiologic implication of use of natural gas from a nuclear-stimulated well (Jacobs *et al*., 1970). Krypton is not retained to any significant extent by the body, so the primary model of exposure is by immersion of the body in contaminated air. An environmental evaluation prior to the Rio Blanco gas stimulation test identified the ingestion of tritiated water (after incorporation in foodstuffs) to vastly dominate whole body exposure, as compared to immersion exposure to ^{3}H, or ^{85}Kr gases, or inhalation or skin absorption of tritiated water (AEC, 1972b).

A significant portion of the tritium produced by Rulison was believed to remain "bound in the solidified melt zone" (AEC, 1973b). Studies of nuclear tests conducted by the French in Africa report that more than 50 percent of available tritium is captured by melt glass (Dupuis, 1970, as reported by Borg, 1975), but recent analyses of contaminant transport

from underground tests in Nevada have assumed much less, or even zero, inclusion of tritium in melt. Tritium in the melt glass is present primarily as bound water dissolved in the glass, with minor amounts of gas trapped in vesicles (Borg, 1975). To be conservative, allowing transport of a larger quantity of tritium, the modeling presented here assumes that none of the tritium is contained in the melt glass and thus all of the tritium produced is available for gas transport. This is consistent with source term modeling performed for underground nuclear tests at the Nevada Test Site (NTS) (Tompson *et al.*, 1999).

As an isotope of hydrogen, tritium can form radioactive water, tritiated hydrogen gas, and methane (CH_4) molecules. Water exists in both gas and liquid phases, while methane exists (under reservoir conditions) in only the gas phase. The pressure and temperature conditions in the Rulison subsurface are not sufficient for an isotopic exchange reaction involving hydrogen to occur with methane (Frink and Wethington Jr., 1971; Burger, 1979; Wethington Jr., 1970). The tritiated methane observed during post-detonation gas-production testing was probably formed under the extremely high pressure and temperature conditions associated with the nuclear detonation. Tritium can also be present as hydrogen gas (either ^3HH or $^3H_2$), which can become dissolved in liquid water and partition between the two phases at equilibrium in accordance with Henry's Law. Virtually all tritiated methane and tritiated hydrogen gas were removed from the subsurface during production testing so that virtually all tritium remaining is associated with water (AEC, 1973b).

Tritium in the liquid water phase is always available for partitioning when the tritiated water vapor and liquid phases come into contact. The liquid phase is practically immobile (passive) and acts as a source/sink for tritium; in other words, a water vapor (gas) phase not containing tritium that comes in contact with a tritiated liquid phase will thermodynamically exchange tritium from the liquid to the vapor phase. Equilibrium exchange between ^3HH and H_2O was believed to occur during production testing at Rulison (Smith Jr., 1971). The modeling presented here includes tritium in the liquid and vapor phase of water and the capability of exchange between the two phases.

The radionuclides produced by the Rulison test were essentially restricted initially to the nuclear cavity. Minor amounts of radionuclide mass have been observed outside of some nuclear cavities at early time as a result of a process of "prompt injection." This is thought to be the result of pressures forcing volatile radionuclides into fractures. In all cases the amount of mass distributed away from the cavity is observed to be very small relative to the amount located inside. At Rulison, the gas production testing shortly after the nuclear detonation would draw gaseous radionuclide mass back to the chimney. As a result, it is assumed here that the entire tritium mass is initially located within the chimney.

Other than accounting for the tritium mass removed during the gas-production testing, other production testing processes are not included in the numerical model. This is a conservative approach in that diffusion of tritium away from the nuclear cavity would be inhibited during the production-test recovery period as fluid flowed toward the cavity replacing the produced gas. Instead, the conceptual model establishes steady-state flow conditions, then allows diffusion to occur as a result of the concentration gradient of tritium caused by the test. These are the conditions used to determine the nature and extent of contamination through time in the absence of gas-resource development. The possible impact of future production wells in the area is modeled by introducing a hydraulic gradient and adding an advective flow component to the transport analysis.

Both diffusive and advective transport are subject to processes that retard the migration of tritium. One of these is the exchange that occurs between tritium in the liquid and gas phases. With liquid-phase velocities much smaller than those in the gas phase, tritium exchanging into the liquid phase encounters a significantly retarded flow velocity. As tritiated gas migrates downgradient, it encounters tritium-free liquid water and exchange occurs, removing tritium mass from the faster pathway. The second significant process is radioactive decay. The tritium half-life is 12.32 years, decaying into nonradioactive helium. Thus, as time continues, the amount of tritium mass continually decreases. This accentuates the impact of exchange, because tritium transferred into the liquid phase is essentially removed by decay. No other sorption or retarding processes are included in the transport model.

THIS PAGE INTENTIONALLY LEFT BLANK

4.0 FORMULATION OF THE NUMERICAL MODEL

4.1 Choice of Numerical Simulator

The conceptual model includes flow and transport as fully coupled processes that must be solved simultaneously to get a realistic understanding of the radionuclide distribution within the reservoir. The Transport of Unsaturated Groundwater and Heat (TOUGH2) simulator (Pruess, 1991; Pruess *et al*., 1999) was used to implement the flow and transport model. TOUGH2 is a DOE-sponsored code that has been used to study heat and mass flow in geothermal reservoirs, saturated/unsaturated groundwater environments, and oil and gas reservoirs. TOUGH2 can simulate fully coupled, transient, three-dimensional, multiphase and multicomponent nonisothermal flow. The many applications in which TOUGH2 has been applied are discussed in several workshop reports (Pruess, 1995, 1998; see also http://www-esd.lbl.gov/TOUGH2/). The governing equations solved by TOUGH2 are presented in the appendix. Note that fracture flow is simulated here by using an equivalent porous medium approximation. TOUGH2 has a module capable of discrete fracture flow, but it is also based upon Darcy's law (which relies on a representative continuum) and demands data for fracture characteristics (e.g., aperture, spacing, and degree of connectivity) as well as hydraulic and transport properties (e.g., transmissivity, porosity, dispersivity) that are largely unknown for Rulison.

4.2 Simulation Domain

The simulation domain covers most of lots 11 and 12 and just the northern portions of lots 13 and 14 (Figure 4-1). This was chosen because the closest distance between the emplacement hole and a boundary of lot 11, in the east-west direction of preferential flow, is to the west.

A vertical cross section of the model domain is shown in Figure 4-2. The nuclear cavity/chimney has a radius of 20 m, while the fractures extend 60 m beyond it. Flow and transport is toward a hypothetical producing natural gas well, located 258 m to the west. The production well in lot 12 is located 73 m from the boundary of lot 11.

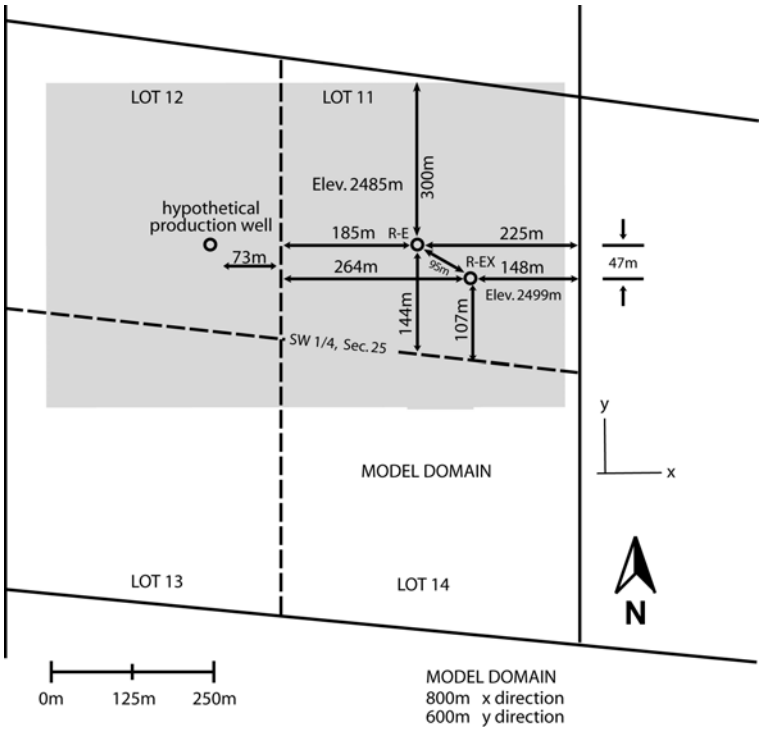

Figure 4-1. Simulation domain relative to lot boundaries.

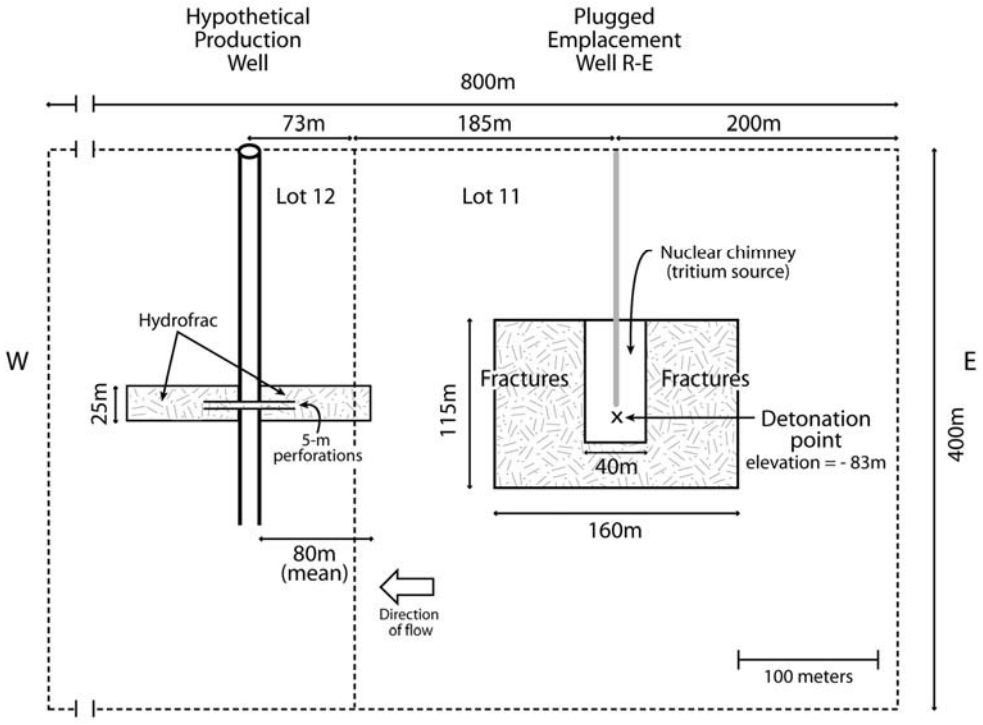

Figure 4-2. Diagrammatic vertical cross section of the model domain, in an east-west slice. The mean length of the hydrofracs is 85 m (modeled as 80 m given the grid discretization); the hydrofrac length is a random variable in the simulations. The top of the domain is 2,368 m below the land surface.

4.3 Boundary Conditions

In the accompanying figures, flow is generally from east to west, from the nuclear chimney located in lot 11 to a production well in lot 12. The hydraulic and transport boundary conditions for the three-dimensional computational domain are shown in Figure 4-3. The upgradient hydraulic boundary condition on the vertical plane is prescribed hydrostatic pressure. To establish hydrostatic pressures, the bottom pressure was prescribed at 20.3 MPa (Coffer *et al.*, 1971) and the vertical pressure distribution was developed in a one-dimensional simulation of a column. This same boundary condition is established at the downstream (west) vertical plane. The hydraulic boundary conditions on the vertical planes to the north and south are no flow.

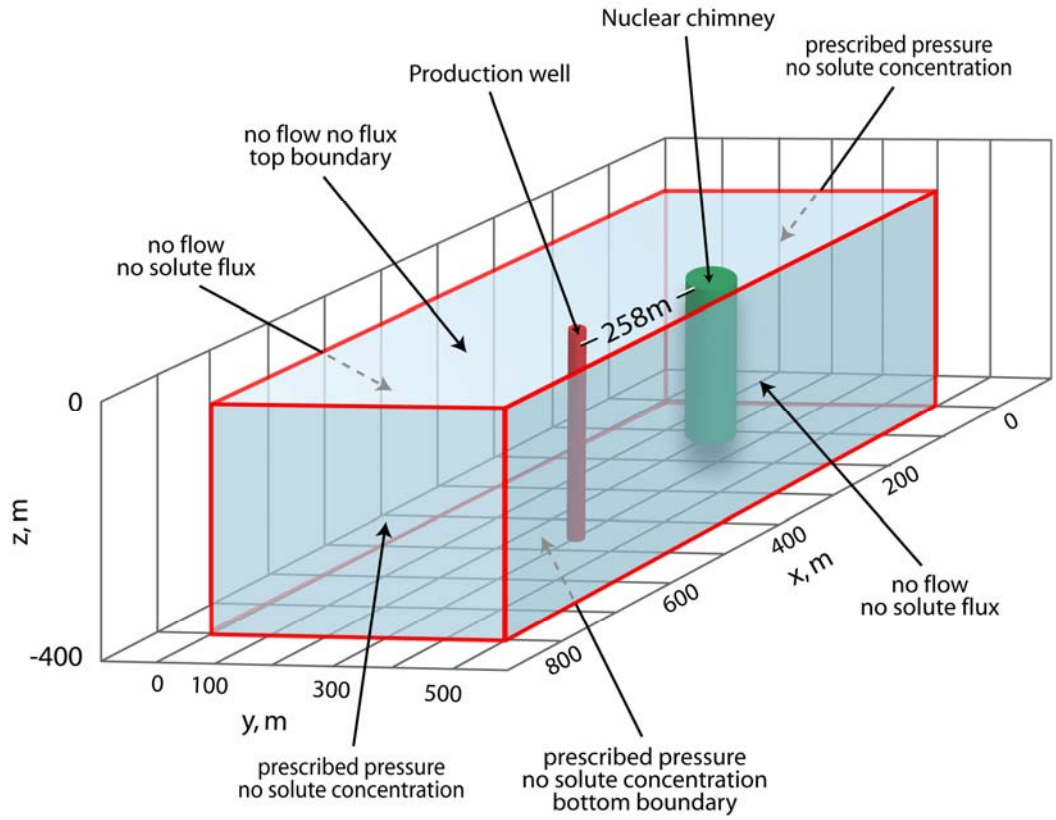

Figure 4-3. Hydraulic and transport boundaries for the simulations.

The horizontal hydraulic boundary conditions are zero flux at the upper boundary and prescribed pressure (20.3 MPa) at the lower boundary. The combination of these two boundary conditions results in a static, steady-state, uniform vertical distribution of moisture contents as are observed from the data (values of liquid saturation are around 50 percent). The combination of zero flux at the top and prescribed pressure at the bottom is the only combination that results in this situation (Figure 4-4a). For comparison, the other three combinations of boundary conditions are presented in the Figure 4-4. Figure 4-4b shows the liquid saturation profile through a 1,200-m column when no-flux conditions are applied at the top and bottom. No mass is allowed to enter the domain, so the upper profile drains to residual liquid saturation (0.45) and ponds at the bottom. A liquid saturation profile for

applied pressures applied to both boundaries is shown in Figure 4-4c. This combination allows mass to enter the domain from above and/or below, depending upon the hydraulic gradient. For a downward-acting gradient, liquid water moves downward while the gas phase (methane and water vapor) moves upward. This combination of boundary conditions may result in a dynamic steady state, one in which constant liquid and gas fluxes are reached, but the gas velocities are great enough such that the travel time to the land surface is on the order of tens to hundreds of years. This combination of boundary conditions was disregarded, as this would not contain gas in a reservoir. Finally, a combination of prescribed pressure at the top and no flux at the bottom results in downward drainage of water into the domain to the point of liquid saturation (Figure 4-4d).

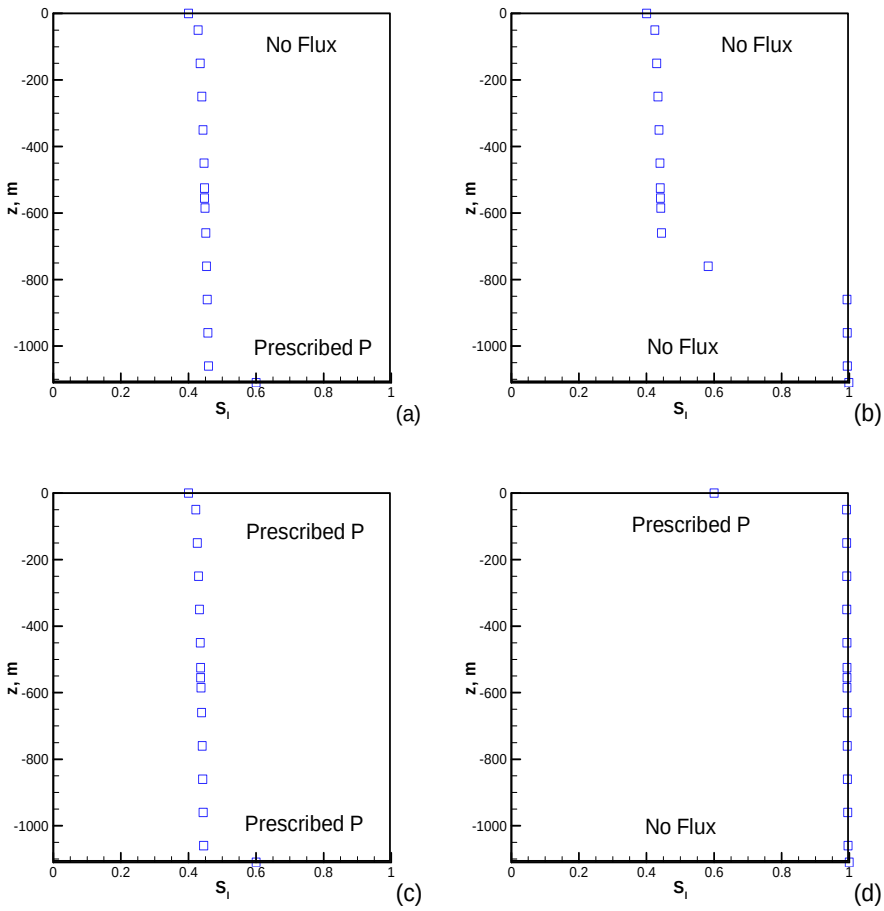

Figure 4-4. Liquid saturation profiles resulting from steady-state simulations for four combinations of horizontal hydraulic boundary conditions for one-dimensional flow in a 1,200-m vertical column. The terms "No Flux" and "Prescribed P" refer to the two types of boundary conditions used in the model. Each simulation was carried out for 10^6 yr. Gas velocities (not shown) are upward.

The six transport boundary conditions coincide with the hydraulic boundary conditions of similar type. That is, conditions of prescribed solute flux coincide with prescribed (hydraulic) flow, while prescribed mass fraction (a normalized concentration, described below) of tritium as tritiated water (X_l^{THO} and X_g^{THO} for the liquid and gas phases,

respectively) coincides with prescribed pressure. The transport boundary conditions are, therefore, no prescribed (zero) mass fraction on the vertical boundaries to the east and west, and no solute flux on the vertical boundaries to the north and south. The lower boundary condition was prescribed as zero mass fraction (i.e., concentration of tritium), while the upper boundary condition was prescribed zero mass flux tritium.

The dimensions are 800 m in the *x*-direction, 500 m in the lateral *y*-direction, and 400 m in the vertical *z*-direction. The grid was divided evenly into 86,100 grid blocks, each 20 m x 20 m x 5 m in the *x*-, *y*-, and *z*-directions, respectively.

Although the computation domain is oriented such that the main direction of flow is toward a pumping well to the west, it could be oriented in any direction, as there is no regional pressure gradient controlling flow. Neither is there any structural feature that is part of the flow domain. There is, however, anisotropy included in the hydraulic conductivity field that favors flow in the east-west direction, aligned with the principal stress field and thus presumably with open fractures. The production well could be viewed just as easily as being to the east. The production well was placed to the west, as the western boundary of lot 11 is closer than the eastern boundary of lot 11 (recall that drilling is restricted within lot 11 itself).

4.4 Geologic Model Formulation - Generation of Conditional Random Fields

There is significant uncertainty regarding the geometry of the hydrogeologic units (sandstone lenses interbedded within shale) in the model domain, due to spatial variability in the stratigraphic units and limited measurements within the modeling domain. To account for this uncertainty, the hydrogeologic units are treated as random variables. Conditional random realizations of the sandstone and shale geometry were generated for the model using probability distributions of the random parameters as described below.

As shown in Figure 2-5, the two rock types of sandstone and shale are identified based on geophysical log information at the Hayward 25-95A (R-E) and Hayward 25-95 (R-EX) wells. The geometry of sandstone lenses has a significant impact on the flow and tritium transport. Spatial distribution of the sandstone and shale at the two wells can be quantified by categorical (indicator) geostatistics

$$I_k(\mathbf{x}) = \begin{cases} 1 \text{ if facies } k \text{ exists at location } \mathbf{x} \\ 0 \qquad\quad \text{otherwise} \end{cases} \tag{1}$$

In the Rulison case, at any depth along the two wells, if sandstone is present and shale is absent, an indicator set of (1,0) is assigned to the point; otherwise, (0,1) is used. Spatial variability of the rock types can be measured by transitional probability, $t_{jk}(\mathbf{h})$, defined as

$$t_{jk}(\mathbf{h}) = \Pr\{k \text{ occurs at } \mathbf{x}+\mathbf{h} | j \text{ occurs at } \mathbf{x}\} \tag{2}$$

which is a conditional probability that a unit *k* occurs at location **x**+**h** (**h** being a lag or separation vector), given that a unit *j* is present at location **x**. After determining the indicator sets at 1-m intervals of the two wells in Figure 2-5, the vertical transition probability is calculated using the GAMEAS subroutine of the T-PROGS computer program (Carle, 1999), and plotted in Figure 4-5. The two figures at diagonal positions (upper left and lower right) are transition probability within the rock types of sandstone and shale, respectively; the two

off-diagonal figures represent the transition probabilities from one to the other. Volumetric proportions of the two units, calculated by GAMEAS, are 49 percent for the sandstone and 51 percent for the shale. This is consistent with the volume proportion of sand identified both regionally and in the site logs. Shale is selected as the background unit, due to its greater presence. Whenever the sandstone is absent, the background unit, shale, fills in the space.

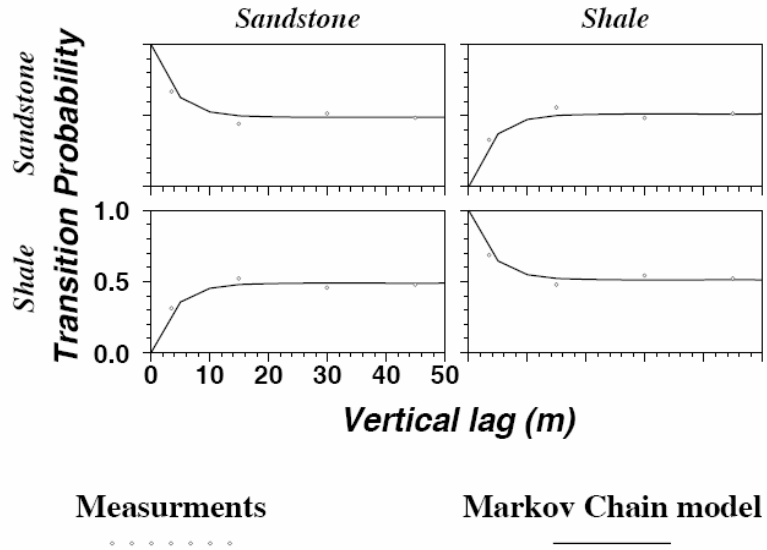

Figure 4-5. Matrix of vertical transition probability obtained from measurements (circle) and fitted Markov chain model (line). "Lag" refers to the separation distance between measurements.

The transition probability can be modeled by a Markov chain model, which assumes that spatial occurrence of a unit depends entirely on its nearest unit. The transition probability/Markov chain approach of modeling spatial variability enables one to integrate readily observed geologic information such as volumetric proportion and mean unit lengths (e.g., thickness and width). A Markov chain model is fitted to the vertical transition probability using the MCMOD subroutine of T-PROGS. The option of using embedded Markov chain is for the fitting, since it does not require information of the background unit (shale); data regarding the shale are very sparse in comparison with that of sandstone. Figure 4-5 plots the Markov chain model using the GRAFXX subroutine of T-PROGS. It shows that the fitted models agree well with measured transition probabilities. The model stabilizes at volumetric proportions at large lag, which are 49 percent and 51 percent for sandstone and shale, respectively, as calculated by the GAMEAS subroutine. For a given unit, the slope of its transition probability is the mean length of the unit. For example, the vertical transition probability in Figure 4-5 shows that the mean thickness of sandstone is 7.5 m, which is obtained by trial and error until the best fit is obtained. The fitted mean length of 7.5 m agrees with the observed reservoir thickness of 6.1 m to 15.2 m at the MWX site (Sandia and CER, 1990). At the Hayward 25-95A (R-E) well, the thickness of the sandstone ranges from 1.0 m to 23.8 m, with an average of 7.3 m; at the Hayward 25-95 (R-EX) well, the thickness of the sandstone ranges from 0.6 m to 17.1 m, with an average of 4.0 m. Mean thickness of the shale is not needed for the fitting, since the embedded Markov chain is used.

Lateral spatial variability cannot be measured quantitatively, since the two available wells are insufficient to estimate transition probability in the horizontal direction. In addition, there are no secondary measurements (e.g., soil survey in Weissmann *et al*., 1999; outcrops in Dai *et al*., 2005) to facilitate the analysis. Therefore, information of horizontal mean length (width) available in the literature is used to model horizontal transitional probabilities. Based on a study of outcrops stratigraphically equivalent to the production intervals, Cole and Cumella (2004) reported a range of width of 12.2 m to 850.7 m, with an average of 161.1 m. Sandia National Laboratories and CER (1990) gave a similar range of 304.8 m to 762 m for the MWX site, while Lorenz (1990) reported a smaller range of 62.5 m to 320.0 m. The mean width of 161.1 m of Cole and Cumella (2004) is used as the mean width of sandstone given that their work used surface exposures as compared to the subsurface sampling at the MWX site. Again, mean width of the shale is not needed for the embedded Markov chain model. The horizontal Markov chain model of transition probability is estimated using the MCMOD subroutine of T-PROGS, and plotted in Figure 4-6. The long mean length of sandstone renders a layering structure of the unit in the simulation domain. On the other hand, since the mean length is smaller than the domain size with a length of 800 m and width of 490 m, the two units of sandstone and shale can be observed in one layer.

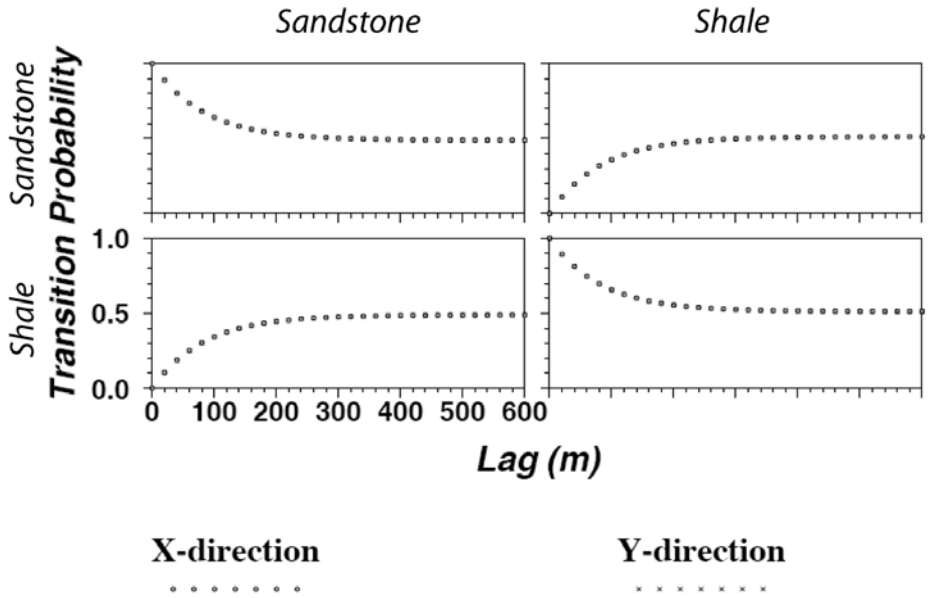

Figure 4-6. Matrix of the Markov chain model of horizontal transition probability calculated using the MCMOD subroutine in the T-PROGS computer program.

Five hundred conditional realizations of sandstone and shale geometry are generated using the TSIM subroutine of T-PROGS. Occurrence of the two units at wells Hayward 25-95A and Hayward 25-95 is used as conditioning data so that generated occurrence of the units at the two wells is the same as the measurements in every realization. A strike angle of N 75^{o} E reported by Cole and Cumella (2004) is used in the generation. Figure 4-7 plots four conditional realizations selected arbitrarily. Sandstone and shale are denoted by 1 and 2, respectively. Conditioning data are also plotted in red to illustrate the conditioning effect. While sandstone and shale locations and length are random, occurrence of each unit at the two conditioning wells is fixed. Layering structure is well depicted in the

realizations, due to the small mean thickness and large mean width. On the other hand, sandstone and shale can be observed at the same horizon, since the mean width is smaller than the domain size. The T-PROGS mesh for the random field generation is the same as the TOUGH2 mesh used for numerical simulation, except that the sizes of the boundary blocks in the T-PROGS mesh are larger that those of the TOUGH2 mesh. The generated sandstone and shale geometries are carried forward as the framework of the TOUGH2 simulation so that uncertainty of tritium transport due to the sedimentary units can be assessed through Monte Carlo simulation.

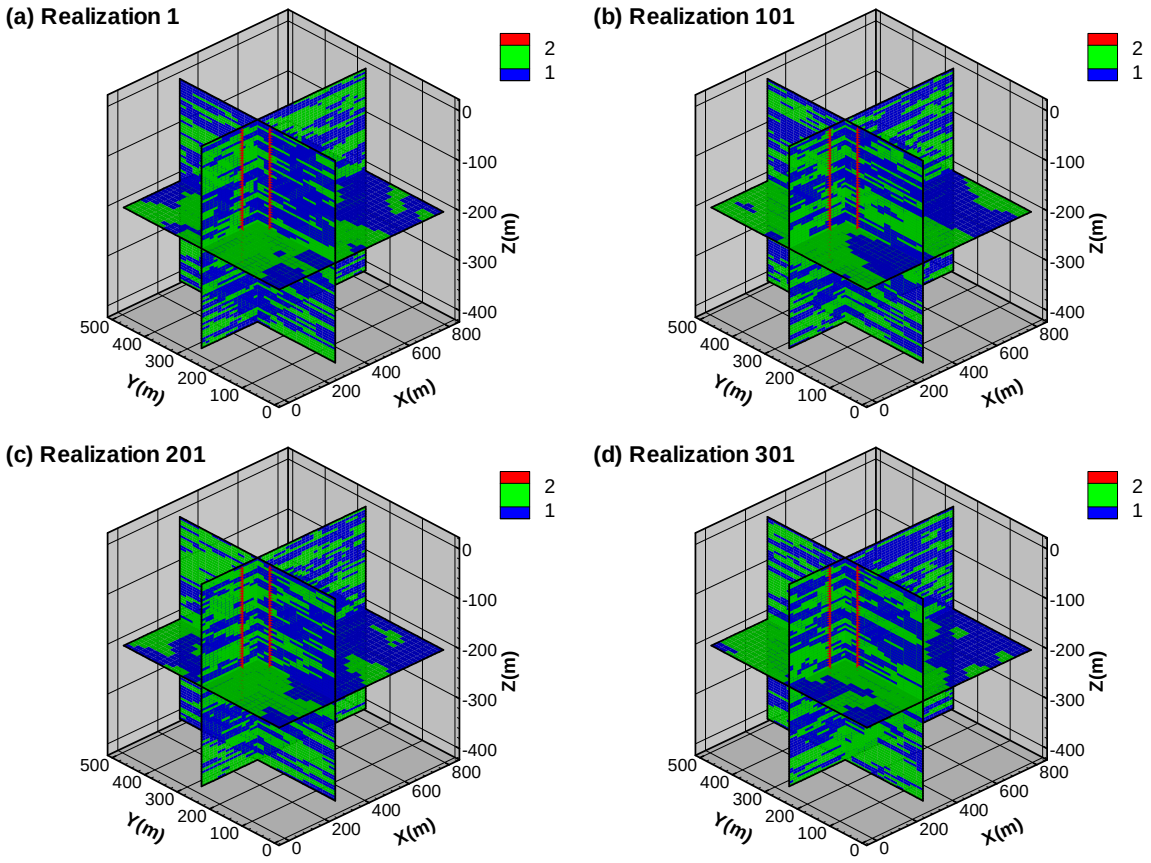

Figure 4-7. Four conditional random realizations of sandstone (denoted by 1) and shale (denoted by 2). Conditioning data are marked in red. The top of the simulation is 2,368 m below the land surface.

4.5 Flow Model Properties

Significant uncertainties are present for models of subsurface flow conditions, many of which are related to uncertainties in parameter values and in their spatial distribution. Some of this uncertainty is included within the model by sampling from possible ranges of parameters rather than using single, deterministic values. The decision to treat a parameter as deterministic or stochastic is made qualitatively. A parameter may be handled as stochastic if its reasonable range could significantly affect the model outcome (i.e., sensitivity). For example, intrinsic permeability and porosity of sandstone are considered as stochastic

variables, while those of shale are set as deterministic. A parameter may be treated deterministically if it is known with certainty, or if the model is considered insensitive to its possible range of values relative to other parameters, particularly if there is no information to determine its distribution and only one best estimate is available. Seven parameters are treated stochastically in the Rulison model (Table 4-1). The selection of their distributions, based on measurements and available qualitative information, is described in the following sections. Sources for the deterministic parameters are presented in Table 4-1, and some of these are also discussed in subsequent sections.

4.5.1 Liquid and Gas Properties

As distributed by DOE, TOUGH2 does not have the capability to model methane as the principal component of the gas phase. Modifications were therefore made to replace air with methane as the primary component of the gas phase. The modifications were to change the molecular weight of air to that of methane (16.05 g mol^{-1}), and to change some values in the correlations used to compute dynamic viscosity. TOUGH2 estimates viscosity based upon the Chung method (Reid *et al*., 1987), so values for the characteristic diameter of the molecule, characteristic energy, and the collision integral were replaced with values correct for methane. The parameters were taken from Appendix B of Reid *et al*. (1987). However, the steam tables, in which liquid water and water vapor partitioning in air is determined, were not modified.

As implemented with the EOS7r equation of state module, TOUGH2 solves equations for two phases (gas and liquid [or aqueous]) and five components: water, methane (replaces air), brine (not considered), radionuclide 1 (tritiated water), and radionuclide 2 (helium, though it is not radioactive and is ignored). Radionuclide 2 is the decay component of radionuclide 1, and its behavior is ignored in the results. The gas phase is composed of methane, water vapor, tritiated water vapor, and helium. The liquid phase is composed of water, tritiated water, dissolved methane, and dissolved helium. Except for a single simulation in which the effect on tritium transport of a 226ºC chimney was investigated, all simulations were isothermal. For this nonisothermal simulation, an additional energy balance equation was included in the calculations.

4.5.2 Rock Properties

4.5.2.1 Intrinsic Permeability

Nuclear Cavity and Chimney: Given the horizontal and vertical discretization of the model (20 m in the horizontal *x*- and *y*-directions, 5 m in the vertical *z*-direction), the Rulison cavity is represented by a column of blocks 2 by 2 cells wide and 22 cells high (Figures 4-8 and 4-9). This is roughly equivalent to an r_c of 20.1 m and a total chimney extent of 109.7 m (which accounts for 83.8 m of chimney height above the working point plus the cavity radius below the working point).

Table 4-1. Ranges and distribution of random parameters and values of deterministic parameters used for modeling. Intrinsic permeabilities are isotropic unless otherwise noted (i.e., *x*-direction, *y*-direction, *z*-direction). Values for which no references are given are the best estimates based upon nonspecific literature.

Random Parameters				
	Minimum	Mean	Maximum	Distribution
Intrinsic permeability *x*-dir., sandstone, m^2	2.70×10^{-19}	1.50×10^{-16}	2.95×10^{-15}	Log normal
Intrinsic permeability *y*-, *z*-dir., sandstone, m^2	2.42×10^{-20}	2.63×10^{-18}	3.27×10^{-17}	Log normal
Anisotropy ratio (k_x/k_y)	10	55	100	Uniform
Intrinsic permeability *x*-dir., hydraulic fractures, $m^{2\dagger}$	2.70×10^{-17}	1.50×10^{-14}	2.95×10^{-13}	Log normal
Intrinsic permeability *y*-, *z*-dir., hydraulic fracs, $m^{2\dagger}$	2.42×10^{-18}	2.63×10^{-16}	3.27×10^{-15}	Log normal
Porosity, sandstone	0.0008	0.0529	0.105	Normal
Hydrofrac length	35	85	182	Log normal
Deterministic Parameters				
		Value		Source
Intrinsic permeability, shale, m^2		1×10^{-20}		Randolph, 1983
Intrinsic permeability, nuclear chimney, m^2		9.87×10^{-13}		Reynolds *et al*., 1970
Intrinsic permeability, explosion-related fractures, m^2		2.96×10^{-16}		Rogers and Reynolds, 1972
Relative permeability		$K_l=S^4$		Corey, 1954
Capillary pressure curve		TRUST fit		Pruess *et al.,* 1999
Porosity, shale		0.07		Randolph, 1983
Porosity, nuclear chimney		0.34		Geometrically derived
Porosity, explosion-related fractures		0.10		
Porosity, hydraulic fractures		0.10		
Rock grain density, kg m^{-3}		2,680		
^3H radioactivity, liquid and gas, Ci		6941		Smith, 1971; AEC, 1972a
Diffusion coefficient, THO in methane, m^2 s^{-1}		7.26×10^{-5}		Cussler, 1997
Diffusion coefficient, THO in liquid water, m^2 s^{-1}		3.47×10^{-9}		Mills, 1973
Diffusion coefficient, He in methane, m^2 s^{-1}		6.75×10^{-5}		Cussler, 1997
Diffusion coefficient, He in liquid water, m^2 s^{-1}		6.28×10^{-9}		Cussler, 1997
Diffusion coefficient, CH_4 in liquid water, m^2 s^{-1}		1.49×10^{-9}		Reid *et al*., 1987 (calculated)
Diffusion coefficient, ^{85}Kr in methane, m^2 s^{-1}		2.62×10^{-5}		Reid *et al*., 1987 (calculated)
Diffusion coefficient, ^{85}Kr in liquid water, m^2 s^{-1}		1.32×10^{-9}		Mills, 1973
^3H half life, yr		12.32		Parrington *et al*., 1996
Rock grain specific heat, J kg^{-1}		1,000		
Thermal conductivity (unsaturated) of rocks, W m^{-1} ºC		2		
Initial Conditions				
		Value		Source
Liquid saturation		0.5		Frank, 1971
Formation pressure (gas static), MPa		20.3 at base		Coffer *et al.,* 1971
Reservoir temp., ºC		101		Smith, 1971
Mass fraction tritiated water in aqueous phase, kg^{THO} kg $liquid^{-1}$		1.57×10^{-10}		(calculated)

†: Intrinsic permeability of hydraulic fractures is increased from that of natural sandstone by a factor of 100.

Observations made at the NTS suggest that intrinsic permeability within a nuclear chimney is highly variable (Borg *et al*., 1976). Extremely low permeabilities are associated with areas at and below the nuclear detonation point where melt accumulates, whereas upper areas have an increased number and size of voids that should result in high permeability. Quantitative estimates of permeability are rare. Borg *et al*. (1976) report permeability estimates determined by monitoring chimney pressure during air injection. However, it is possible that the voids are so large that the concept of permeability does not apply, that is, that flow in the chimney is not properly modeled as flow through porous media. This limitation is overcome by realizing that, in the model, the chimney radius is only 20 m, while the distance from the detonation point to the hypothetical production well is 258 m.

No direct estimates were made for Rulison, but it is assumed here that large, well-connected pores are present in the chimney, with the zone at the bottom neglected where the nuclear melt glass collected and solidified. Reynolds *et al*. (1970) assigned a value of 9.87 x 10^{-13} m^2 (1,000 mD; 1 mD = 9.87 x 10^{-16} m^2) to the chimney for modeling they performed. Though they note this was arbitrarily selected, it is consistent with the limited NTS data (Borg *et al*., 1976) and was used here for an isotropic permeability throughout the cavity and chimney.

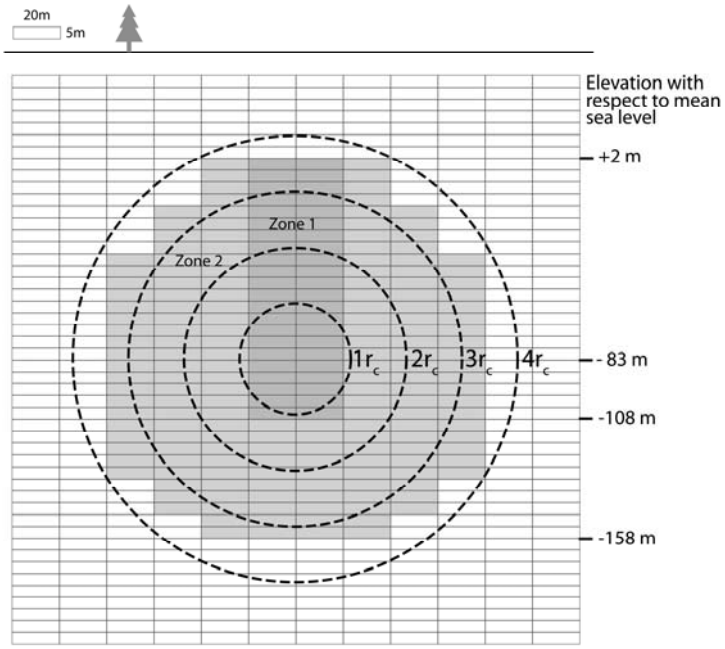

Figure 4-8. Partial cross section of model grid around the chimney showing the assignment of cells to the chimney region (zone 1) and the nuclear-fractured region (zone 2). Also shown are the estimated cavity (with a radius of approximately 23.5 m) and multiples of the cavity radius away from the zero point where the nuclear device was located.

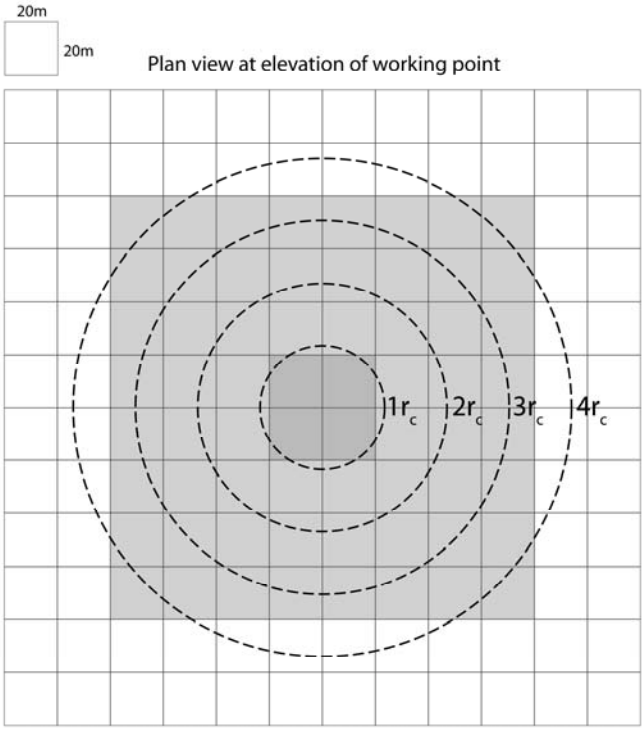

Figure 4-9. Same as Figure 4-8, but shown in plan view, looking down from above.

Nuclear-stimulated Zone: By matching Rulison gas-production test data, Lawrence Livermore National Laboratory estimated values for permeability height (equivalent to a transmissivity) for the enhanced permeability zone caused by the nuclear test (from 23.2 to 63.1 m away from the detonation, outside the cavity but within the intensively fractured zone), as well as the far-field beyond 63.1 m (Rubin *et al*., 1972). They concluded that the test data were best matched by an increased permeability region with a 33-fold increase over the undisturbed formation permeability extending from the chimney wall out to a radial distance of 2.75 r_c. Rogers and Reynolds, Jr. (1972) applied a net sand interval of 22.9 m to the Lawrence Livermore National Laboratory analysis to obtain a permeability for the far-field of 8.9 x 10^{-18} m^2 (0.009 mD). Applying the same thickness to the fracture zone results in a permeability for the nuclear fractured interval of 2.96 x 10^{-16} m^2 (0.3 mD). Using a thicker interval, such as the full chimney height, results in a smaller permeability estimate. DeGolyer and MacNaughton (1971) also matched the production data after the nuclear test, and used a different model to postulate "ultimate" permeabilities of concentric fracture zones varying from 2.96 x 10^{-16} m^2 (0.3 mD) closest to the cavity to 3.95 x 10^{-17} m^2 (0.040 mD) at the edge of the fracture radius. Their model included the fracture zone being dewatered as production progressed, such that early time permeabilities were lower.

The site-specific information described above suggests that the permeability in the nuclear fractured zone is on the order of 3 x 10^{-16} m^2 (0.3 mD) or less. The nuclear fracture zone is represented by an additional three blocks outside the cavity zone in each direction at the elevation of the working point. This represents a fracture zone with a radius of about 80.2 m. It is assumed that the nuclear fractures create an isotropic network leading to a uniform increase in permeability throughout the nuclear fractured zone. This is consistent

with the general nuclear test experience that the zone within 2.5 to 4 r_c is pervasively fractured, and consistent with the great depth of burial, and thus large overburden pressure, of the Rulison test.

Sand Intervals with Natural Fractures: Based on gas-production testing in well Hayward 25-95 (R-EX), conducted after hydraulic fracturing, permeability in the region around the Rulison test was estimated to be 7.9 x 10^{-18} m^2 (0.008 mD) prior to the nuclear detonation (Reynolds *et al*., 1970; Coffer *et al*., 1971). Different analytical techniques applied to the same data resulted in permeability values ranging from 5.3 x 10^{-18} to 1.04 x 10^{-17} m^2 (0.0054 to 0.0105 mD), but these were considered less reliable (Reynolds *et al*., 1970). Production testing after the nuclear detonation resulted in estimates of far-field permeability (beyond the impact of nuclear-generated fractures) of 8.9 x 10^{-18} m^2 (0.009 mD; Lawrence Livermore National Laboratory estimate reported in Rogers and Reynolds, 1972) to 3.95 x 10^{-17} m^2 (0.04 mD; DeGolyer and MacNaughton, 1971). Permeability measurements of core from well Hayward 25-95A (RE) range from 1.38 x 10^{-18} to 2.47 x 10^{-18} m^2 (0.0014 to 0.0025 mD) at confining pressure (Quong, 1972). Quong (1972) notes that his values are lower than those based on production tests and postulates that this reflects the effect of flow mechanisms beyond the scale of the cores. He also reports a core measurement made by the U.S. Bureau of Mines of 6.02 x 10^{-18} m^2 (0.0061 mD).

Various assessments have been made of the permeability of the Williams Fork Formation fluvial sands in the region. The Rulison feasibility study reports a median permeability of 4.9 x 10^{-16} m^2 (0.5 mD) for the Mesaverde Group (Austral Oil Company and CER, 1966), a value that today appears significantly optimistic. As part of the Piceance Basin Continuous Gas Assessment Unit, the Williams Fork Formation reservoirs are reported as generally having permeabilities of 9.87 x 10^{-17} m^2 (0.1 mD) or less (Johnson and Roberts, 2003). Cumella and Ostby (2003) summarize permeability of productive Williams Fork Formation as ranging from 9.87 x 10^{-20} to 1.97 x 10^{-18} m^2 (0.0001 to 0.002 mD). Reeves *et al*. (1999) report a range of 4.94 x 10^{-18} to 9.87 x 10^{-17} m^2 (0.005 to 0.1 mD) for the permeability of the Williams Fork Formation in the Rulison, Parachute, and Grand Valley gas fields.

The Multiwell Experiment is the most abundant source of permeability data for the fluvial sands of the Williams Fork (Sandia and CER, 1990). These data come from the analysis of over 610 m of core, detailed log analysis and interpretation, and analysis of production testing using both analytic and modeling techniques to match pressure histories. The MWX researchers found that the fluvial sandstones have matrix permeabilities of less than 9.87 x 10^{-19} m^2 (0.001 mD) under *in situ* conditions of stress and water saturation, but that the overall permeability is 9.87 x 10^{-18} to 1.48 x 10^{-17} m^2 (0.01 to 0.015 mD). They concluded that the fluvial interval was characterized by relatively wide, heterogeneous, low-permeability sandstones, which contain a complex anisotropic natural fracture system that controls the overall reservoir permeability.

Dry Klinkenberg permeability measurements, collected at several values of overburden pressure, are recorded for hundreds of samples from the lower fluvial interval at the MWX site (Sandia and CER, 1990). Datasets were developed by digitizing data from figures (Sandia and CER, 1990), evaluating data tabulated and evaluated by Kukal and Simons (1986), Randolph (1983), and Soeder and Randolph (1987), and by selecting values from the raw data sheets presented in Appendix C of the MWX Lower Fluvial report (Sandia and CER, 1990). One limitation on all of the data is that it is not readily differentiated based

on lithology. The samples reported in Appendix C of the MWX report (Sandia and CER, 1990) (Core Laboratory data) were cross-referenced with the petrographic data presented in Appendix B of the MWX report to cull values gathered from siltstone and mudstones. A smaller dataset that could be positively associated with particular reservoir sand bodies from figures in the MWX report was used for comparison to the larger core dataset and indicated that the two represented similar populations. Ultimately, the culled dataset from Appendix C was selected to represent the distribution of matrix permeability (Figure 4-10). Permeability at 3,000 psi was used, though the depth at the Rulison test site is under greater confining stress (the values at 4,000 psi are lower).

Though the MWX reservoir behavior was successfully simulated using isotropic assumptions (Sandia and CER, 1990), most workers favor treating the reservoir as anisotropic, with higher permeability aligned in the direction of the predominant fractures. Highly elliptical reservoir drainage patterns occur in a reservoir with subparallel regional fractures, with the long axis of the ellipse aligned with fracture strike. Lorenz (2003) states that "system permeability transverse to fracture strike is low, nearly the matrix value, but horizontal effective permeability along fracture strike has been documented to be up to a hundred times that of the matrix."

Given the similarities in sedimentology and structure at the MWX and Rulison sites, the extensive data developed for the MWX site are used to guide parameter values at Rulison. An anisotropy between 1:10 and 1:100 is assumed. Since no other information is available, a uniform distribution is used to describe variation of the anisotropy. The uniform distribution can be updated to other more informative distributions (e.g., triangle), if more information becomes available. The mean permeability in the nonfractured direction is assigned a value of 2.63×10^{-18} m^2 (0.0027 mD), based on the MWX data described above (which has a mean of 2.28×10^{-18} m^2; Figure 4-10). The permeability in the fracture direction (east-west, as discussed elsewhere), is selected as a value 10 to 100 times (the exact multiple is randomly selected from a uniform distribution between those values) the matrix value. The permeability in the fracture direction is thus consistent with the magnitude determined for the reservoir from production tests (which in turn are governed by flow through the fractures), with a mean of 1.5×10^{-16} m^2 (0.15 mD). As discussed below, the intrinsic permeability in the nonfractured direction follows a lognormal distribution. Consequently, the intrinsic permeability in the fracture direction also follows a lognormal distribution.

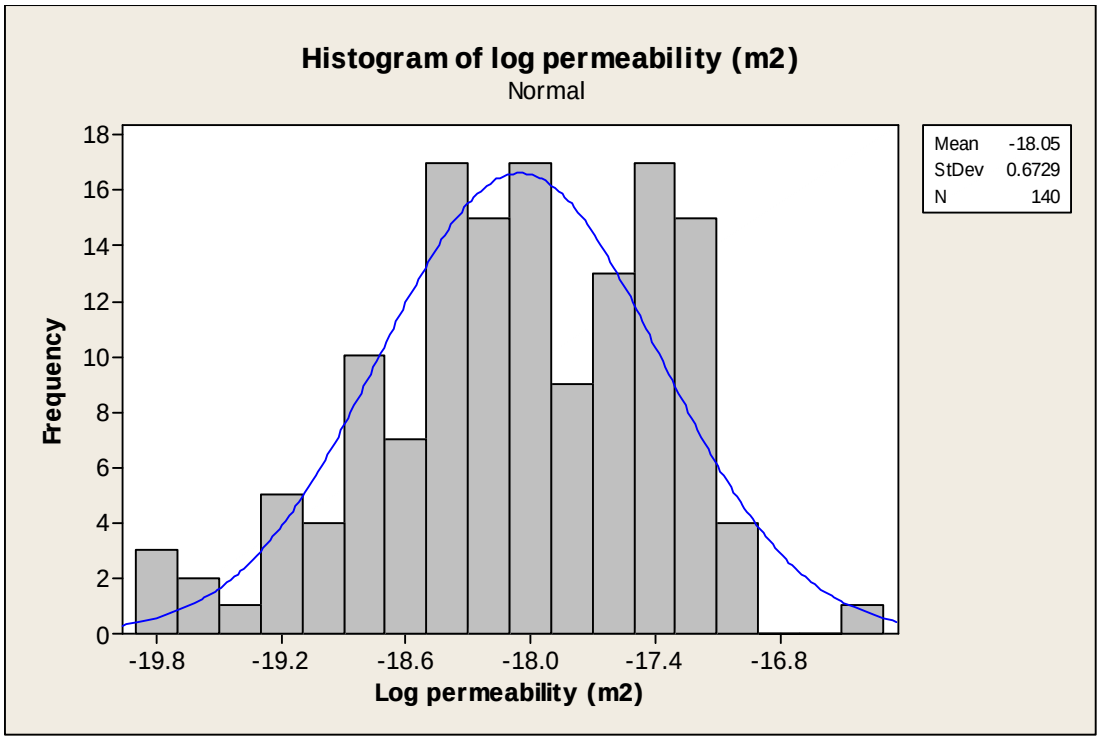

Figure 4-10. Histogram of log permeability (m^2) of sandstone and a fitted normal distribution using MINITAB.

Permeability of Hydraulic Fracture Zone: There is considerable uncertainty in regard to permeability of hydraulic fractures. Workers at the MWX site estimated a minimum fracture permeability range of 3.16×10^{-14} to 1.58×10^{-13} m^2 (32 to 160 mD) for a hydrofracture in the coastal-facies stratigraphic interval of the Mesaverde Group (Sandia and CER, 1989). Well test analysis of hydraulic fracture zones in tight sands in seven wells in the Green River Basin give a range of permeabilities of less than 9.87×10^{-18} to 5.9×10^{-17} m^2 (0.01 to 0.06 mD) (Reeves *et al*., 1999). Several other analytical methods confirmed this range. Modeling of the Rio Blanco nuclear gas-stimulation site assumed a permeability of 2.96×10^{-15} m^2 (3 mD) for hydraulic fractures (Cooper *et al*., 2005).

To be consistent with the conceptual model, the permeability assigned to the hypothesized hydraulic fractures should be equal to or larger than that of the fracture permeability assigned to the native sandstones. To be consistent with the magnitude of the estimates presented above, the permeability selected for the east-west direction in the sandstone lenses is increased 100 times for the east-west direction of the hydraulic fractures. The mean permeability for the east-west hydraulic fractures in the calculated log normal distribution is 1.5×10^{-14} m^2 (15.2 mD). The permeability in the N-S direction is similarly calculated as a multiple of the native sandstone value, with a mean of 2.63×10^{-16} m^2 (0.27 mD). The intrinsic permeability of the hydraulic fracture zone follows the lognormal distribution, the same as that of the intrinsic permeability of the native sandstone.

4.5.2.2 Porosity, Saturation, Capillary Pressure, and Relative Permeability

Porosity of the nuclear chimney: The porosity in the chimney is expected to be considerably increased over that of the native Williams Fork Formation as a result of the creation of the cavity. Using geometric considerations, and assuming a cylinder with rounded ends, the void space of the cavity can be distributed throughout the chimney to estimate a porosity. Using a cavity radius of 23.5 m and chimney height of 83.8 m (the half-sphere void at the top must be subtracted for this calculation, giving a height of 60.4 m), the distributed porosity value is 0.34. This value is used for the porosity in the model cells representing the chimney.

Porosity of other rocks types: The most common pore geometry identified in Mesaverde sandstone samples from the MWX site is secondary solution pores connected by narrow intergranular slots (Soeder and Randolph, 1987). Porosity was found to primarily be a function of the solution pores, although permeability was controlled by flow through the narrow slots.

Porosity for producing wells completed in the Mesaverde Group in the Piceance Basin Continuous Gas Assessment Unit are reported to range from 0.07 to 0.12 (Johnson and Roberts, 2003). Cumella and Ostby (2003) report porosity of the productive Williams Fork sandstone as ranging from 0.06 to 0.12. Lorenz (1990) evaluated porosity of different sedimentary rock types in the lower fluvial interval at the MWX site and found that generally porosity was higher in the point-bar sand deposits and that it correlated to grain size. He reports an average reservoir porosity of about 0.08. Individual porosity values reported by Randolph (1983) for the fluvial interval at the MWX site range from 0.045 to 0.108. Over 290 core measurements of porosity for the fluvial interval are shown on data plots in Sandia and CER (1990). The mean of these data is 0.053, with a minimum of 0.011 and maximum of 0.11 (Figure 4-11). Analysis of geophysical logs from Hayward 25-95 led to an estimated average reservoir porosity of 0.078 in the fluvial sand, whereas core values suggested 0.087 (CER, 1969). Given the greater availability of data, the MWX core values are used here to establish a distribution of sandstone porosity.

Porosity for the intervening shale units is assigned as 0.07, as is the porosity at the boundaries of the model. With the focus on the sandstone reservoirs, most studies neglect measurements of the shale and claystone. With their very low permeability, the model is insensitive to the porosity assignment of these confining units. Low permeability, fine-grained units such as shale frequently have significant void space between mineral grains, though much of this can be expected to be lost due to compaction. Therefore, a value is selected that is within that measured for the adjoining fine-grained sandstone.

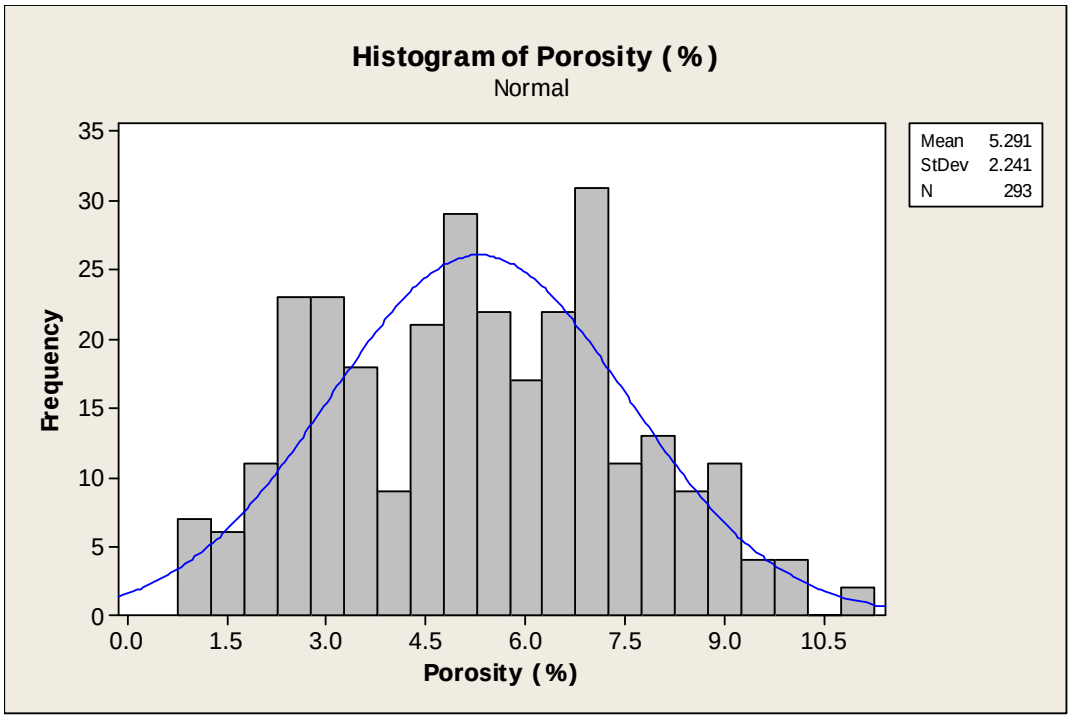

Figure 4-11. Histogram of core measurements of porosity (%) and a fitted normal distribution using MINITAB.

Fracture porosity is a very difficult parameter to measure. Though data are generally lacking, fracture porosity tends to be very low as compared to intergranular porosity. In the case of the equivalent porous medium Rulison model, the porosity assigned to the sandstone units (described above) represents the fractured sandstone reservoirs. The porosity of the hydraulically and nuclear stimulated fractured sandstone can be expected to be higher than the naturally fractured sandstone, particularly given the widespread use of propants (solid material, usually well-sorted sand, injected with the hydraulic fluid to hold the fracture open). Thus the porosity of the cells depicting hydraulically fractured sandstone, and representing explosion-related fractures adjacent to the nuclear cavity, is assigned a value of 0.10.

4.5.2.3 Saturation

Initial gas saturation was estimated as 0.50 in all rock types. This value is fairly certain for the sandstone and shale rocks, but less certain in the fractured formation (i.e., hydraulically fractured and nuclear-stimulated zones). All simulations were allowed to run to steady-state, so were ultimately controlled by the residual gas saturation, which was also set at 0.50.

4.5.2.4 Capillary Pressure

Capillary pressure as a function of liquid saturation was reported by Randolph (1983). The data are presented in Figure 4-12 along with the model used in the simulations. The data were collected using mercury as the working fluid; potentials (in mmHg) were multiplied by the density of mercury (13.55 g/ml) to convert to mm H_2O. The TRUST function (Pruess *et al.*, 1999, p. 188) was fit to the data. The TRUST function is a slight modification of the

more commonly known function developed by Brooks and Corey (1964). In the TRUST function, the capillary pressure is defined as

$$P_{cap} = -P_e - P_o\left[\frac{1-S_l}{S_l - S_{lr}}\right]^{1/\eta} \quad \text{for } S_{lr}<S_l<1 \tag{3}$$

$$P_{cap} = 0 \qquad \text{for } S_l = 1 \tag{4}$$

where P_o is a reference pressure (10^6 Pa), S_l is the (variable) liquid saturation, S_{lr} (= 0.50) is residual liquid saturation, η (=2) is a curve-fit parameter, P_e (=10^4 Pa) is an additional reference pressure that operates as a curve-fit parameter, and the saturations are all volumetrically based. The *in situ* saturations in the cores were measured at approximately 0.50; this was defined as the residual saturation. The reason is that for simulations without a water table (i.e., for these simulations) and a bottom boundary of prescribed pressure, the formation water drains to residual saturation. For that reason, it was assumed that the measured liquid saturation was at the residual value. The implication is that the liquid saturation is nearly everywhere 0.50 throughout the domain, as the rocks were assumed to be at steady-state prior to the start of the transport simulations. One significant point of maintaining a residual liquid saturation is that in the vicinity of the production well, liquid saturation was not allowed to drain below this value such that there was no liquid water produced with gas. In reality, some liquid water would be produced with gas, on the order of barrels per day, as this is what is observed in the Rulison field. The same capillary pressure function was used for all rock types.

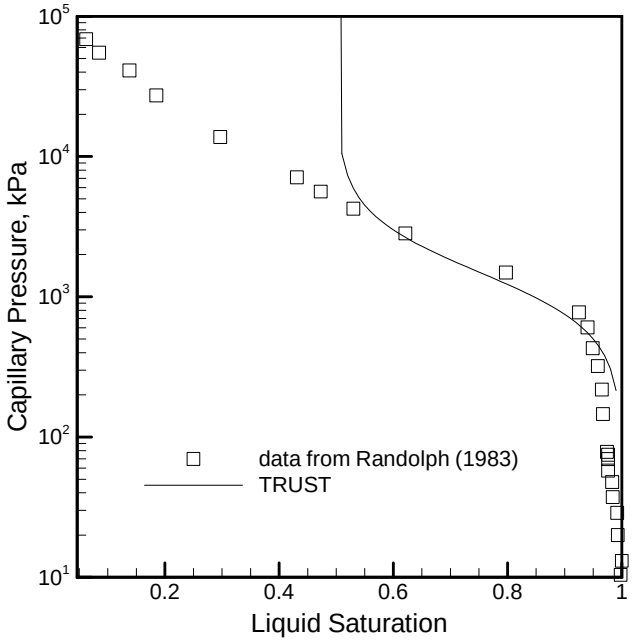

Figure 4-12. Moisture retention (i.e., capillary pressure) curve fit to data from Randolph (1983). The TRUST (Pruess *et al*., 1999) curve was fit to the data with S_{lr}= 0.5, P_e= 10^4, P_o = 10^6, and η = 2.

4.5.2.5 Relative Permeability

Corey's (1954) function was used to model relative permeability to gases and liquids (Figure 4-13). The relationship for relative permeability to liquid and gas, respectively, are

$$k_{rl} = \hat{S}^4 \tag{5}$$

$$k_{rg} = \left(1-\hat{S}\right)^2\left(1-\hat{S}^2\right) \tag{6}$$

where

$$\hat{S} = \frac{\left(S_l - S_{lr}\right)}{1 - S_{lr} - S_{gr}} \tag{7}$$

where k_{rl} is relative permeability to the aqueous phase, k_{rg} is relative permeability to the gas phase, and S_{gr} is residual gas saturation.

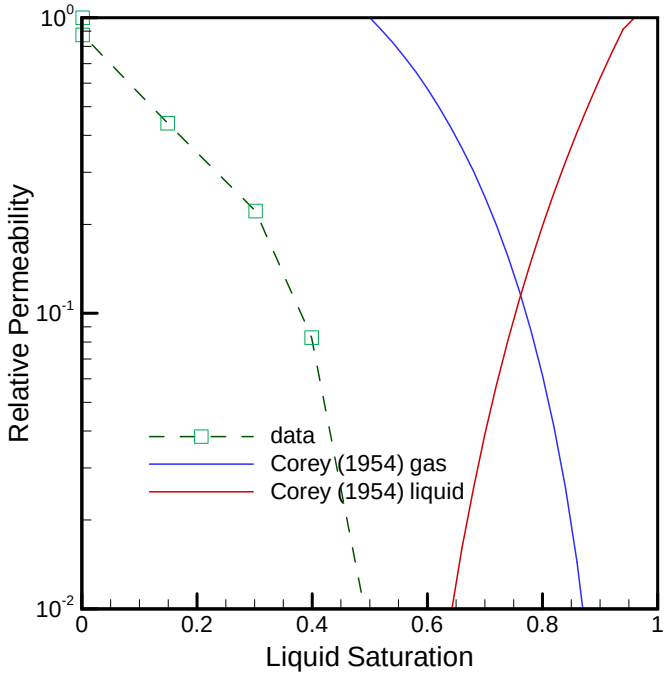

Figure 4-13. Relative permeability curves for gas and water. Data are from Randolph (1983), which were fit to Corey's (1954) function.

Randolph (1983) reported on measurements of permeability to gas as a function of liquid saturation; however, these measurements were all made for values of S_{lr} <0.5. In other words, liquid was "forced" out of the rocks such that the measurements were all made below residual saturation. An important feature of Corey's curves is that the relative permeabilities for each phase (k_{rl} and k_{rg}) do not necessarily sum to unity for any given saturation. This is important as extensive experimentation in the 1950s and 1960s indicated that $k_{r,g} + k_{r,l} \neq 1$ (Bear, 1988). The above functions (Equations [5] and [6]) were used for all rock types.

4.6 Transport Model Parameters

The transport model considers the migration of tritiated water, in liquid and vapor, through a two-phase system composed of methane gas and liquid water. Other gas-phase radionuclides, as well as tritiated hydrogen gas (^{3}H and ^{3}HH) and tritiated methane, were largely removed during gas-production activities shortly after the Rulison detonation, and are not included in the model.

4.6.1 Chemical Transport Properties

The following diffusion coefficients for gas mixtures are required: tritiated water (^{3}HHO or THO) and helium (the nonradioactive decay product of tritium) in methane. The free-air diffusion coefficient for helium has been measured and is reported in Cussler (1997). The free-air diffusion coefficient for tritiated water in methane was calculated using the method of Chapman and Cowling (see Reid *et al*., 1987). The effect of pressure on diffusivity (Reid *et al*., 1987, eq. 11-5.1) was investigated. For the reservoir conditions at Rulison (approximately 20 MPa), the diffusion coefficients changed only by 2 percent, well within the uncertainty of the estimates at low pressure. In the liquid phase, molecular diffusion coefficients were required for THO and He in water. Again, measured values of He at infinite dilution are provided in Cussler (1997) while tritiated water in liquid water was determined using the method of Wilke and Chang, which accounts for reservoir pressure (see Reid *et al*., 1987).

The product of the free-air (for gases) and molecular diffusion (for liquids) coefficients with a tortuosity value results in the effective diffusion coefficient through the reservoir rocks. As defined in TOUGH2, tortuosity can be defined as having a porous medium-dependent part, τ_o, and a saturation-dependent part, τ_β. The Millington-Quirk tortuosity model (Millington, 1959; Millington and Quirk, 1961), which incorporates phase-dependent saturation, was implemented in the simulations. That is

$$\tau_o \tau_\beta = \phi^{1/3} S_\beta^{\,10/3} \tag{8}$$

where ϕ is porosity, and S_β is the phase saturation. Figure 4-14 shows the tortuosity as a function of various porosities. Millington-Quirk is one of the most common tortuosity models for solute transport in porous media. Tortuosity was found to be a source of uncertainty in the Rio Blanco model (Cooper *et al*., 2005), when compared to a proposed relative permeability-based model. A model based upon relative permeability, instead of phase saturation, was found to enhance the mass fraction of tritiated water in the gas phase by tens of meters in both the longitudinal and transverse directions. With respect to fractured rock, however, there are no tested tortuosity models. The understanding of tortuosity in fractured rock is incomplete, partly due to the inability to adequately characterize natural fractures and fracture networks. As stated in the section on the Conceptual Model, mechanical dispersion in the liquid phase was not included.

Values for Henry's constant of methane dissolution in water vary between 4.41×10^{-10} Pa^{-1} (0ºC) to 1.41×10^{-10} Pa^{-1} (100ºC) (Perry and Green, 1997). Since the values change by only a factor of three, and because the geothermal gradient relates to a temperature of approximately 100ºC throughout much of the reservoir, the default value for air dissolution in water was used (10^{-10} Pa^{-1}). This is not expected to have a significant effect on the results, as methane dissolution in water is small.

Finally, the half lives of ^{3}H and ^{85}Kr are 12.32 and 10.76 yr, respectively (Parrington *et al*., 1996).

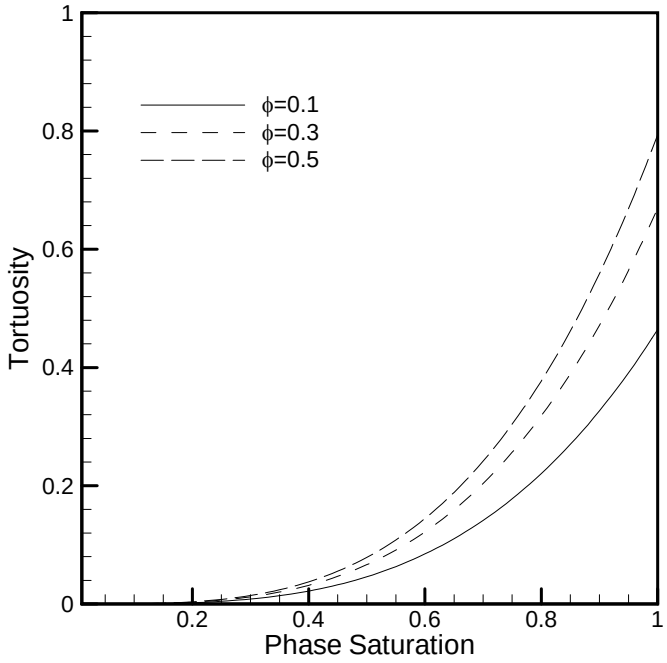

Figure 4-14. Tortuosity model showing dependence on porosity.

4.6.2 Radioactive Source Values

The production of radionuclides by the Rulison device was predicted based on nuclear device design and evaluated based on observed radionuclide concentrations during reentry and testing operations. The initial tritium production has been reported as 10,000 Ci (AEC, 1973b). Bowen *et al.* (2001) state that accuracy of tritium estimates for underground nuclear tests is 300 percent or better, with the larger error associated with nuclear tests in which no data were collected after the test. For nuclear tests in which data were collected after the test, such as Rulison, the estimates are more accurate. This level of uncertainty is small relative to other sources of uncertainty in the flow and transport problem.

Following the nuclear detonation, there was a hiatus in operations to allow decay of short-lived radionuclides, and to resolve legal matters regarding the proposed production testing. In 1970, the exploratory well, Hayward 25-95 R-EX was reentered and directionally drilled to intercept the Rulison chimney. Four episodes of production testing occurred, each of which removed radionuclides along with the gas. Radionuclide concentrations in the flared (burned in the atmosphere) gas were monitored (AEC, 1972a). Based on these data, 2,824 Ci of tritium were removed from the subsurface, either within the dry gas, or as water and hydrocarbons. This amount can be decay-corrected to the time of the detonation to calculate

the amount removed relative to the original 10,000 Ci (Table 4-2). The decay-corrected tritium mass removed is 3,059 Ci.

The amount remaining in the subsurface after the flaring is 6,941 Ci. This is the mass of tritium available for migration through the subsurface, decay-corrected to zero time.

Table 4-2. Tritium associated with the Rulison test. All values are in Curies. Decay-correction is based on a tritium half-life of 12.32 years, with correction to September 10, 1969.

^{3}H Produced: 10,000
^{3}H Removed: 3,059

	^{3}H in dry gas	^{3}H in water and hydrocarbons	Total at time flared	Total flared, decay-corrected to zero time
Calibration flaring	60	4	64	68
High-rate flaring	418	201	619	660
Intermediate-rate flaring	385	265	650	698
Long-term flaring	290	1,201	1,491	1,633
Total			2,824	3,059

^{3}H remaining, decay-corrected to zero time: 6,941

As reported by Smith (1975), following a nuclear detonation, the distribution of tritium between the liquid and gas phases is not at equilibrium, but it is unknown how long this disequilibrium may persist. It is known, however, that for geothermal (i.e., high-temperature) systems considered at equilibrium, partitioning of tritiated water occurs such that a sample from the liquid phase has nearly the same radioactivity as an equivalent volume of condensate from the gas phase (Pruess, 2002). The difference in mass fractions between water vapor and liquid water is due solely to isotopic fractionation. Mass fraction (X) is defined as the mass of a component within a phase divided by the total mass of that phase, for a unit volume. That is

$$X_{gas}^{\ THO} = \frac{m_{gas}^{\ THO}}{\sum m_{gas}^{\ i}} = \frac{m_{gas}^{\ THO}}{m_{gas}^{\ THO} + m_{gas}^{\ H_2O} + m_{gas}^{\ CH_4}} \tag{9}$$

where m refers to mass, the subscripts depict the phase, and the superscripts depict components in that phase. The fractionation factor for tritium at 100ºC is 1.030 (Ferronsky and Polyakov, 1982, Table 1.4). This means that the liquid phase is enriched in tritiated water by only 30 per mil, or 3 percent. At equilibrium, therefore, mass fractions of tritiated water in water vapor and liquid water are so close that they can be considered to be equivalent, as the model considers mass fraction values spanning more than nine orders of magnitude. This is not the same as the mass fractions in the two phases—gas and liquid—being equivalent, since the gas phase contains mostly methane and some water vapor.

At Rulison, tritium is transported in the reservoir as tritiated water, and is therefore partitioned thermodynamically in the same manner that water is partitioned between the aqueous and gas phases. In TOUGH2, this partitioning is based upon the steam table and Kelvin equations (Pruess *et al*., 1999). However, only a small fraction of the water is tritiated, and needs to be treated as a tracer, separate from the bulk of nontritiated water in each phase.

For tritium partitioning between the liquid and gas phases to be modeled correctly, tritiated water is treated as a tracer in this problem, implementing Henry's law in an *ad hoc* manner for partitioning. It is important to note that this was done simply to partition tritiated water between the gas and liquid phases. Central to this approach is the assumption of equilibrium between liquid and vapor phases. This in turn requires contact between water vapor in the gas-filled fractures and liquid water in the partially saturated pore spaces, or in films on fracture surfaces, a contact facilitated by the high water content of the Williams Fork formation (in excess of 0.5). It also demands rapid equilibration, particularly during the gas production scenarios. The assumption of rapid exchange is supported by experiments measuring tritium exchange between liquid and vapor that found equilibration times on the order of seconds (Slattery, 1993).

The following explains how the partitioning was approximated using the Henry's law coefficient. For example, for an X_l^{THO} of 10^{-7} kg THO per kg liquid, the equivalent value in the gas phase should be 10^{-7} kg THO per kg condensed water. This would, however, need to be converted to concentration in the gas (methane plus water vapor) phase. That is,

$$X_g^{THO} = \left(\frac{m_{THO}}{m_{\text{water vapor}}} \right) \left(\rho_{\text{sat vapor}} \right) \left(\frac{1}{\rho_{\text{total gas phase at sat}}} \right) \tag{10}$$

where m refers to mass and ρ is mass density. If the mass fraction of tritiated water in the aqueous phase is 10^{-7} kg m^{-3} tritiated water per kg m^{-3} liquid (considered dimensionless throughout the rest of this discussion), then the mass of tritiated water per mass of water vapor is also 10^{-7}. To determine the correct partitioning relative to the total gas phase (methane plus water vapor), the mass fraction X_g^{THO} was calculated based upon the above equation and using 10^{-7} as $m_{\text{THO}}/m_{\text{water vapor}}$. This value of X_g^{THO} was then used as a target to determine what Henry's law coefficient results in the same value. By doing this, it was determined that a Henry's law coefficient of 9.65 x 10^{-8} Pa^{-1} results in correct partitioning of tritiated water mass between the two phases. This implementation assumes a constant temperature and gas density. The gas densities varied spatially by approximately 15 percent in the simulations.

It must be emphasized that being part of the water molecule, tritiated water does not partition between the gas and liquid phases in accordance with Henry's law. The Henry's law equation is used here only as a method to partition, because it can be manipulated to calculate the correct partitioning. An approach using Henry's law would, however, be appropriate for noncondensable diatomic tritium (i.e., $^2H^3H$, or $^3H_2$), which is volatile.

The above discussion describes how tritiated water is distributed between the gas and aqueous phases. The initial mass fraction of tritium must also be addressed. TOUGH2 requires that the initial mass fraction of "solute" (tritiated water, in this case) be input as mass fraction in the liquid phase -- there is no consideration for initial mass fraction in the gas phase. Partitioning between phases is done during the first time step. This is usually not a problem, as most users know the aqueous phase mass fraction of the solute they are modeling. At Rulison, however, it is only known that the initial radioactivity of tritiated water was 6941 Ci; it is not known how this radioactivity was distributed initially between

phases. The following describes how the initial mass fraction of tritiated water in the aqueous phase was determined.

Mass of tritiated water is calculated from radioactivity (Curies) from the following expression (where dps is "disintegrations per second"):

$$1\,\text{Ci } {}^3\text{H}\left(\frac{3.7\text{x}10^{10}\,\text{dps}}{1\,\text{Ci } {}^3\text{H}}\right)\left(\frac{\text{atom } {}^3\text{H}}{1.78\text{x}10^{-9}\,\text{dps}}\right)\left(\frac{1\,\text{mol } {}^3\text{H}}{6.02\text{x}10^{23}\,\text{atoms } {}^3\text{H}}\right)\left(\frac{0.003\,\text{kg } {}^3\text{H}}{1\,\text{mol } {}^3\text{H}}\right)\left(\frac{0.020\,\text{kg THO}}{0.003\,\text{kg } {}^3\text{H}}\right)$$
$$= 6.906 \text{ x } 10^{-7} \text{ kg THO} \qquad (11)$$

A Curie is defined as 3.7 x 10^{10} dps, while the decay constant for tritium (1.78 x 10^{-9} dps) is defined as $\ln 2/t_{1/2}$, where $t_{1/2}$ is the half-life of tritium (in seconds).

The mass is partitioned between phases in the following manner. If C is denoted as the total mass of tritium, and A and B are tritium mass in the aqueous and gas phases, respectively, then $A+B=C$. A is calculated using the mass fraction X_l^{THO} specified in the initial conditions and water mass in the element (grid block) based on element volume V_{ele}, porosity ϕ_{ele}, and liquid saturation S_l, i.e., $A = \rho_l V_{ele}\phi_{ele}S_l X_l^{THO}$. B is calculated using Henry's law and the ideal gas law. The pressure corresponding to mass fraction X_l^{THO} is first calculated using Henry's law $P = K_h X_l^{THO}$, where P is the partial pressure and K_h is Henry's constant. The number of moles of tritiated water vapor is then calculated using the ideal gas law $n = \frac{PV}{RT} = \frac{K_h X_l^{THO} V_{ele}\phi_{ele}S_g}{RT}$, where $S_g = 1 - S_l$ is the gas saturation. Therefore, the mass of tritium in gas phase is $B = \frac{K_h X_l^{THO} V_{ele}\phi_{ele}S_g}{RT} \times 20$, where 20 is molecular weight of tritiated water. Since $A+B=C$,

$$\rho_l V_{ele}\phi_{ele}S_l X_l^{THO} + \frac{K_h X_l^{THO} V_{ele}\phi_{ele}S_g}{RT} \times 20 = X_l^{THO}\left(\rho_l V_{ele}\phi_{ele}S_l + \frac{K_h V_{ele}\phi_{ele}S_g}{RT} \times 20\right) = C \qquad (12)$$

and X_l^{THO} is estimated as

$$X_l^{THO} = C \Big/ \left(\rho_l V_{ele}\phi_{ele}S_l + \frac{K_h V_{ele}\phi_{ele}S_g}{RT} \times 20\right) \qquad (13)$$

The chimney was composed of 88 grid blocks, each with the dimensions 20 m x 20 m x 5 m high (2,000 m^3 volume). The porosity and liquid saturations were assumed 0.34 and 0.5, respectively. The source was distributed evenly among all 88 grid blocks.

4.7 Transient Parameters

4.7.1 Gas Well Production Characteristics

The gas production well is located 258 m from the nuclear emplacement well, Hayward 25-95A. The distance from Hayward 25-95A due west to the lot 11-lot 12 boundary is approximately 185 m. By Colorado Oil and Gas Conservation Commission Order No. 139-43, wells cannot be located closer than 73 m from the boundaries of the drilling and spacing unit. The hypothetical production well is thus placed 73 m west of the lot 11-lot 12 boundary, resulting in a distance of 258 m between the hypothetical well and Hayward 25-95A.

A production decline curve provided by Presco, Inc. (Houston) was used in the simulations (Table 4-3). The curve was based upon producing histories in gas fields in the vicinity of the Rulison nuclear test, where gas was produced from the Williams Fork Formation. Each production well within a field was different, although gas was typically produced from 10 to 15 perforated intervals with typical lengths of 6.1 m. In this model, it is assumed that production occurs from a 5-m zone (consistent with the vertical grid discretization), which produces 10 percent of the rate provided by Presco, Inc. It is assumed that production begins in 2007, i.e., 38 years after the nuclear detonation. That is, radionuclides are transported under "natural" processes -- such as advection, dispersion, and diffusion -- from 1969 until 2007, at which time production begins. Gas production is assumed to take place for 30 years; after this time, production is turned off and radionuclide transport occurs in the presence of the recovering pressure field.

Table 4-3. Gas decline curve for simulations with gas production. Values are in thousands of cubic feet of gas (MCFG) for the entire month.

	Jan	Feb	Mar	Apr	May	Jun	Jul	Aug	Sep	Oct	Nov	Dec
1992	39,000	35,400	31,350	24,000	21,000	18,600	16,500	15,900	15,000	14,400	14,100	13,950
1993	11,550	11,550	11,550	10,800	10,800	10,800	10,260	10,260	10,260	9,750	9,750	9,750
1994	9,000	9,000	9,000	8,250	8,250	8,250	7,860	7,860	7,860	7,500	7,500	7,500
1995	7,050	7,050	7,050	6,600	6,600	6,600	6,450	6,450	6,450	6,300	6,300	6,300
1996	6,150	6,150	6,150	6,000	6,000	6,000	5,850	5,850	5,850	5,700	5,700	5,700
1997	5,550	5,550	5,550	5,400	5,400	5,400	5,250	5,250	5,250	5,100	5,100	5,100
1998	4,950	4,950	4,950	4,800	4,800	4,800	4,710	4,710	4,710	4,650	4,650	4,650
1999	4,560	4,560	4,560	4,500	4,500	4,500	4,380	4,380	4,380	4,260	4,260	4,260
2000	4,140	4,140	4,140	4,050	4,050	4,050	3,900	3,900	3,900	3,810	3,810	3,810
2001	3,690	3,690	3,690	3,600	3,600	3,600	3,450	3,450	3,450	3,300	3,300	3,300

4.7.2 Hydraulic Fracture Zone Geometry

Despite great interest in the size of fractures generated by hydrofrac operations, data regarding fracture geometry are sparse due to the difficulty of making observations. Most estimates are the result of interpretation of microseismic signals. Warpinski *et al*. (1997) used a variety of data, including intersecting wells, to demonstrate that microseismic activity can provide a reliable image of a hydraulic fracture. The ideal hydraulic fracture is usually considered a single feature spreading from the stimulated well (a "bi-wing" fracture). Mahrer

(1999) found that actual hydraulic fractures are often more complex than this ideal. Multiple fractures result in shorter, narrower, and less conductive fractures than expected from a single planar feature (Mahrer, 1999).

4.7.2.1 Hydraulic Fracture Length

The presence of fracturing, as indicated by microseismic events, does not necessarily correlate to conductive, connected flow pathways. Phillips *et al*. (2002) emphasize that although the presence of seismicity is taken to indicate a pressure connection, it is not necessarily a high-permeability connection between that point and an injection well. They note that some of the most conductive flowpaths are likely to be in seismically inactive regions. A study specific to propant placement (Sharma *et al*., 2003) found that propped or effective fracture lengths derived from pressure buildup analysis and history matching production data were significantly shorter than the designed or predicted fracture lengths. Using data from six wells in Texas, they found propped fracture lengths of 76.2 m from pressure buildup and production response data, whereas microseismic data indicated created fracture lengths of 122 to 152 m, and fracture models predicted lengths of 305 to 366 m. They also note that their propped lengths are longer than those usually achieved by standard fracturing methods, which typically show effective fracture lengths of 30.5 to 45.7 m (Sharma *et al*., 2003).

Another study in Texas used high-resolution microseismic techniques to analyze hydraulic fractures in tight gas-sands (Rutledge and Phillips, 2003). The majority of seismic events occur within 198 m of the injection well, though a shallower zone of seismicity indicated fractures out to 396 m. Rutledge and Phillips conclude that pressurizing existing fractures may be the primary process of enhancing permeability and fracture network conductivity over most of the length attained, rather than creating new hydraulic fractures. They also identify a trailing aseismic zone, which they suggest may be related to the fracture length that is maintained open and thus available for propant placement. The aseismic zone attained lengths of about one-third to one-half of total seismic length, suggesting potentially conductive hydrofrac lengths of 61 to 198 m. Long seismic lengths (over 760 m) were also identified for an injection in the Austin Chalk (Phillips *et al*., 2002), though again, a lack of conductivity was observed based on production performance. Work in other environments has found much shorter lengths. Based on interpretation of well tests in seven production wells completed in tight sands in the Green River Basin, Reeves *et al*. (1999) determined hydrofrac lengths of 15 to 50 m.

Research at the MWX site provides hydraulic fracturing data close to the Rulison test site. The MWX included reservoir stimulation experiments (Sandia and CER, 1990). During stimulation of the Fluvial B-sand, microseismic data recorded events at distances up to 39.6 m on the east wing and 45.7 m on the west wing of the hydrofrac. Operational data suggested a propped fracture length of 97 m. Seismic data from the suite of fracturing operations in the C-sand identify asymmetric fracture wings of 76.2 m to the west and at most 61 m to the east (azimuth of 63 west of north). The purpose of the stimulation experiment in the E-sand was to create a propped hydraulic fracture with a 229-m length, though this was not achieved. Microseismic data defined a symmetric hydraulic fracture with wing lengths of 76.2 m, though elsewhere, operational data are cited as indicating a propped fracture length of 122 m. In the coastal zone, below the fluvial interval, hydrofracs were 76.2 to 91.4 m in length in one stimulation (Sandia and CER, 1989). Another stimulation in

that zone estimated a total hydrofrac length of 90 m and propped length of 84 m from a treatment pressure history match, but subsequent well tests indicate an effective fracture length of less than 46 m.

More recently, the MWX site (renamed the "M-Site") was the location for additional research pertaining to hydraulically fractured rocks. Warpinski *et al*. (1996) evaluated six hydrofrac operations in the B-sand fluvial sandstone (Williams Fork) at the MWX site, identifying a range in length from 53.3 to 106.7 m and a range in height of 12.2 to 41.1 m. They note that the length changes only slightly from tests of small-volume, low-viscosity fluids pumped at slow rates to larger volumes of high-viscosity fluids pumped at high rates, with the height being more affected. Another six hydrofrac operations were performed in the C-sand, resulting in fractures extending 121.9 to 152.4 m. However, diagnostics at an intersection well located at a distance of 87.5 m showed that the fractures were not conductive connections. One of their stimulations was a propped treatment of a size typically performed per interval in the basin. Most of the fractures from that injection were within 121.9 m of the injection well.

A commercial operator in the Rulison area reports hydrofrac lengths of 83.8 to 106.7 m (Presco, personal comm., 2004).

In regard to the width of the hydraulic fracture, Mahrer (1999) noted the characteristic of microseismic data to map an elongated, nonplanar, three-dimensional fracture cloud. He associates this with the width of the fracture zone, finding it to be five or more percent of the length.

From the information presented above, it is likely that hydrofrac operations in the foreseeable future near the Rulison test site could create conductive pathways extending 45.7 to 121.9 m from a stimulated well. Though longer fractures cannot be ruled out, they are unlikely to remain open, conductive conduits for fluid flow. However, a hydraulic fracture length of 160 m could connect directly with the fracture zone simulated around the nuclear chimney and thus represents an important scenario to include in the uncertainty analysis. The possibility of even longer fractures is included by assuming a lognormal distribution for hydraulic fracture length. Lognormal distributions are typical of fracture length and height (Lorenz, 2003). Given the model discretization of 20 m in the *x-y* directions, 95 percent of the lognormal distribution will occur between 40 m and 160 m, with a mean length of about 85 m.

4.7.2.2 Vertical Extent of Hydraulic Fractures

Hydraulic fracture operations are generally designed to stay "in-zone," that is, confining the hydraulic fractures to the desired stratigraphic interval. In practice, this appears to often work well in sedimentary environments. Phillips *et al*. (2002) observed a strong tendency for microseismicity induced by fluid injection to organize into thin, roughly horizontal strands of activity in clastic sedimentary environments. The near-horizontal orientations led them to suspect that stratigraphy controls fracture behavior, with stratigraphic changes limiting fracture growth through an increase in ductility or an increase or decrease in mechanical strength and supported stress at a layer boundary. Rutledge and Phillips (2003) found that propped hydraulic fracture height was reasonably well contained to the perforated depth interval during injections in the Cotton Valley Formation, a gas reservoir in low-permeability sands interbedded with shales. They believe the containment of

seismicity within the target sands occurs due to activation of the reservoir's prevalent natural fractures, which are confined within individual sands and largely absent in the intervening shales. The depth distribution of microearthquakes presented by Rutledge and Phillips (2003) is generally contained in intervals with heights of less than 10 m around approximately 5-m perforation zones. Closer to the Rulison site, a series of six hydrofracture operations in the 15-m-thick B-Sand of the lower fluvial interval of the Williams Fork at the MWX site produced a range of fracture heights from 12 to 41 m, with an average of 22.4 m. Warpinski *et al*. (1997) similarly found that hydrofractures were generally contained within the C-sand during injections in that unit.

For the gas-production scenario, it is assumed that the perforation interval extends 5 m vertically. This is consistent with industry practice and with the general thickness of sand bodies encountered in the Hayward 25-95 and 25-95A wells (average thickness of 6.7 m, but recall the vertical grid discretization is 5 m). The location of the production interval is different in each realization, depending on the spatial distribution of the sandstone and shale facies. The location of the production well is attempted to be first placed at the same elevation as the nuclear working point; if that cell contains sandstone in a given realization, and there is another sandstone facies above or below the cell the well is then placed there. This is to ensure that the hypothetical production occurs in a sandstone lens that is at least 10 m thick. Otherwise, if the initial location is in shale or there is only one grid block of sandstone, a search strategy starts. A grid block above the initial grid block is first searched. If the requirements of a sandstone lens of at least 10 m thick is satisfied, the production well is place in the grid block. Otherwise, a grid block below the initial location is searched. This up-and-down cyclical searching strategy continues until the requirements are satisfied. The hydraulic fracture zone simulated around the perforation interval is assumed to have a vertical extent of 10 m above the perforation and 10-m below the perforation. This yields a zone of 25 m that is assigned hydraulic fracture properties extending out into the formation from the assumed production well location. This assignment considers the hydraulic fracture information described above, while balancing the desire to intercept sand bodies that are simulated in the equiprobable realizations with the possible diluting effect of an overly thick production interval. Within the 25 m zone, sandstone is perforated, while shale remains shale.

In practice, a production well would have many perforated intervals. These producing horizons above and below the simulated zone are considered to have little to no impact on the fluid flow considered here. This result is expected due to the natural layering of the lower Williams Fork Formation, with the intervening shale barriers, and due to the no-flow boundaries that would result between stacked producing intervals. Placing the producing interval at the same (or nearly same) interval as the radionuclide source ensures that the shortest possible flowpath is considered in the analysis.

4.8 Implementation of Numerical Model

Significant uncertainty exists in the hydraulic parameters and geometry of hydrogeologic facies, due to their spatial variability and limited measurements within the modeling domain. Thus some aspects are treated as random variables to account for the uncertainty. The generation of conditional random realizations of the hydrogeologic facies was described previously. A summary of the computational sequence is presented first. This is followed by a description of the development of the probability distributions of the random

parameters applied in the domain. Finally, there is a description of the random field generation.

4.8.1 Computational Sequence

Solution of the flow and transport equations for the Rulison problem involves a complex sequence of modeling steps using the programs T-PROGS and TOUGH2 to generate input files. Figure 4-15 distills this sequence to a series of inputs, actions, and computations and gives an overview of the modeling process The final results are comprised of 500 equiprobable realizations. Each individual realization, or model run, begins with random selection of one of the constructs of the geologic model generated using the T-PROGS computer program. The T-PROGS realization assigns the model cells to sandstone or shale facies according to the spatial statistics describing the fluvial sequence, and conditioned using the known lithology at wells Hayward 25-95 and 25-95A. Along with the T-PROGS realization, values for sand porosity and sand matrix permeability (permeability in the north-south *y*-direction, and in the vertical *z*-direction) are selected from their respective data distributions. A multiplier value is selected from a uniform distribution and combined with the selected matrix permeability to compute a fracture permeability for the sand in the east-west *x*-direction. The steady-state flow problem is then solved in TOUGH2, using the selected uncertain parameters, along with all the deterministic parameters. At this point, the flow model simulates one realization of gas and liquid flow conditions at the Rulison site, prior to the nuclear test.

Once steady-state flow conditions are achieved, the input file is altered by adding the effects of the nuclear test. This involves increasing the permeability and porosity of the grid blocks occupied by the cavity and chimney. Cells immediately surrounding the chimney are also changed by altering their permeability to simulate adjacent fractures generated by the test. The tritium source is added to the chimney region and the TOUGH2 simulation begins again, simulating migration for the 38 years from the test detonation until present day. The flow model to this point has now simulated one realization of tritium migration to year 2007, which is essentially migration due to diffusion because no gas production has occurred within the model domain.

At this point, the simulation assumes a production well is located due west of Hayward 25-95A, in Lot 12. A production interval is identified for the well in the sand interval closest to the center elevation of the nuclear chimney. This interval is assumed to undergo a hydrofrac operation. A length for the hydrofrac zone is selected from a distribution. The hydraulic conductivity of the hydrofracs is computed from the k_y=k_z previously selected and the k_x previously calculated, by multiplying those values by 100 to generate anisotropic permeability values for the hydrofracs. The selected hydrofrac characteristics are combined with deterministic production conditions and TOUGH2 resumes calculations. Flow and transport are computed for 500 years into the future, a time-period which includes 30 years of gas production from the hypothetical well (from year 38 to year 68 of the simulation or between the years 2007 and 2037). The above sequence is then repeated until 500 of the geologic model realizations have been used.

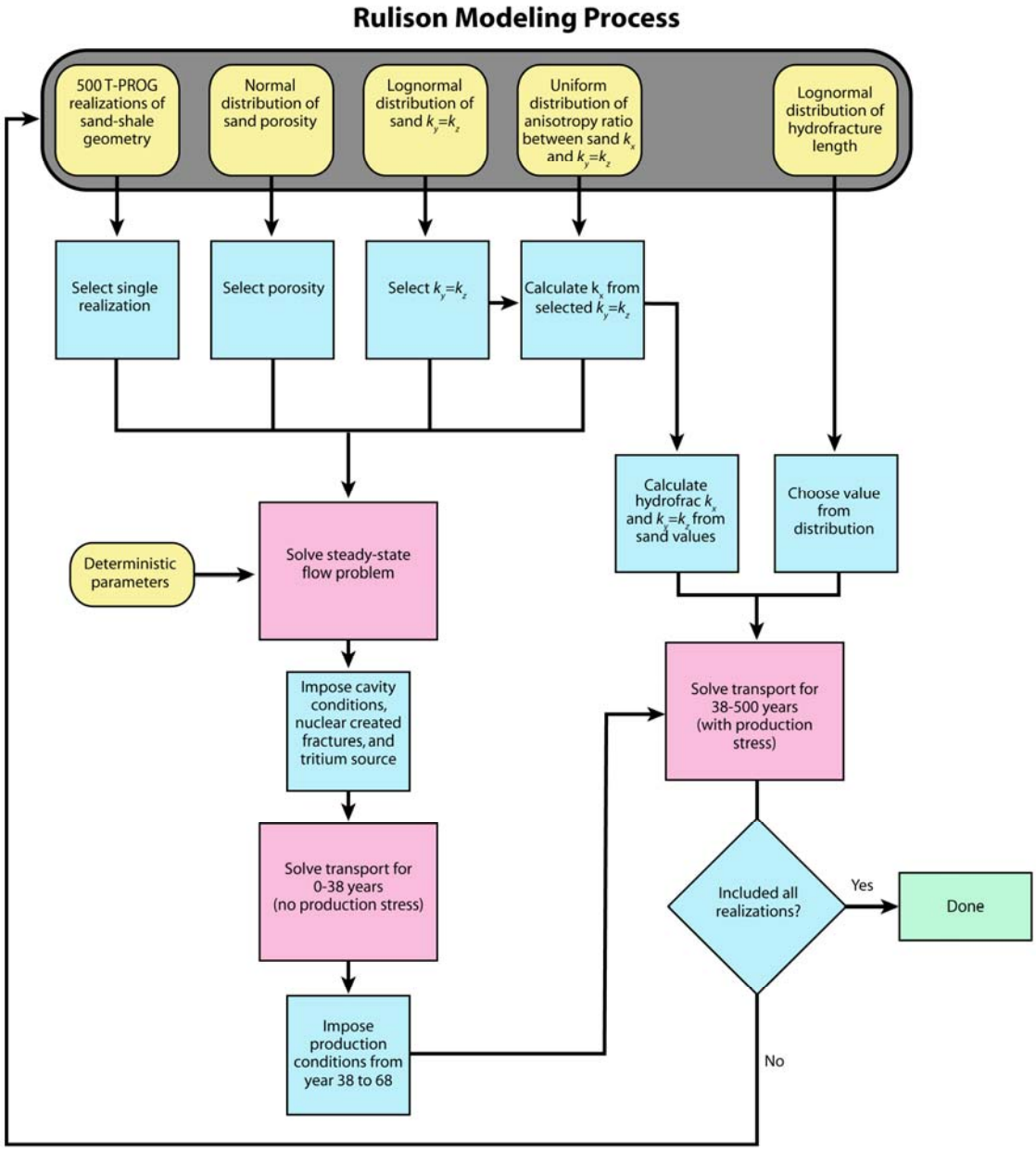

Figure 4-15. Simplified schematic of the modeling process followed for the Rulison simulations. Yellow boxes denote model input, blue boxes describe actions, and pink boxes show model runs.

4.8.2 Identification of Distributions of Random Variables

Hydraulic parameters vary within each facies at the site, and the spatial variation is uncertain due to limited measurements. Since flow and transport in the conceptual model is restricted to the sandstone facies, only hydraulic parameters in the sandstone facies are considered random to address their uncertainty (i.e., parameters for the shale facies are treated deterministically). The following parameters were considered random variables in the simulation: intrinsic permeability and porosity of the sandstone, and length and intrinsic

permeability of the hydrofracs. The distributions of these random variables were first developed, and then 500 realizations of these variables were generated using the Latin Hypercube Sampling (LHS) method.

Permeability distributions (measured at 3,000 psi) were identified based on 140 core measurements at the MWX site (Sandia and CER, 1990). Porosity distributions were identified from 293 core measurements, whose values were digitized from data plots shown in Sandia and CER (1990). While 307 data are digitized, 14 data were considered as outliers and discarded from the analysis. Descriptive statistics of the measurements are listed in Table 4-4. Sandstone permeability varies from 1.97×10^{-20} m^2 (0.02 μD) to 3.47×10^{-17} m^2 (35.13 μD), indicating a significant variability. The range of porosity is small, within approximately one order of magnitude.

Table 4-4. Descriptive statistics of sandstone permeability (presented in μD and m^2) and porosity (%) measurements from core analysis.

Parameter	N	Mean	Standard Deviation	Min	Q25	Median	Q75	Max
Permeability (μD)	140	2.308	3.708	0.020	0.345	0.910	3.388	35.130
Permeability (m^2)	140	2.28×10^{-18}	3.66×10^{-18}	1.97×10^{-20}	3.41×10^{-19}	8.98×10^{-19}	3.34×10^{-18}	3.47×10^{-17}
Porosity (%)	293	5.29	2.24	1.05	3.50	5.22	7.10	10.9

Following Carsel and Parrish (1988), three distribution types of transformations (Johnson, 1987) were first applied to the measurements. They are the lognormal (LN), log ratio (SB), and hyperbolic arcsine (SU)

$$\text{LN: } Y = \ln(X) \tag{14}$$

$$\text{SB: } Y = \ln[(X - A)/(B - X)] \tag{15}$$

$$\text{SU: } Y = \sinh^{-1}(U) = \ln(U + \sqrt{1 + U^2}) \tag{16}$$

where X is the untransformed variable with limits of variation from A to B ($A < X <$B) and $U = (X\text{-}A)/(B\text{-}X)$. Denoting the original data as NO (meaning no transformation) yields four data sets: NO, LN, SB, and SU. The Lilliefors test for normality, which is a variant of the Kolmogorov-Smirnov test, was used to test goodness-of-fit of a set of the transformed data to a normal distribution with mean and variance estimated from the data set (this is not specified *a priori* as in the Kolmogorov-Smirnov test). The steps of the Lilliefors test are as follows:

(1) Normalize a data set with mean and standard deviation estimated from the data

$$z_i = \frac{x_i - \bar{x}}{s} \quad (i = 1, 2, ..., N) \tag{17}$$

where z_i and x_i are normalized and original data, respectively; $\bar{x}$ and s are sample mean and standard deviation of X, respectively; and N is the number of the data, which must be at least 4.

(2) Calculate the empirical cumulative distribution function (CDF), $G(z)$, and the standard normal CDF, $F^*(z)$;

(3) Evaluate the maximum absolute difference (T^*) of $F^*(z)$ and $G(z)$

$$T^* = \max\left|F^*(z_i) - G(z_i)\right| \quad i = 1,2,...n \tag{18}$$

(4) Select a level of significance α to obtain the Lilliefors test statistic T from Bowen and Bennett (1988). If T^* exceeds T, the hypothesis of normality is rejected at the significance level of α.

The four transformations of NO, LN, SB, and SU are applied to the measurements of permeability and porosity. Empirical CDFs of the transformed permeability data are plotted in Figure 4-16. For the sake of comparison, the figure also plots theoretical CDFs of the normal distribution with mean and variance obtained from the transformed permeability data. Figure 4-17 does the same for porosity. Visually, the LN and NO transforms are the best for permeability and porosity, respectively, indicating that the lognormal and normal distributions best describe the intrinsic permeability and porosity data, respectively.

Quantitative evaluation of the best distribution is conducted using the Lilliefors test. The maximum differences, T^*, corresponding to the four transformations are listed in Table 4-5, which also lists the Lilliefors T value of 0.05 significance levels obtained from Bowen and Bennett (1988). The T^* of LN and NO is the smallest for permeability and porosity, indicating that the CDFs of the two transformations are the closest to the targeted normal distribution. However, comparing the T^* values of the two transformations and their corresponding T values shows that the LN- and NO-transformed data failed to pass the Lilliefors test at the significance level $\alpha = 0.05$. This may be due to the large size of available measurements, since T is estimated as $0.886/\sqrt{n}$ (n being the number of measurements) (Bowen and Bennett, 1988). Nevertheless, Figures 4-16 and 4-17 suggest that it is reasonable to use lognormal and normal distributions to describe the permeability and porosity data.

As discussed before, the anisotropy ratio between permeability at the x and y (and z) directions is also uncertain, due to lack of measurements. The ratio is treated as a random variable to account for the uncertainty. Plausible minimum and maximum values of the ratio are 10 and 100, respectively (Lorenz, 2003). Since there is no other information available about the ratio, a uniform distribution, U(10,100), is used to describe the distribution.

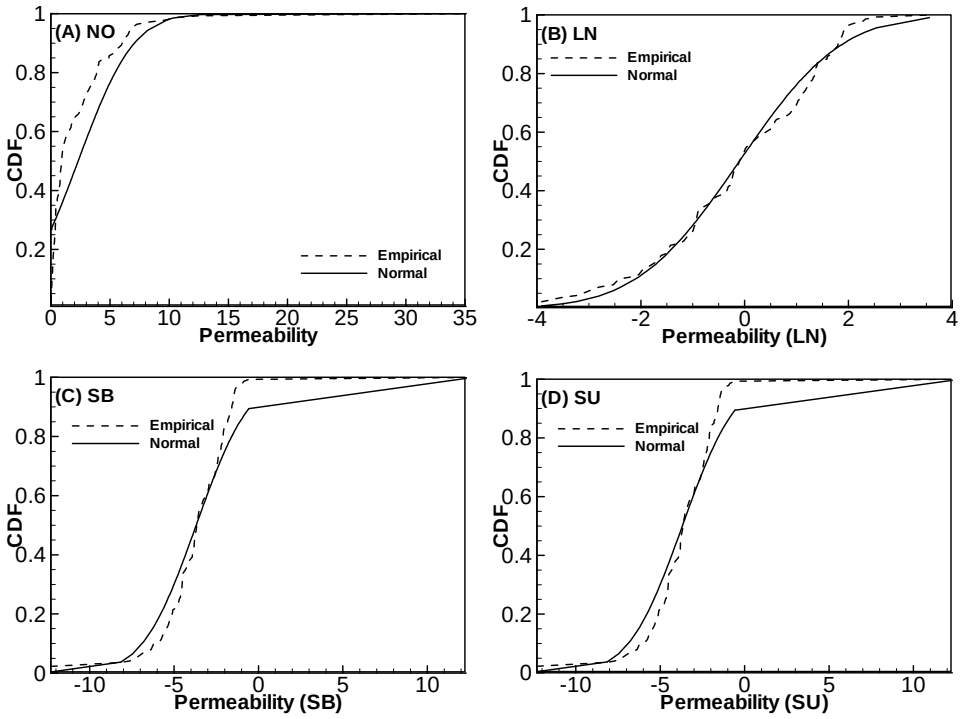

Figure 4-16. Empirical and theoretical cumulative distribution function (CDF) of (a) permeability data and its (b) LN, (c) SB, and (d) SU transforms. Permeability is in microdarcy; one microdarcy is 9.87 x 10^{-19} m^2.

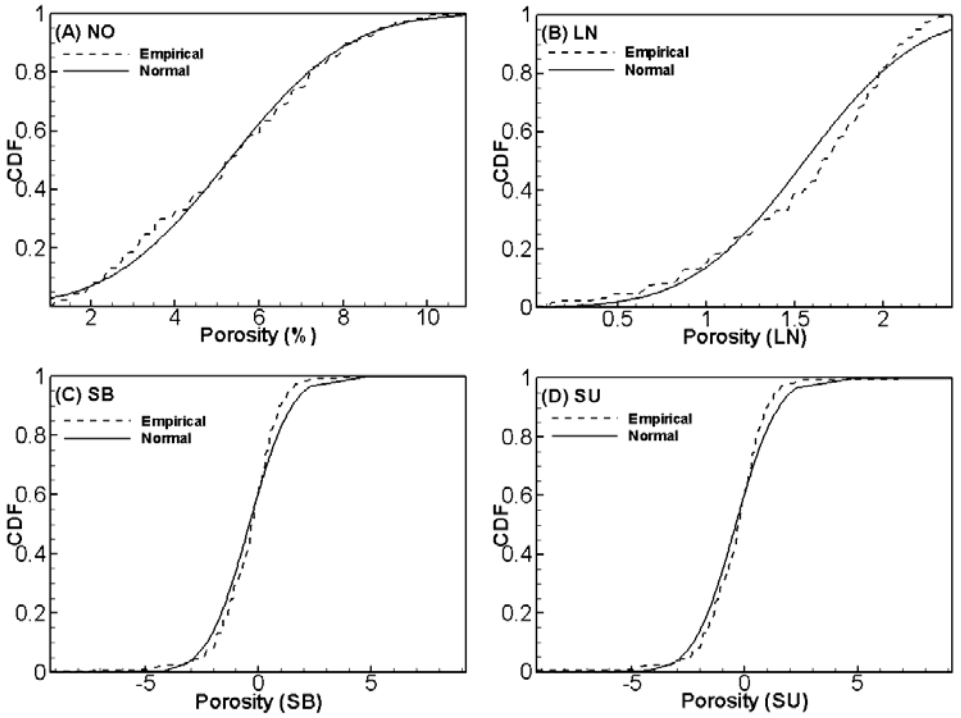

Figure 4-17. Empirical and theoretical cumulative distribution function (CDF) of (a) porosity data and its (b) LN, (c) SB, and (d) SU transformations.

Another uncertain variable is the length of the hydrofracs around the production well. According to Lorenz (2003), it is assumed that the length follows a lognormal distribution. This distribution is assigned a 5th percentile of 40 m and 95th percentile of 150 m, based on the information discussed in the section describing Hydraulic Fracture Characteristics.

Table 4-5. Lilliefors statistics of the original and transformed permeability and porosity. Original permeability was in microdarcies. NO, LN, SB, and SU denote the original data and the three Johnson transformations († denotes selected transformations for permeability and porosity).

Transform	T^* (permeability)	T^* (porosity)
NO	0.2686	0.0724†
LN	0.07929†	0.1222
SB	0.1384	0.0885
SU	0.2563	0.0795
$T(\alpha=0.05)$	0.07488	0.0518

4.8.3 Random Field Generation

Random fields of the above four variables were generated using the Latin Hypercube Sampling (LHS) method, using the LHS code of Iuzzolino (2003). The LHS method is an efficient sampling method and its sampling processes of uncorrelated random variables are as follows (Helton and Davis, 2000):

(1) Divide the range of each variable into *n* intervals with equal probability;

(2) Select one value from each interval randomly;

(3) Pair the obtained *n* values for the first variable with the *n* values of the second variable randomly; and

(4) Combine these *n* pairs randomly with the *n* values of the third variable to form *n* triplets and continue pairing until the last variable is combined with others.

LHS can also consider correlations between different variables using the method of Iman and Conover (1982), who introduced a restricted pairing method based on a desired rank correlation matrix to generate samples with correlations among the variables. While permeability and porosity are in general positively correlated, it is not possible to identify the correlation in this project, since the measurements of permeability and porosity reported in the MWX reports are unpaired. Therefore, uncorrelated permeability and porosity pairs were generated (high values of *k* and low values of porosity lead to high velocity, but if positively correlated, high values of *k* would be unlikely to pair with low values of porosity). Due to the relatively small variation of porosity, the effect of this assumption on the simulation results is expected to be insignificant.

While 500 realizations of random fields of the porosity and anisotropy ratio were generated directly using LHS, 500 realizations of permeability and hydrofrac length were first generated using a normal distribution and then were transformed to a log normal distribution. Figure 4-18 plots the CDFs of the generated permeability fields (in log space), porosity, anisotropy ratio, and the hydrofrac length. The CDFs of the measured permeability and porosity values were also plotted in Figure 4-18. It shows that the distributions of

generated parameters agree well with those of the measurements. Correlations of generated random fields are negligible, indicating that the generated random fields are uncorrelated, which is expected.

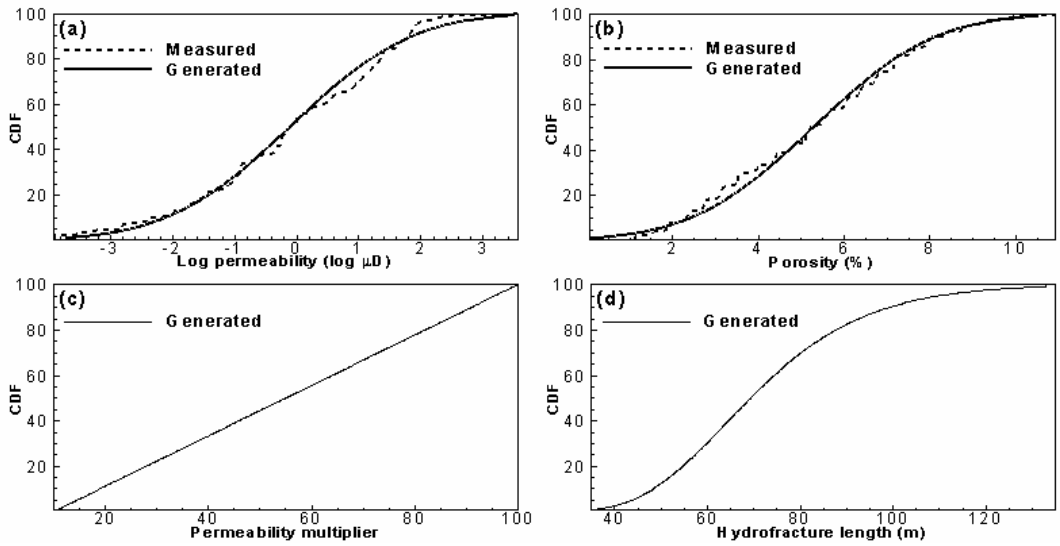

Figure 4-18. Cumulative distribution functions (CDFs) of generated (solid) (a) log permeability, (b) porosity, (c) anisotropy ratio, and (d) hydrofrac length. CDFs of measured (dashed) log permeability and porosity are also plotted in (a) and (b). One microdarcy is equivalent to 9.87×10^{-19} m^2.

The generated realizations of the four random variables are randomly combined with the realizations of the geologic facies. In other words, for each realization of the facies, one set of permeability, porosity, anisotropy ratio, and hydrofrac length is selected randomly, and assigned to the sandstone facies. As a result, 500 realizations of random fields were generated and used in the Monte Carlo simulations for uncertainty assessment.

4.8.4 Numerical Dispersion

Numerical dispersion can be an issue in problems in which the advective-diffusion (or dispersion) equation is solved with upwind finite differencing. This is mostly of concern in strongly advective flows in which sharp fronts (e.g., a separate fluid phase or a dissolved solute) become smeared, leading to unphysical behavior (Zheng and Bennett, 2002). This can be an issue with TOUGH2 because of the integral finite difference formulation with upwind differencing (Oldenburg and Pruess, 2000). However, most of the transport simulations reported here are strongly diffusive, as opposed to advective. Numerical dispersion can be calculated with $(\Delta x / 2)u$ (Zheng and Bennett, 2002), where Δx is the length of a grid block in the *x*-direction and *u* is the *x*-direction velocity. The mesh used in all simulations was uniform (20 m in the *x*-direction) and the maximum gas-phase velocity was on the order of 10^{-8} m^2 s^{-1}. Numerical dispersion was therefore on the order of 10^{-7} m^2 s^{-1}, less than two orders of magnitude than the gas diffusion coefficient for THO in methane (7.26×10^{-5} m^2 s^{-1}). Numerical dispersion, therefore, was not an issue in these simulations. Numerical dispersion in the *y*-direction was of the same order as the *x*-direction, while numerical dispersion in the *z*-direction was about one quarter that of the *x*-direction due to the grid block sizes.

THIS PAGE INTENTIONALLY LEFT BLANK

5.0 MODEL RESULTS

As described previously, the tritium transport calculations are presented in terms of mass fraction of tritiated water, as opposed to concentration of tritiated water (*e.g.*, mg or mol tritiated water to liter of water). Particularly when considering gases, mass fraction simplifies issues of ensuring consistency in the pressure-volume-temperature conditions under consideration (*i.e.*, concentrations in a gas are dependent on volume, which is itself dependent on pressure and temperature). Although mass fraction maintains uniformity as densities vary in the calculation, it can be difficult to intuitively grasp the meaning of the values. This difficulty is heightened because the model results only pertain to subsurface flow and transport processes. Dilution and mixing in the wellbore and other processes involved in any exposure scenario are not included, preventing meaningful comparison of the results to regulatory or health standards. These comparisons can be readily made when the mass fractions are used in an exposure assessment.

The model results are presented in upcoming figures relative to the natural background abundance of tritium. Tritium is produced by gamma radiation in the upper atmosphere and thus occurs naturally, although nuclear testing and other man-made nuclear activities produced much larger amounts. The estimated ratio prior to weapons testing is one tritium atom for every 10^{18} hydrogen atoms, a ratio referred to as a "tritium unit," or TU. With enrichment methods, analytical detection limits as low as 3 TU are possible. The drinking water standard for tritium specified by the EPA in 40 CFR Parts 9, 141, and 142 is approximately 6200 TU per liter of water.

The background value of 1×10^{-18} is an atomic ratio of one tritium atom for every 10^{18} atoms of hydrogen. This is very close, although not exactly equivalent, to the background mass fraction for the liquid phase, with the difference resulting from the mass difference between tritium and hydrogen (a mole of ^3HHO is 20 g whereas a mole of H_2O is 18 g). The true mass fraction for the liquid phase representing the background of tritium prior to human activities is 2.23×10^{-18} g ^3HHO/g H_2O.

The mass fraction results from TOUGH2 for the gas phase are in terms of mass of tritiated water vapor to mass of total gas, for a unit volume. Converting the background atomic ratio to a value somewhat consistent with the model output requires assumptions of saturated vapor density, temperature, and pressure. For example, at standard temperature of zero (0°C) and pressure (1 atmosphere), the saturated vapor density for water in air is 4.85 g H_2O m^{-3} of air. Using the mass fraction for the background ratio of $^3HHO/H_2O$, there would be 1.08×10^{-17} g ^3HHO m^{-3} air. With the mass of a cubic meter of atmosphere at standard temperature and pressure being 1294 g, the mass fraction of a background amount of tritium in the atmosphere under those conditions is 8.4×10^{-21} g ^3HHO g^{-1} air. If 25°C is considered rather than standard temperature, the saturated vapor density become 23 g m^{-3} and the density of air is 1184 g m^{-3}, leading to a mass fraction of 4.3×10^{-20} g ^3HHO g^{-1} air. Given that the comparison must necessarily remain an approximation because the model results represent conditions in the subsurface formation and relate to a methane atmosphere rather than air, the value of 10^{-20} is used as the background mass fraction for tritiated water in the gas phase for plotting purposes.

The following presentation of model results begins by examining tritium migration under the current subsurface conditions of no nearby gas production. Results are then presented for several individual model realizations involving a hypothetical gas-production well to demonstrate factors controlling tritium migration under production conditions. Finally, the composite Monte Carlo results are presented, revealing the overall behavior accounting for uncertainty in lithology, intrinsic permeability, porosity, and hydrofracture length.

5.1 Tritium Migration under Nonstressed Conditions

Though the spatial distribution of geologic units and flow properties varied greatly between realizations, tritium transport under nonstressed reservoir conditions does not vary significantly. Transport during the first 38 years of the simulations (from the time from the Rulison test to the present day) replicates the conditions during these decades, when no production stress has been present. In the absence of this stress, there is no advective movement of liquid or gas. As a result, tritium migrates diffusively outward from the nuclear chimney as a result of concentration gradients. Tritium is initially evenly distributed throughout the model grid blocks representing the chimney. The fractures associated with the nuclear detonation fill with tritiated water vapor within the first 10 years; transport is then much slower into the much lower-permeability surrounding rocks. Tritium transport is solely controlled by gas diffusion, exchange between phases, and radioactive decay. By the end of 38 years, diffusion results in above-background tritium concentrations extending radially about 80 m from the nuclear detonation point. This is essentially extending throughout the nuclear fractured region. This distance is virtually the same between the 50^{th} and 95^{th} percentiles of the realizations, indicating that the uncertain variables included in the model have little impact on the diffusion-driven transport.

A single simulation was run to 500 years without a pressure gradient in order to investigate the overall scale of diffusive transport. The diffusion rate outside the nuclear fractured zone slows such that radioactive decay reduces concentrations to below background beyond the 80-m distance. Thus, 80 m is the general outer bound of diffusive transport under these conditions with radioactive decay. The result that tritium diffusion is limited to 80 m suggests that tritium will be contained within the boundaries of Lot 11, where future drilling is excluded in perpetuity, in the absence of a pressure gradient.

5.2 Factors Controlling Transport for Individual Realizations of the Production Well Scenario

The pumping interval of the hypothetical well in the production scenario is located so that it always corresponds to the closest vertical sand body directly across from the center of the chimney. This causes the pumping interval to sometimes be in different horizons from simulation to simulation. In other words, if a sandstone body was located at the same elevation as the chimney center, the well was located there. If no sandstone was present, then the production interval was moved vertically to the nearest sandstone above or below. The searching routine looked above the chimney center elevation first, so there is a tendency favoring locations higher rather than lower.

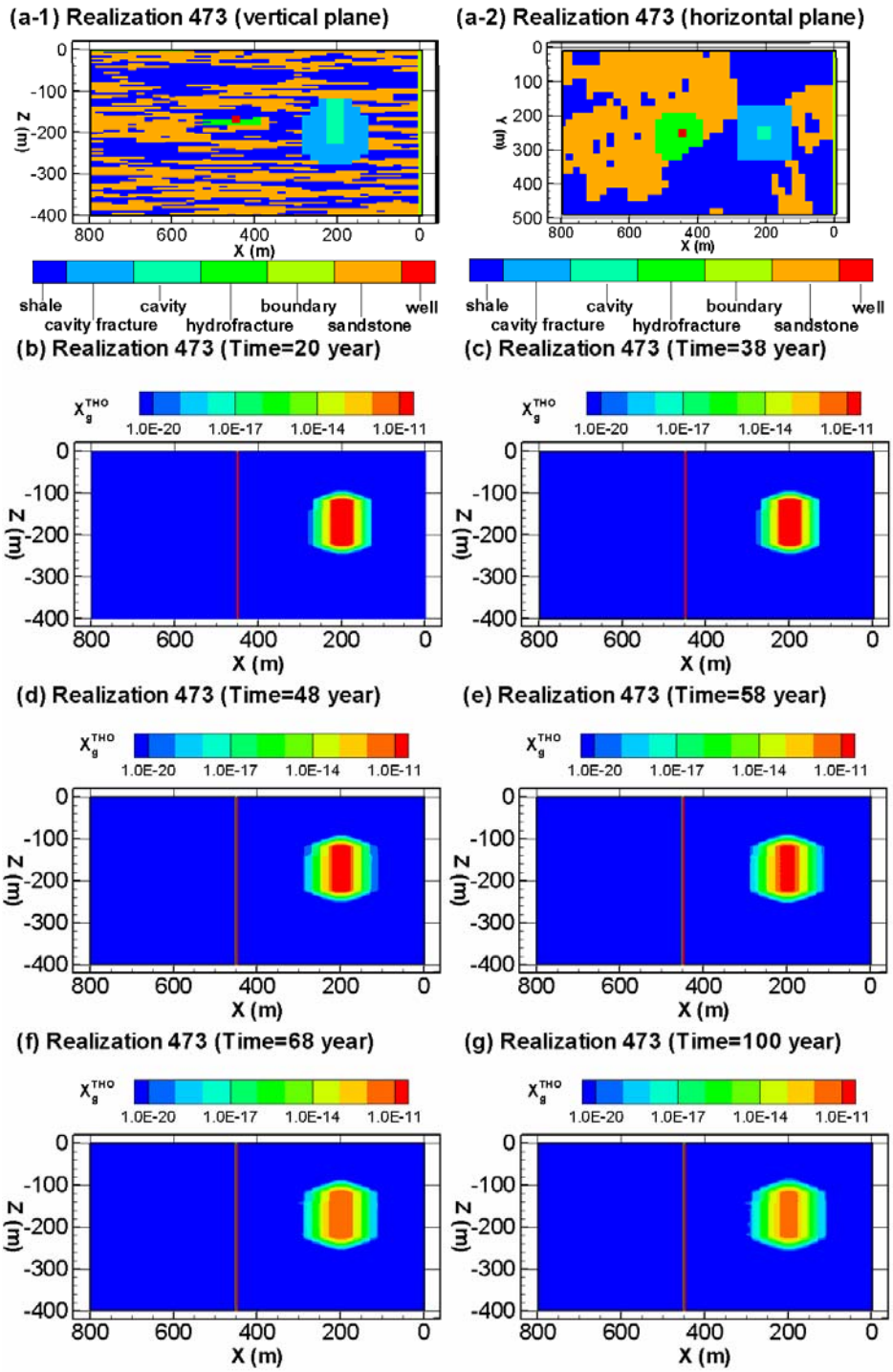

Figure 5-1. Tritium transport simulation for a realization (number 473) with limited connection between the nuclear chimney and hypothetical gas-production well. The top two figures show the permeability field in cross-sectional (a-1) and plan (a-2) views, with the location of the chimney, nuclear fractures, gas-production well, and hydrofractures. Figures (b) through (g) show the mass fraction of tritiated water in the gas (X_g^{THO}) field at 20, 38, 48, 58, 68, and 100 yr following the nuclear detonation. The top of the simulation domain is 2,368 m below the land surface.

Figure 5-1 shows the results of a simulation without a laterally continuous sandstone unit between the chimney and production well. Figure 5-1a-1 is a vertical cross section showing the location of the sandstone (orange) and shale (dark blue) rocks in relation to the chimney (light green and light blue) and well (red square). The well is located 258 m horizontally away from the working point, along the vertical red line seen in Figures 5-1b through g. The preponderance of shale between the chimney and production well is clearer in plan view, as can be seen in Figure 5-1a-2. It shows a horizontal slice of this realization, at the elevation of the production interval. In addition to the sand-shale distribution, this realization also represents hydraulic conductivity values for k_x and k_y=k_z that are at the low end of the distribution, resulting in flow velocities also at the lower end of the distribution. The value of k_x of sandstone in this realization is 2.13 x 10^{-18} m^2 (the minimum k_x is 2.7 x 10^{-19} m^2). Porosity of this realization is 0.0571, close to the mean porosity of 0.0529. For the first 38 years, i.e., prior to gas production at the well, tritium transport, plotted as mass fraction of tritium in the gas phase (X_g^{THO}), is symmetrical away from the chimney into the surrounding rocks (Figures 5-1b and c). Gas production begins 38 years after the nuclear detonation (Figure 5-1c) and continues for 30 years (Figure 5-1d through f). The absence of sandstone continuity between the gas-production well and the nuclear-fractured zone, along with the low permeability of shale units, result in only a slight amount of tritium transport away from the chimney at locations where sandstone exists. No tritium above the background value reaches the well during the production period. At the time production stops (68 years, Figure 5-1f), the dimensions of the mass fraction field have stabilized, and tritium concentration is controlled solely by radioactive decay.

Figure 5-2 shows the results of a simulation with the opposite behavior. In this simulation, tritium was easily transported away from the chimney and mixed with gas such that it was observed at the gas-production well. Figure 5-2a-1 shows the permeability field in a vertical slice. The sandstone lenses where the production well is located are thinner in Figure 5-2a-1 than in Figure 5-1a-1. Vertically, the sandstone unit representing the production zone is better connected to the top of the chimney in this realization than that shown in Figure 5-1a-1. In plan view (Figure 5-2a-2), this realization shows continuous and extensive sandstone between the chimney and production well. The intrinsic permeability of the sandstone is also much higher in this realization, with a k_x value of 2.04 x 10^{-16} m^2 selected from the distribution. Porosity of this realization is 0.0042, about one order of magnitude smaller than that of the realization shown in Figure 5-1. Porosity is inversely related to velocity such that lower values promote transport. The first 38 years of tritium transport (Figure 5-2b,c) are nearly identical to that shown in the previous figure, because transport is controlled by diffusion. However, Figure 5-2d shows a dramatic difference after 10 years of gas production, as compared to the previous realization. Tritium has reached the well through the connection between the sandstone and the upper portion of the chimney, and filled up the hydrofractured rock surrounding the well. In addition, even though gas is produced from a 5-m interval, the combination of pressure gradient and permeability cause the tritium "plume" to intercept the well over a 60-m vertical interval. The dimensions of the X_g^{THO} field are nearly the same in Figures 5-2d through g. As in the previous figure, a quasi-steady state has been reached, and tritium mass fraction field is controlled by radioactive decay.

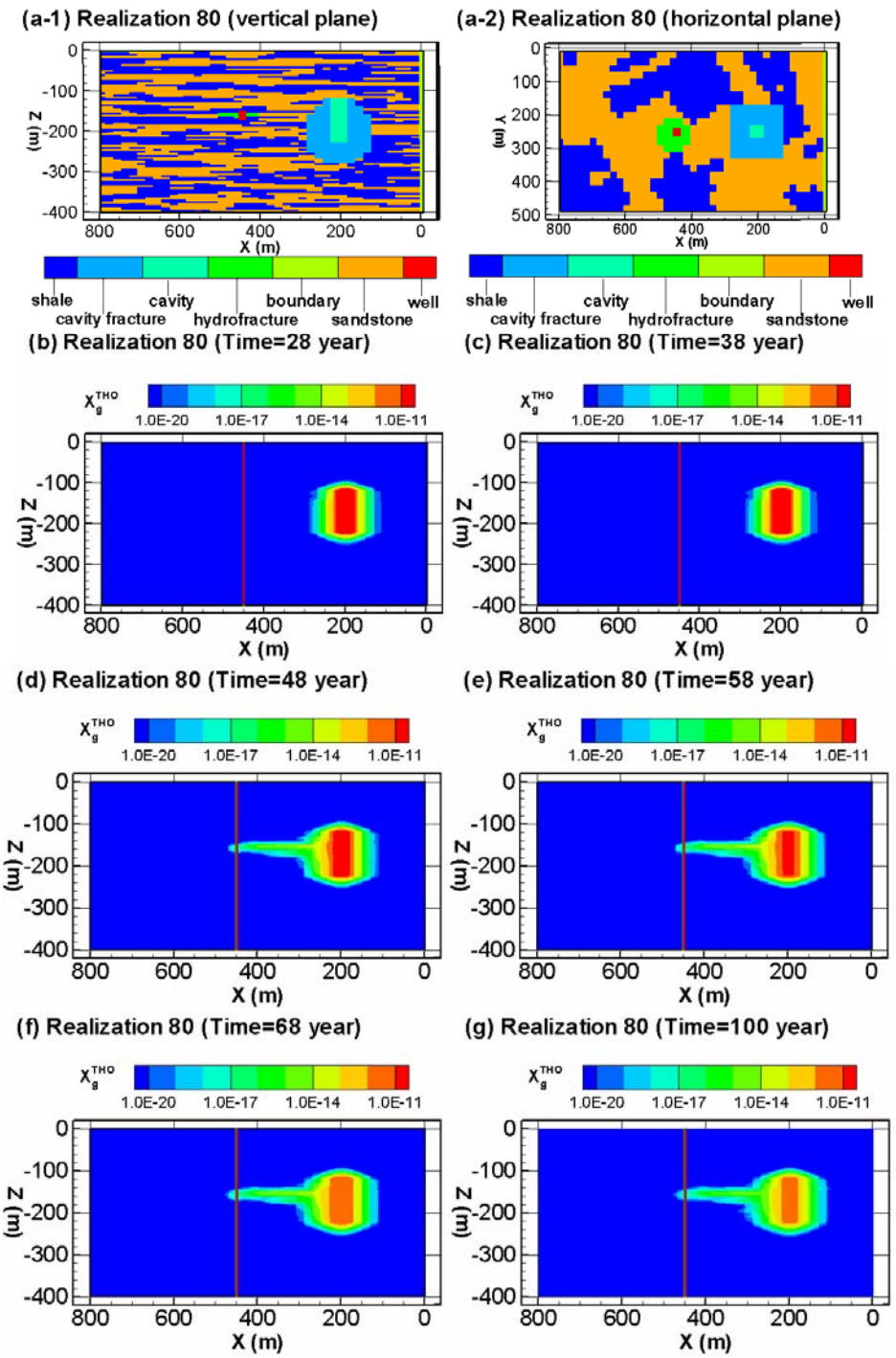

Figure 5-2. Simulation displaying transport of tritium between chimney and production well. The permeability field (a) shows the location of the chimney, fractures, production well, and hydrofracs. (b) through (g) show the mass fraction of tritiated water in the gas (X_g^{THO}) field at 20, 38, 48, 58, 68, and 100 yr following the nuclear detonation. The top of the simulation is 2,368 m below the land surface.

A realization in which the pathlines take a slightly more circuitous route from the chimney to the well is shown in Figure 5-3. The permeability field (Figure 5-3a) shows the perforated interval of the well located just below a shale bed. A 40-m-thick sandstone lies just beneath the shale. As in the other simulations, the shale acts as a trap that does not allow tritium to migrate through it. However, the vertical intrinsic permeability, k_z, of the sand is between the intrinsic permeability of the shale and k_x. This is still large enough to allow gas flow and tritium transport vertically through the sandstone rocks.

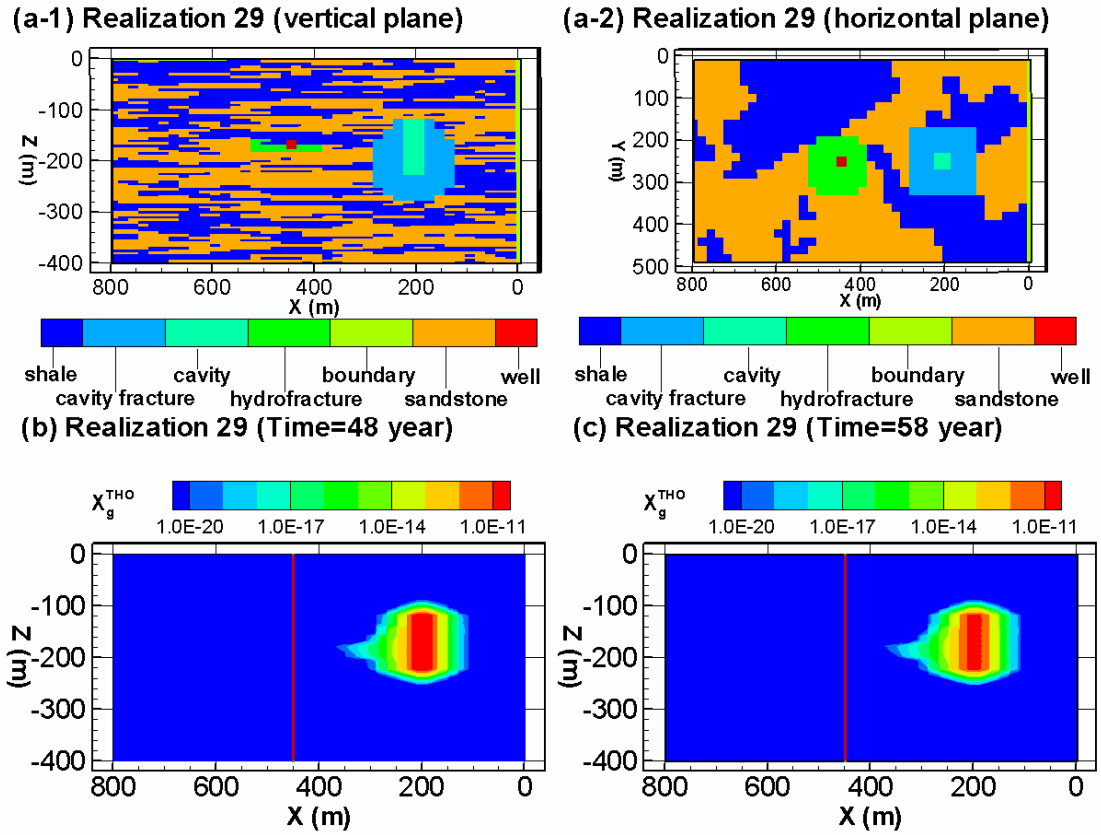

Figure 5-3. Simulation showing plume tritium path upward from the center of the chimney to the production well. The permeability field is shown in (a), and the X_g^{THO} field is shown at times 48 yr (b) and 58 yr (c) following the nuclear detonation. The top of the simulation is 2,368 m below the land surface.

Evaluating the behavior of these individual realizations indicates the importance of the random parameters for controlling transport behavior. The sandstone lens geometry, and its relationship to the pumping interval, are critical in controlling the opportunity for transport from the nuclear chimney to the production well. When the sandstone connection with the nuclear fracture and chimney is present, the k_x value of the sandstone (which is controlled by k_y=k_z [since they are calculated before k_x] and the hydrofracture k) becomes critical, along with the porosity value. The importance of the length of the hydrofracture is dependent on the other factors in that the sandstone geometry must provide a pathway

between the production well and nuclear chimney for the hydrofracture to be effective, and the *k* selected for the sandstone can promote transport even outside of the hydrofracture zone.

The figures all show the X_g^{THO} at various times. The mass fraction of tritiated water in the aqueous phase X_l^{THO} has the exact same shape, but with mass fraction values greater by approximately a factor of two. Maximum liquid-phase velocities are essentially zero, while the highest gas-phase velocities are on the order of 10^{-8} m s^{-1} (< 1 mm day^{-1}). The reason that the tritium exists in the liquid phase is due to equilibrium exchange between the gas and liquid phases.

5.3 Results of the Monte Carlo Analysis of Tritium Transport

Multiple realizations of parameter fields were generated to account for uncertainty in the geometry of the sandstone and shale facies, permeability of sandstone and its anisotropy, porosity, and hydrofracture length. Ranges of these random variables are listed in Table 4-1, which also lists other model parameters that are treated deterministically. Due to randomness of the facies, the location of the production interval of the hypothetical production well is selected in each realization so that it is in the sandstone facies occurring closest to the elevation of the center of the chimney.

Because 500 Monte Carlo realizations were used to calculate the sample statistics (*e.g.*, mean, standard deviation, and percentiles) rather than an ideal, infinite number, the stability of the sample statistics was investigated to ensure that they are reliable to predict system behavior. In general, convergence can be assumed if the statistics stabilize after a certain number of simulations. As there is no theoretical method that can determine the number of needed simulations, an empirical method was used to examine the stabilization of the variables of interest with the number of realizations at representative grid blocks. Figure 5-4 (a and b) shows the mean and standard deviation of tritium mass fraction in the liquid and gas phases, respectively, 58 years after the detonation. The selected grid block, AZD24, was used as the production interval in 229 of 500 realizations. This block was in sandstone (but not the production interval) for 34 realizations and in the shale facies in the other 237 realizations. Due to pumping effects and the alternating sandstone and shale facies, this grid block may have the worst convergence behavior. Although a small decreasing trend exists for both the mean and standard deviation, 500 realizations are considered sufficient, given that convergence at cell AZD24 is an extreme case, in which the convergence is affected by both gas production and alternating hydrofacies.

While various statistics (e.g., mean, variance, 5^{th}, 50^{th}, and 95th percentiles) can be used to assess predictive uncertainty, the 50^{th} and 95th percentiles of predicted mass fraction are used here. The term 50^{th} percentile means that half of the predicted mass fractions (of tritium to total gas, or tritium to total liquid water) are smaller than the value and the other half larger. Similarly, 5 percent of predicted mass fractions are smaller than the value defining the 5^{th} percentile, while 5 percent are larger than the 95^{th} percentile. In other words, the 5^{th} and 95^{th} percentiles bracket 90 percent of the predictions and exclude the 10 percent in the upper and lower extremes. Whereas the 5th and 95th percentiles -- also called uncertainty bounds -- are often used in uncertainty analysis, they exclude extreme events that may be of concern to decision makers and stakeholders. In risk analysis, the first and 99th percentiles are also used to include the extreme events if necessary. The mean and variance of the mass

fraction (or concentration) fields are not used to evaluate tritium transport in this project. The reason is that the computed distributions of mass fraction are not normal due to the combination of lognormal distribution of permeability, normal distribution of porosity, uniform distribution of anisotropy ratio, and lognormal distribution of hydrofracture length. The 50th and 95th percentiles are expected to contain more information of uncertainty than mean and variance.

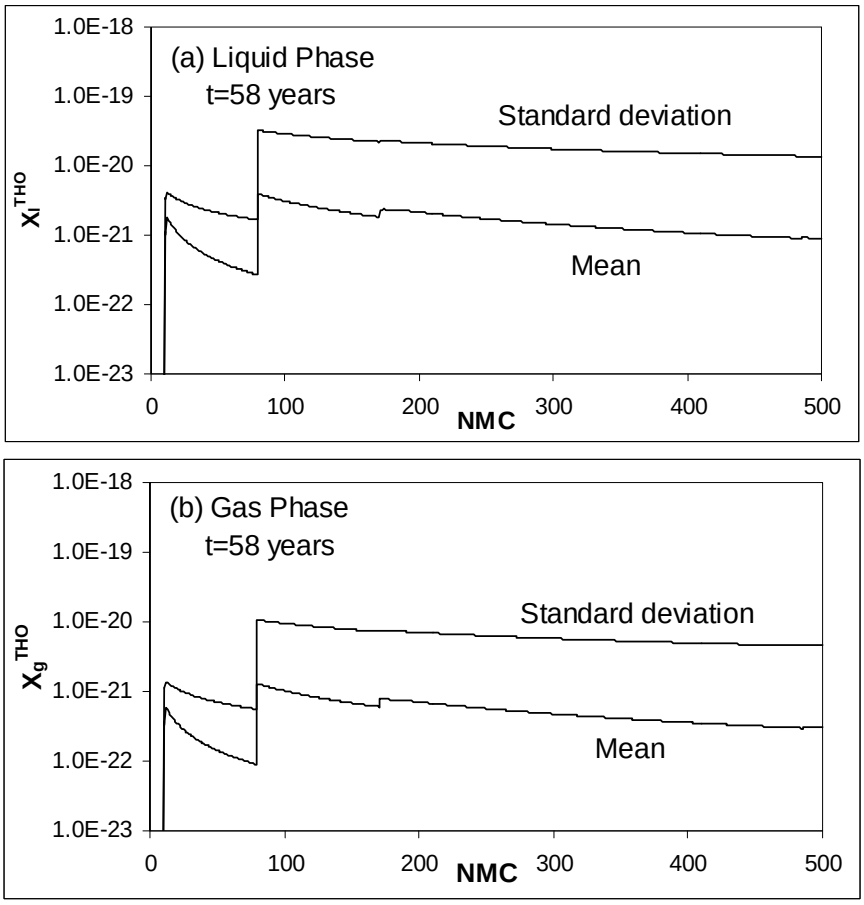

Figure 5-4. Examination of convergence with the number of Monte Carlo (NMC) simulations of mass fractions of tritium at (a) liquid and (b) gas phases.

Figure 5-5 shows plots of the 50th (a1 through l1) and 95th (a2 through l2) percentiles of tritium (as tritiated water) mass fraction in the gas phase (X_g^{THO}). Note that the percentiles are estimated at each grid block of the computational grid such that there is no guarantee, or need, to ensure that the tritium mass was the same for each percentile. Figures 5-5a through e correspond to the period after the detonation but prior to gas production (0 to 38 yr). Uncertainty in tritium transport during this period was small such that the 50th and 95th percentiles are similar. However, uncertainty increases when gas production starts (Figures 5-5f through h, i.e., from 48 to 68 yr), as indicated by the larger size of the plumes of the 95th percentiles, as compared to the 50th percentile. In addition, the shape of the plume of the 95th percentile is more irregular than that of the 50th percentile. This is due to the joint effect of the random permeability fields and differing pumping well vertical locations. Tritium in the gas phase moves faster through high-permeability sandstone lenses; in

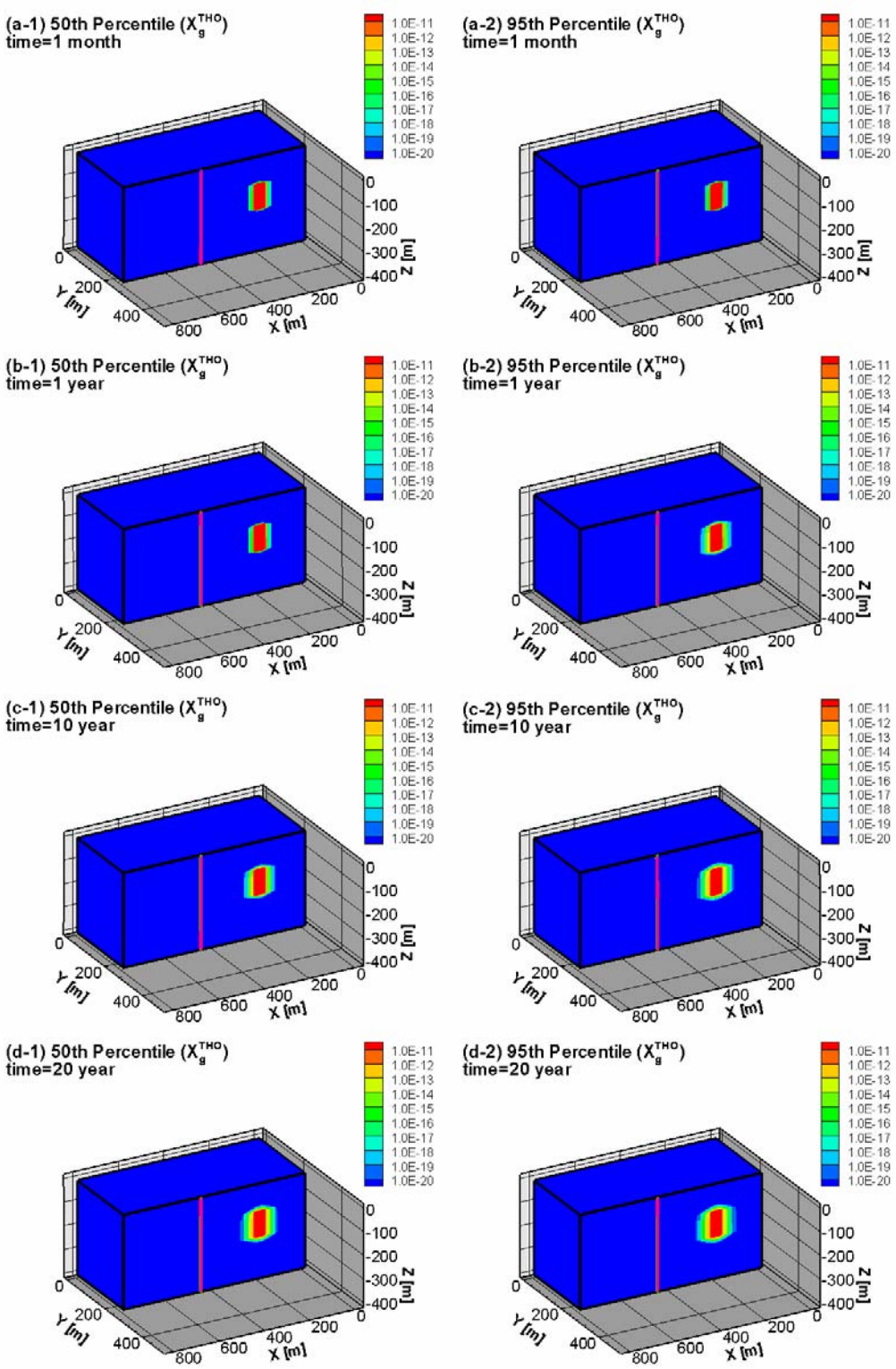

Figure 5-5. (a-1) through (l-1) 50th and (a-2) through (l-2) 95th percentiles of mass fraction of tritium in the gas phase after (a) 1 month, (b) 1 yr, (c) 10 yr, (d) 20 yr, (e) 38 yr, (f) 48 yr, (g) 58 yr, (h) 68 yr, (i) 100 yr, (j) 150 yr, (k) 250 yr, and (l) 500 yr of detonation. The top of the simulation is 2,368 m below the land surface.

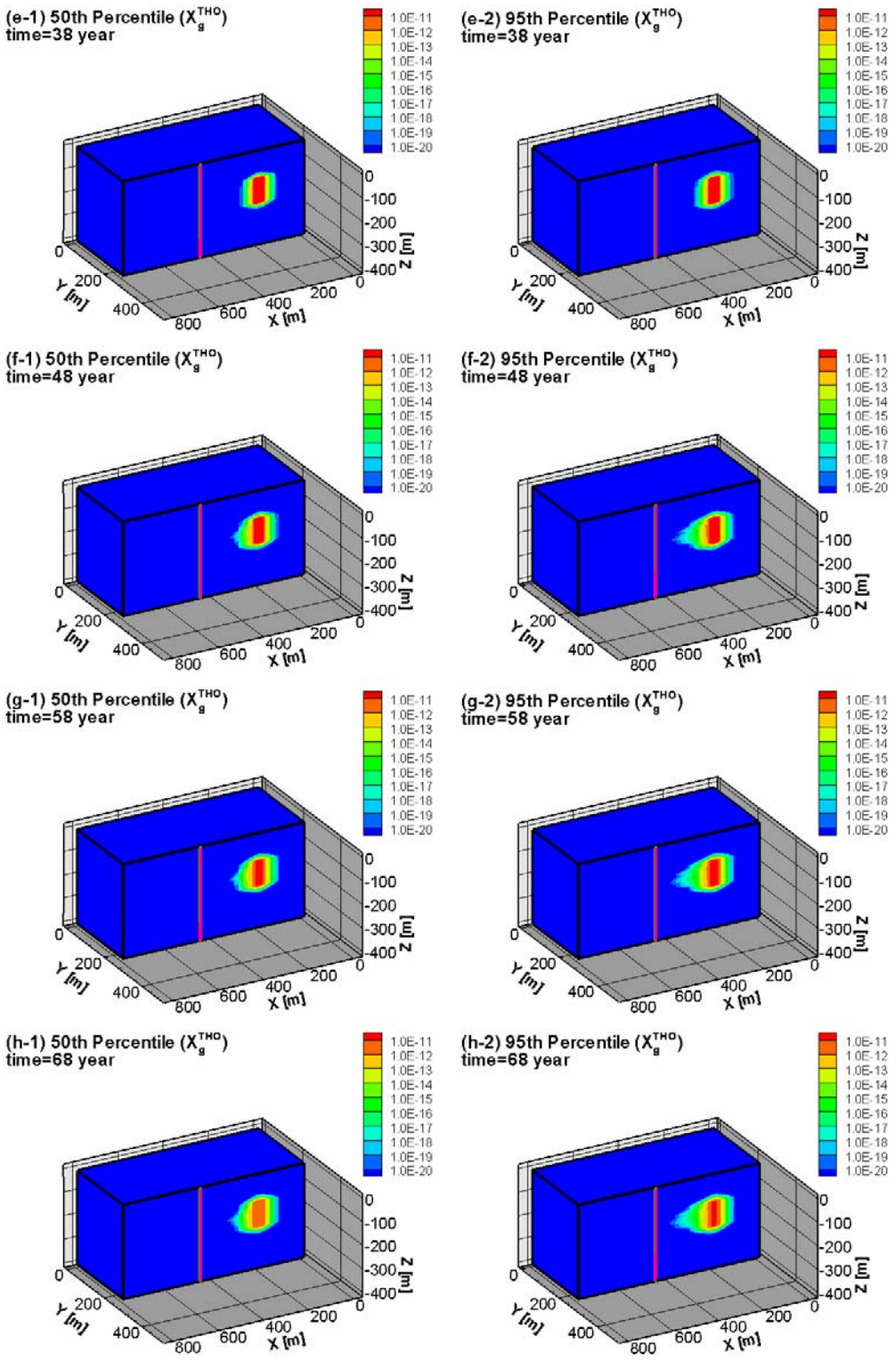

Figure 5-5. (a-1) through (l-1) 50th and (a-2) through (l-2) 95th percentiles of mass fraction of tritium in the gas phase after (a) 1 month, (b) 1 yr, (c) 10 yr, (d) 20 yr, (e) 38 yr, (f) 48 yr, (g) 58 yr, (h) 68 yr, (i) 100 yr, (j) 150 yr, (k) 250 yr, and (l) 500 yr of detonation. The top of the simulation is 2,368 m below the land surface (continued).

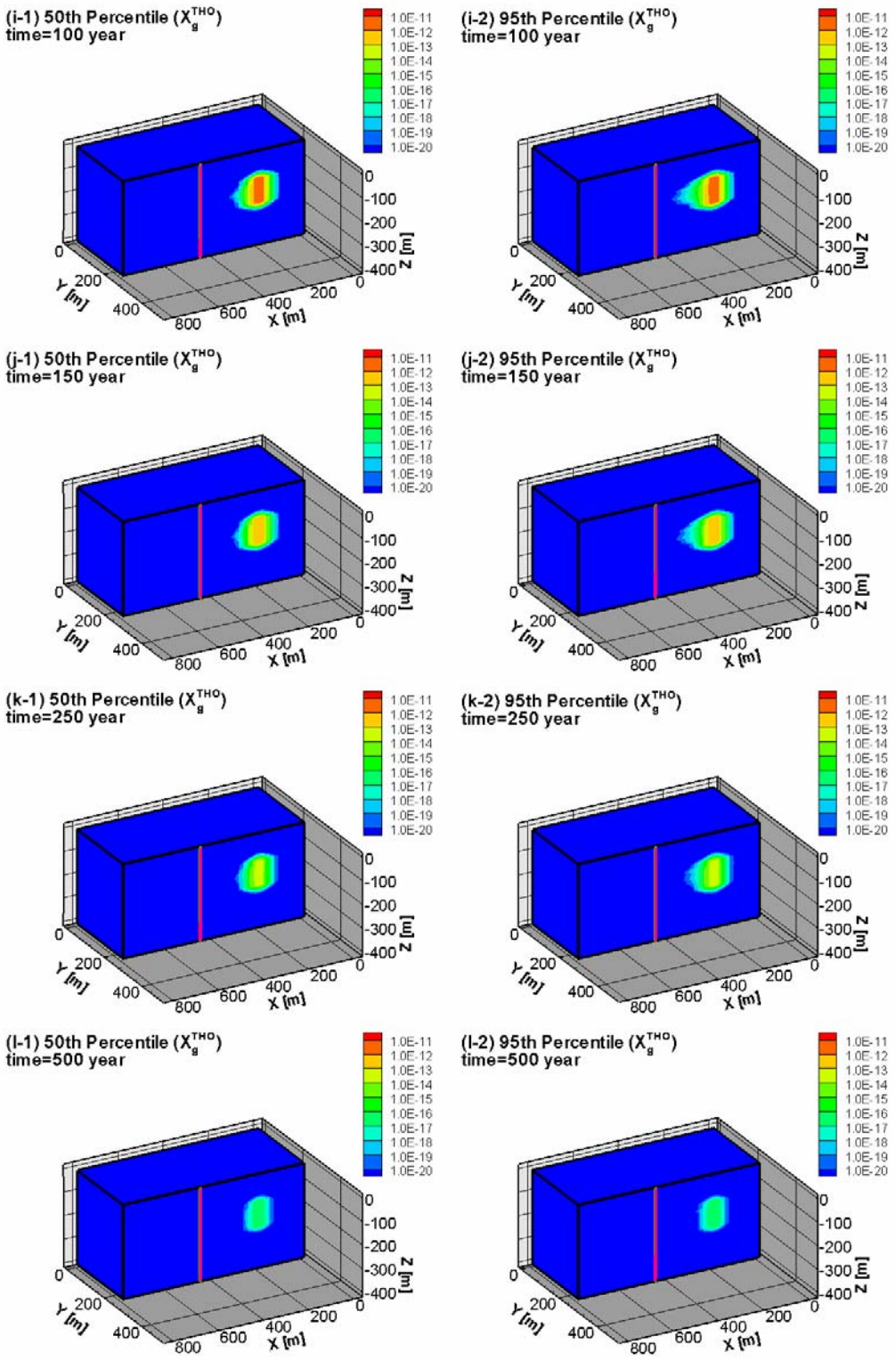

Figure 5-5. (a-1) through (l-1) 50th and (a-2) through (l-2) 95th percentiles of mass fraction of tritium in the gas phase after (a) 1 month, (b) 1 yr, (c) 10 yr, (d) 20 yr, (e) 38 yr, (f) 48 yr, (g) 58 yr, (h) 68 yr, (i) 100 yr, (j) 150 yr, (k) 250 yr, and (l) 500 yr of detonation. The top of the simulation is 2,368 m below the land surface (continued).

addition, gas is produced only from the sandstone. After gas production ceases (Figures 5-5i through l), the velocities in the gas phase slow down, and uncertainty decreases with time. At this time, the spatial distribution of tritium in the gas phase becomes similar in the 50th and 95th percentiles.

Figure 5-6 shows X_g^{THO} in a horizontal plane where the production well is located in 229 out of the 500 realizations. Well locations in other realizations are several grid blocks above or below this elevation. The mass fraction fields are shown for both the 50th (Figure 5-6 a-1 through d-1) and 95th percentiles (Figure 5-6 a-2 through d-2) for 38, 48, 68, and 100 yr after the nuclear detonation. With respect to spreading in the lateral *y*-direction, the greatest transport distance is at x=200, where the chimney is centered. Based on the figures of 50th percentile of mass fraction, spreading is approximately 150 m in either *y*-direction around the chimney. At the well location, however, the maximum distance tritium has spread is approximately 35 m in the *y*-direction. Fracture permeability around the chimney is uniform in the k_x, k_y and k_z directions; in the sandstone and hydrofracs, however, $k_x > k_y = k_z$ by a factor between 10 and 100. This is why spreading in the *y*-direction is greater around the chimney than in the rest of the domain.

Figure 5-7 plots the 5th, 50th, and 95th percentiles of breakthrough curves at the production interval. The 95th percentile results indicate that 95 percent of the realizations did not experience breakthrough of tritiated water vapor above background at a production well located 258 m west of the detonation point. For the 95th percentile, the maximum mass fraction of tritiated water vapor in the gas phase, X_g^{THO}, is 1.01 x 10^{-21}g^{THO}/g^{gas} at 68 years after the detonation. The mass flux values are more easily seen in the breakthrough curves (Figure 5-7) than the mass fraction images (Figure 5-4), because the nearby grid blocks have lower concentrations. X_g^{THO} remains an order of magnitude, or more, below the background value throughout the 500 years of the simulation, even at the 95th percentile. Concentrations above background at the pumping well are observed at the 99th percentile. Mass fractions about one order of magnitude higher than background are observed throughout the pumping period, then reduce below background 150 years after the nuclear test. The maximum X_g^{THO} is 2.33 x 10^{-19}g^{THO}/g^{gas}, observed at 68 years after the detonation, for the 99th percentile.

The relative effect of each random variable on the model outcome can provide information on which variables control the breakthrough behavior and thus are critical to conclusions derived from the results. However, conventional parametric sensitivity analyses are complicated by the random hydrofacies structure of the model. For example, the sensitivity of breakthrough at the production well to porosity cannot be examined independently of the hydrofacies variability; the sensitivity will depend upon the particular sand, shale, and hydrofracture geometry of each realization. Recognizing this difficulty, the computed X_g^{THO} at the hypothetical production well is related to the particular sandstone permeability, porosity, hydraulic fracture permeability, and hydraulic fracture length for the corresponding realization in Figure 5-8. The same model cell and time used to demonstrate convergence in Figure 5-4 (cell AZD24 at 58 years) are used for plots, with this cell being the pumping well in 229 realizations. Figure 5-8 plots the mass fraction and permeability in log scales. The very weak correlations seen in Figure 5-8 indicate that none of the plotted variables dominantly control tritium migration in the simulations. Instead, it is likely that the random hydrofacies distribution is the primary control, with permeability and porosity impacting the results in the context of the hydrofacies distribution.

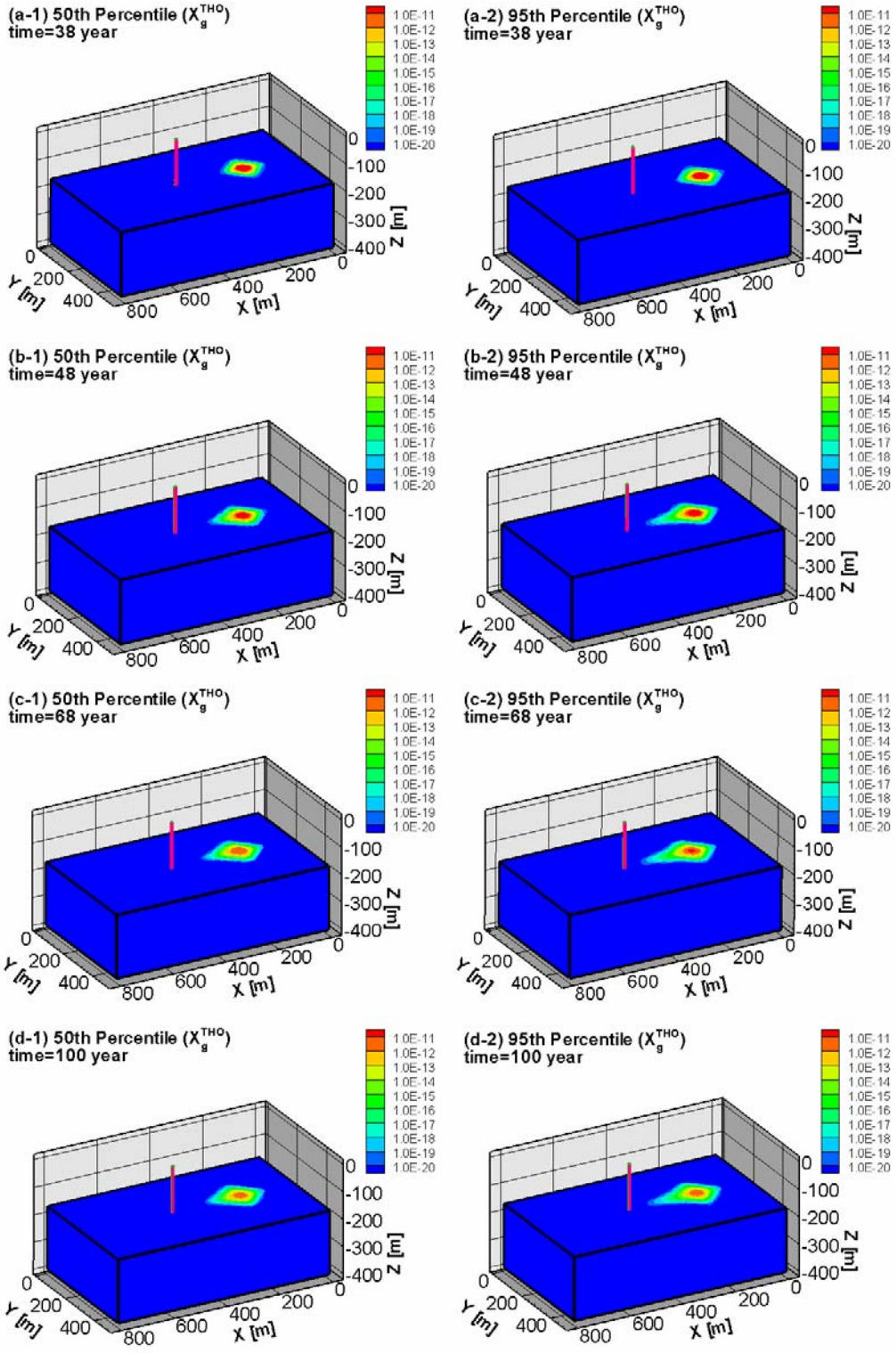

Figure 5-6. Mass fraction of tritium in the gas phase in the horizontal plane at the same elevation of the producing interval. The top of the simulation is 2,368 m below the land surface.

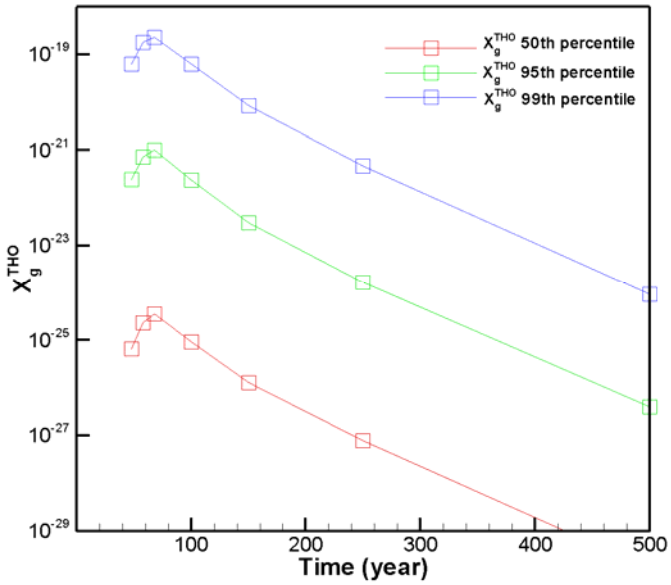

Figure 5-7. Breakthrough curves at the pumping well for the 50th, 95th, and 99th percentiles.

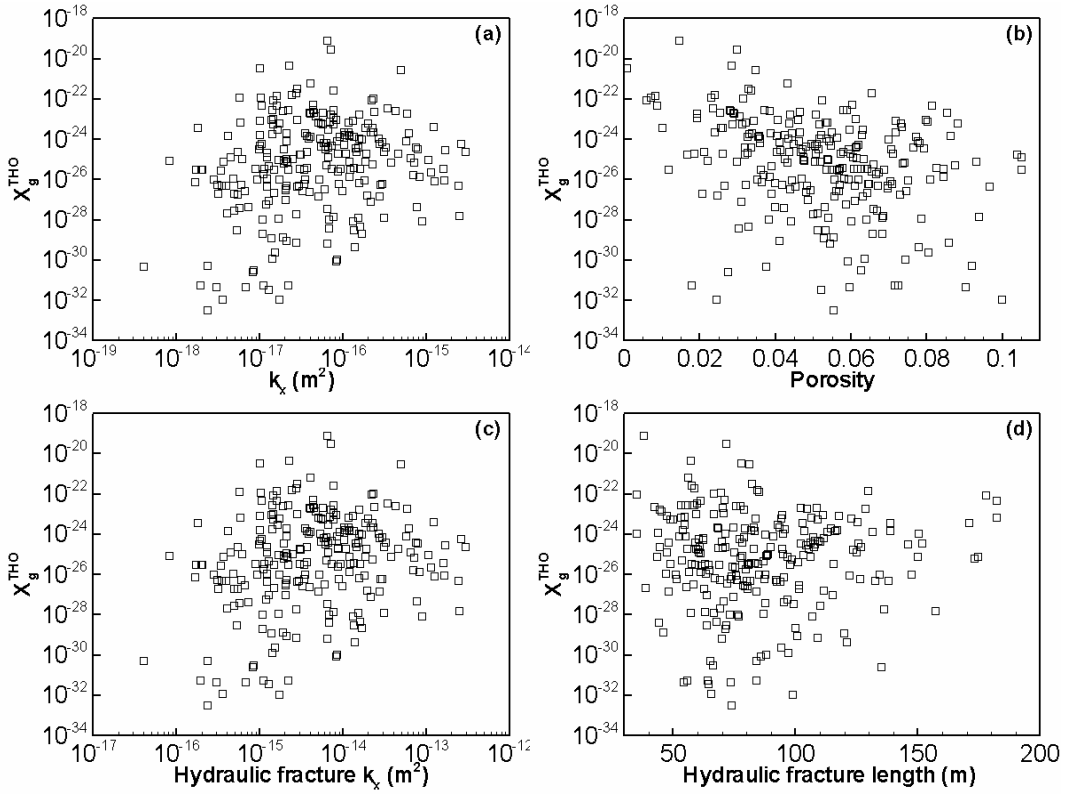

Figure 5-8. Mass fraction of tritium in water vapor at model cell AZD24 for individual realizations, compared to parameter values for that realization. Results are shown for 58 years after the detonation for the 229 realizations in which the cell is in the hydraulic fracture and 34 realizations in which the cell is in sandstone.

6.0 ALTERNATIVE SCENARIO ANALYSIS

Key variables in this modeling analysis of tritium transport include intrinsic permeability, porosity, and the spatial distribution of hydrogeologic units (hydrofacies). Intrinsic permeability and porosity are highly variable, and the spatial distribution of hydrofacies is largely unknown, due to information limited to two boreholes. Given that uncertainty in hydrofacies distribution, intrinsic permeability, and porosity could be critical to the simulation results and conclusions drawn from the results, these quantities were treated as random variables using a Monte Carlo analysis. Instead of analyzing one deterministic set of variables, multiple sets of random variables were considered. The impact of parametric uncertainties on the modeling analysis was assessed by considering different statistics of the results, i.e., the 50^{th} percentile as average system behavior and the 5^{th} and 95^{th} percentiles as uncertainty bounds of system variation. These statistics reveal the impact of parametric uncertainty on the analysis. For example, the peak mass fraction calculated for the hypothetical production well is several orders of magnitude higher at the 95^{th} percentile, as compared to the 50^{th} percentile.

Altogether, the Monte Carlo results of the 500 realizations incorporate uncertainty in sandstone-shale geometry, porosity, permeability along the y and z directions (k_y=k_z), and permeability along the x direction (k_x), hydrofracture length, and permeability of the hydrofractures. Additional uncertainty was present in the problem, but not accounted for in the Monte Carlo results. Rigorous analysis of the impact of uncertainty in other model features would require their evaluation with all 500 Monte Carlo realizations. Future risk calculations with the current Monte Carlo results may indicate whether additional rigorous uncertainty analysis is needed. The impact of several other model features on the modeling analysis is briefly examined below using a selected realization of permeability, porosity, and spatial distribution of hydrofacies.

These additional simulations examined alternative scenarios and conditions held constant in the Monte Carlo runs. These were (1) inclusion of additional production wells, (2) increase in gas production at the existing production well, (3) superposition of a regional, horizontal pressure gradient across the domain, (4) lower porosity for hydrofractures and nuclear fractures, and (5) elevated temperature at the chimney source. Figure 6-1 shows the location of the additional wells. The intrinsic permeability and porosity field used in all simulations except the nonisothermal case is the one (Figure 6-2) that resulted in the 78^{th} percentile breakthrough at the production well in the Monte Carlo simulations. Except for the distinctions pertaining to each simulation, all parameters, as well as the initial and boundary conditions were the same as those presented in Table 4-1. For the nonisothermal case, a simplified layer-cake geology was used, depicting a continuous sandstone layer between the nuclear chimney and the production well and applying the mean values for permeability and porosity from the range (Table 4-1) identified for the Monte Carlo analysis.

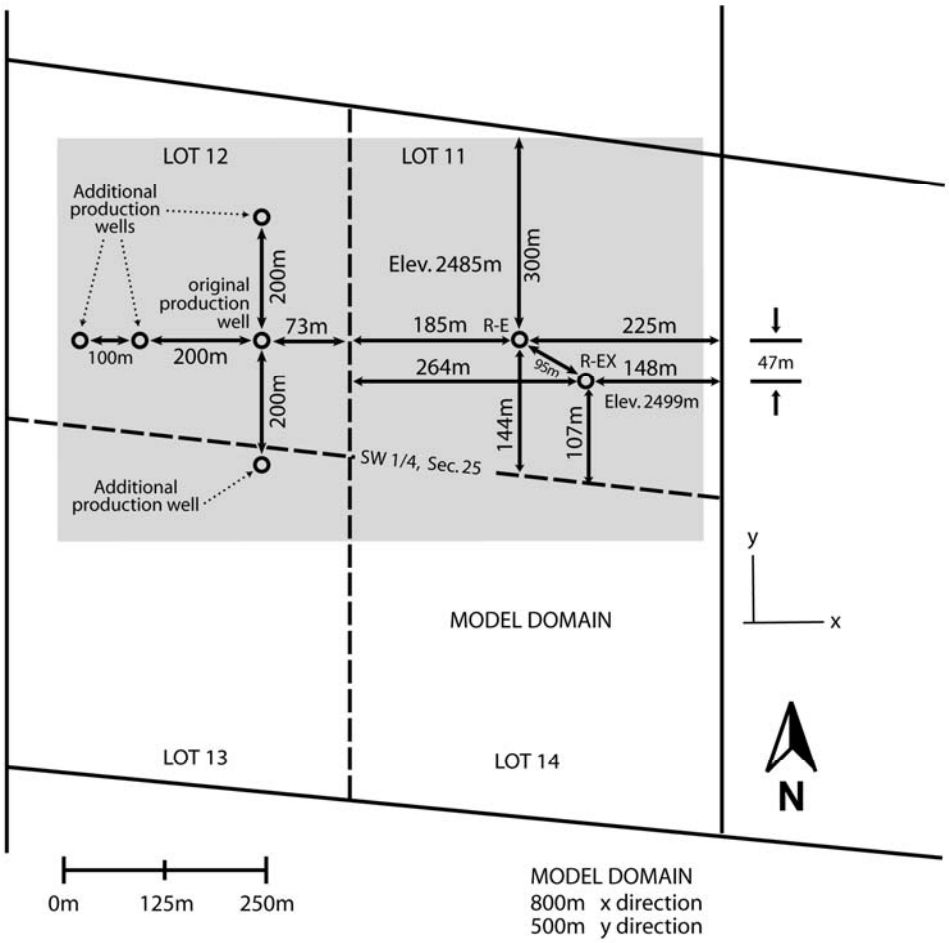

Figure 6-1. Location of the additional production wells.

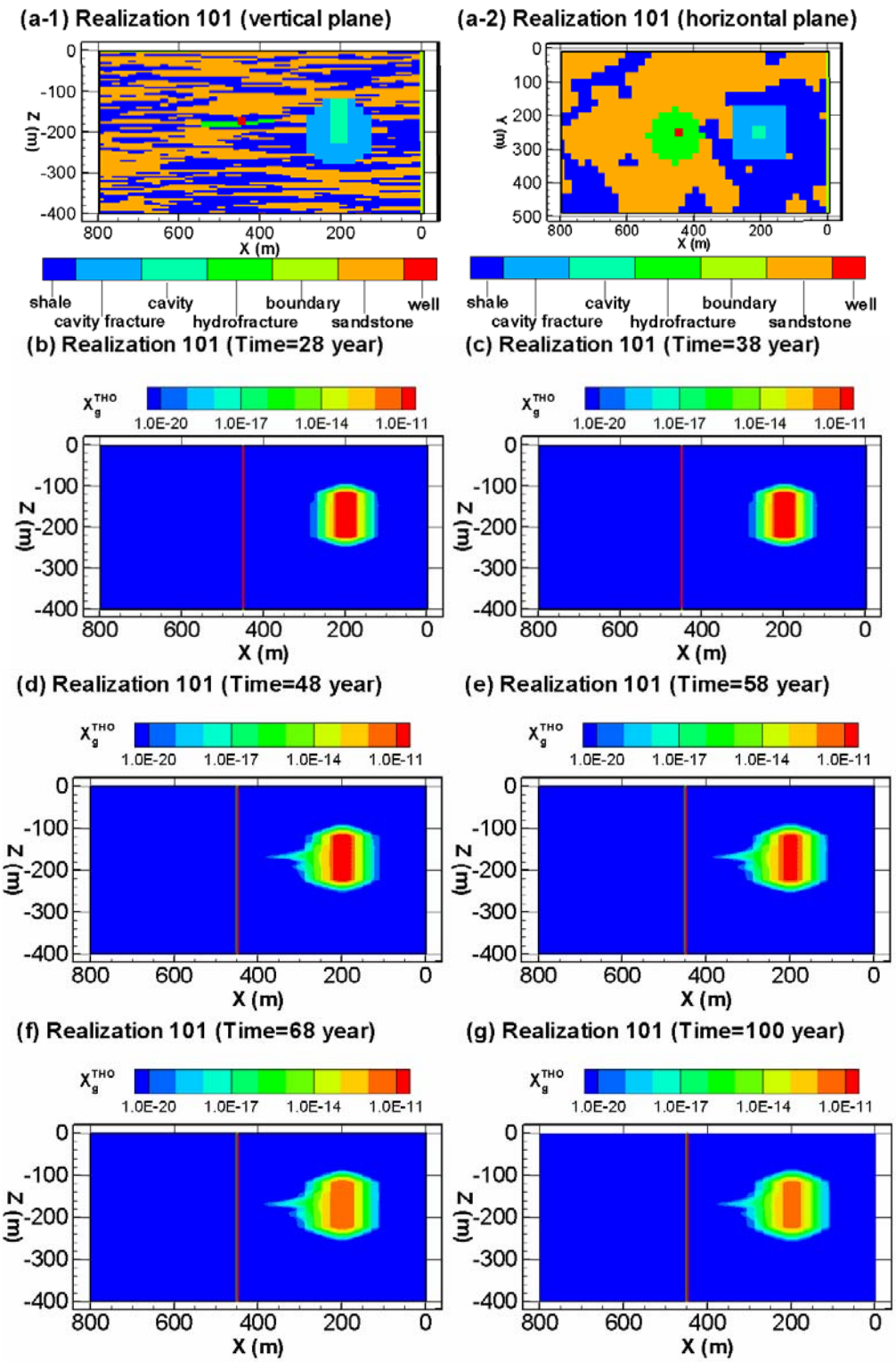

Figure 6-2. Simulation resulting in transport at the 78th percentile of the 500 Monte Carlo realizations. The permeability field (a) shows the location of the chimney, fractures, production well, and hydrofracs. (b) through (g) show the mass fraction of tritiated water in the gas (X_g^{THO}) field at 20, 38, 48, 58, 68, and 100 yr following the nuclear detonation. The top of the simulation domain is 2,368 m below the land surface.

One additional production well to west of the original production well. In this run, an additional well (in addition to the one located 258 m west of the detonation point) was located 200 m west of the hypothetical production well (Figure 6-1). Both wells produced from the same production interval (essentially at the same elevation as the center of the nuclear detonation), had the same production rate, and were turned "on" at the same time. Results of both simulations show that there was never any breakthrough of tritiated water in either the gas or aqueous phases (X_g^{THO} and X_l^{THO}, respectively) at any time, in either well at the production interval. In other words, the second well located to the west did not enhance the pressure field toward the original well, and therefore did not lead to increase in velocities of either the gas or liquid phase. This may be attributed from the large extent of sandstone around the pumping wells (Figure 6-1 and 42, a-2), where natural gas can be produced from.

Two additional production wells located to north and south of the original production well. A simulation was run in which two additional production wells were located 200 m north and 200 m south of the original production well (Figure 6-1). The producing interval for all three wells was the same, that is, at the same horizon as the detonation. The wells were turned on at the same time, and had equivalent production rates. The results showed no breakthrough of tritiated water above background in either phase to any of the wells. The "original" well, located 258 m west of the detonation, had no breakthrough, as was the case for this realization (number 101) in the Monte Carlo analysis. No breakthrough occurred to the two additional wells largely due to the additional travel distance required, as well as due to anisotropy of the permeability field. Recall that *y*-direction intrinsic permeability is two orders of magnitude less than that in the *x*-direction, such that anisotropy acted as a barrier to flow in the north and south directions. The wide spatial distribution of the sandstone may also be a factor.

One well located 560 m west of detonation point. The COGCC currently manages a one-half mile (805 m) radius from the nuclear emplacement well as requiring a hearing before the Commission prior to approval of any drilling application. There is interest in assessing the impact of a production well at that distance, but the domain established for the model does not extend far enough from the detonation point to simulate production at 805 m. Instead, a simulation was run in which the single production well was located 560 m to the west from the detonation point, near the western boundary of the model domain. As could be anticipated from the Monte Carlo results, this resulted in no breakthrough of tritium in either phase to the well. The pressure drawdown around the well did not result in enhanced migration of tritiated water in either phase from the chimney. In other words, under this scenario and for this realization, tritium migration away from the chimney behaved as though it was transported solely due to diffusion.

Increase in gas production. A simulation was conducted with the original scenario, i.e., with the "original" hypothetical production well, but with a 50 percent increase in the rate of production (the production rates shown in Table 4-3 were multiplied by 1.5). This simulation resulted in tritium migration at concentrations above background to a distance of 240 m from the nuclear detonation point, where $X_g^{THO} = 3 \times 10^{-20}$. In the original scenario, tritium above background migrated approximately 180 m from the nuclear detonation point. At the production well, the peak value under the conditions of increased gas production was essentially at background at a value of $X_g^{THO} = 1.1 \times 10^{-20}$, at 58 years.

Regional pressure gradient 0.001 equivalent freshwater head. A simulation in which an east-west horizontal pressure gradient equivalent to 0.001 m m^{-1} of freshwater head (9.81 Pa m^{-1}) was run. This was in contrast to the other simulations in which there was no external horizontal pressure gradient across the domain, except for the local one created by the production well(s). The pressure was highest at the eastern boundary and lowest at the western boundary, such that flow was directed toward the production well. The result was a slight increase in transport as compared to the equivalent Monte Carlo realization (i.e., the same permeability and porosity field) in which no pressure gradient was present. Although no breakthrough of tritium occurred at the production well, the maximum extent of tritium migration away from the chimney was 180 m, essentially the same as in the case with no gradient, except that the concentration was very slightly higher (peak value for X_g^{THO} was 10^{-19} 68 years after the detonation for the gradient simulation and 9.9 x 10^{-20} for the non-gradient case.) The regional pressure gradient has essentially no effect on tritium transport for this realization.

Regional pressure gradient 0.01 equivalent freshwater head. A simulation in which an east-west horizontal pressure gradient equivalent to 0.01 m m^{-1} of freshwater head (98.1 Pa m^{-1}), or ten times the pressure gradient of the above simulation, was run. The results show little change from the case with the 9.81 Pa m^{-1} gradient simulation, suggesting that the overall poor continuity of sand lenses inhibits flow, and that the pressure field created by the production well has a greater effect than the regional pressure gradient. The maximum extent of the plume again reached 180 m from the detonation point, with a peak X_g^{THO} of 2 x 10^{-19}. This is the same extent as that in the simulation above, with a lower horizontal pressure gradient, although the mass fraction is greater in this simulation.

Hydrofracture and nuclear-stimulated fracture porosity held at formation value. For the Monte Carlo simulations, the porosity of the hydrofractures and nuclear-stimulated fractures was selected from the upper end of the porosity distribution of fractured sandstone, under the assumption that those fractures would have higher porosities than natural fractures. The sensitivity of that assumption was tested by running a simulation in which the porosity of the grid blocks representing the hydrofractures and nuclear-stimulated fractures was not altered from that of the native sandstone of the realization. The realization used in these alternative scenarios (realization number 101), has a porosity of 0.048 for the naturally fractured sandstone. This is also the porosity assigned to the hydrofractures and nuclear fractures in this alternative simulation (i.e., the porosity of all sand units is the same throughout the domain). Thus, the hydrofractures and nuclear fractures are represented only by an increase in permeability. At the production well, the peak value under the conditions of reduced hydrofracture and nuclear-fracture porosity was essentially at background at a value of X_g^{THO} = 1.7 x 10^{-20}, at 68 years. This represents only a single intrinsic permeability and porosity realization. In general, low porosity values may not lead to enhanced transport, as suggested by Figure 5-8b. The reason is that in many realizations, porosity (and permeability) impacts the results within the context of the distribution of the hydrofacies.

Initial chimney temperature 226ºC. A simulation was run in which the chimney temperature was initially at 226ºC (U.S. AEC, 1973b) and the rest of the temperature field initially at 101ºC. The chimney was allowed to cool conductively; that is, there was no cooling rate prescribed to it. Results show enhanced tritium transport, as the pressure at the chimney

increased due to the relationship for gases between pressure, temperature, and volume. The X_g^{THO} field extended approximately 50 m further in all directions in the nonisothermal simulation than the same isothermal simulation with identical properties. This result is due entirely to the pressure gradient induced by the elevated chimney temperature as the diffusion coefficient is unaffected by temperature. Temperature-driven pressure increases should, in theory, only happen in thermodynamically closed systems. Gas reservoirs are often considered to be open, but the question is one of time scales. If the time scale of a pressure perturbation far exceeds that of the time of the problem at hand, the reservoir could be considered closed. The time scale of a pressure perturbation to be propagated to the land surface can be determined by $t_c = L^2 / D_{pn}$, where L is a characteristic distance and D_{pn} is the pneumatic diffusivity of the reservoir. The pneumatic diffusivity is $D_{pn} = kP / \mu\theta_g$ where μ is the dynamic viscosity of the reservoir gas. For μ ~ 2.65 x 10^{-5} kg m^{-1} s^{-1}, k ~ 10^{-17} m^2, θ_g ~ 0.5, and P ~ 20 MPa, the pneumatic diffusivity is ~ 1.5 x 10^{-5} m^2 s^{-1}. For a 100-m-long flowpath, the time constants for a gas pressure perturbation might be approximately 21 years. So the reservoir should not be considered as being thermodynamically closed for more than several decades. The elevated chimney temperature results in both enhanced spreading of tritiated water away from the chimney as well as a reduction in tritium mass fraction in both the gas phase and liquid phases within the chimney. The effect of an elevated temperature source on gas transport in a more realistic heterogeneous domain is unknown, however. The simulations were computationally intensive because of the additional temperature equation that needed to be solved. If a risk analysis indicates the information is needed, additional simulations in which the effects of various heterogeneous permeability fields are investigated could be run to determine the sensitivity of tritium transport within a temperature field. It should be noted that the temperature history of the chimney is largely unknown, which will cause significant additional uncertainty.

Whether thermal and hydraulic conditions satisfy convection fluid motion is determined by the dimensionless Rayleigh number, *Ra*, which is a ratio of buoyant forces to viscous and dispersive forces. For flows in porous media, the Rayleigh number is

$$Ra = \frac{\beta \Delta T g k L}{\alpha \nu} \tag{19}$$

where $\beta = \frac{1}{\rho_0}\frac{\partial \rho}{\partial T}$ is the thermal expansion coefficient (assumed constant) [T^{-1}], ΔT is a temperature difference across a length scale L, g is acceleration due to gravity [L t^{-2}], k is permeability [L^2], α is the thermal diffusivity of the gas [L^2 t^{-1}], and ν is the kinematic viscosity of the gas [L^2 t^{-1}]. A rigorous analysis of the onset of convection for gases was developed by Nield (1982), but for no latent heating due to gas compressibility, it reduces to the above form.

The coefficient of thermal expansion is determined from the slope of a plot mass density of air and temperature. Published data at reservoir pressure are difficult to find, but a plot at atmospheric pressure is shown in Figure 6-3.

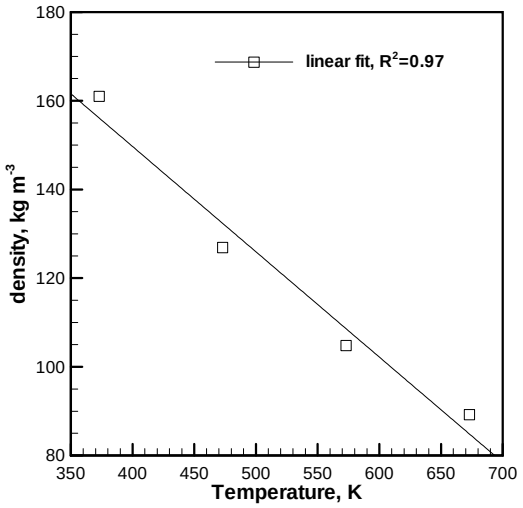

Figure 6.3. Air density versus temperature at atmospheric pressure.

From Figure 6.3 and a reference gas density of ~ 150 kg m^{-3}, $\beta \sim 10^{-3}$ K^{-1}. For a 100 K vertical temperature difference over 100 m, $k \sim 10^{-17}$ m^2, dynamic viscosity $\mu \sim 2.65 \times 10^{-5}$ kg m^{-1} s^{-1} (air at 20 MPa), and $\alpha \sim 3 \times 10^{-7}$ m^2 s^{-1} (for air), *Ra* is equal to 0.02, which is below the criterion for onset of convection (Nield and Bejan, 2006). Based upon linear stability analysis, convection occurs for a critical Rayleigh number $0 \le Ra_c \le 4\pi^2$.

A separate order-of-magnitude analysis of the rise of a buoyant plume supports the Rayleigh number criterion. The vertical velocity of a thermal plume due to buoyancy can be determined by a variable-density version of Darcy's law. A first-order Taylor Series expansion of density is

$$\rho = \rho_o + \frac{\partial \rho}{\partial T} \Delta T \qquad (20)$$

where ρ is mass density of the gas, ρ_o is a reference density, and *t* is temperature. Insertion of Equation (20) into Darcy's law, and considering only buoyancy forces, the vertical component of Darcy's law for a buoyant plume becomes

$$w = \frac{-k}{\mu} g \rho_0 \beta \Delta T \qquad (21)$$

where *w* is the vertical velocity. For the above characteristic values, $w \sim 6 \times 10^{-11}$ m s^{-1}, which is too small to be of significance. However, there may be convection in the chimney fractures, with their higher intrinsic permeability, but almost nothing is known about the nature of thermal convection of fluids in fractures (Nield, 2006).

THIS PAGE INTENTIONALLY LEFT BLANK

7.0 SUMMARY, DISCUSSION, AND CONCLUSIONS

The purpose of the modeling analysis described in this report is to evaluate the degree of tritium transport in the subsurface as a result of migration under ambient conditions and as a result of natural-gas production from a hypothetical production well. This includes diffusion of tritium in liquid and gas phases away from the chimney and the effect of a gas well producing at the event horizon several hundred meters away. A numerical model was developed using the TOUGH2 simulator to evaluate the transport of tritium (as tritiated water) in both the gas and liquid phases, exchange between phases, and radioactive decay. The use of numerical models to simulate complex subsurface systems requires approximations of reality. A fundamental approximation used for Rulison is that the natural fracture flow system is represented numerically as an equivalent porous medium. This means that discrete fracture flow is not simulated, though the model is designed to replicate fracture flow characteristics. Input data for the model were gathered from published sources. Values for several key parameters, however, are uncertain. These parameters include the geometry of sandstone and shale layers, intrinsic permeability and porosity of the sandstone beds, and intrinsic permeability of fractures induced by hydrofracturing treatments in a hypothetical production well. These uncertainties were handled by a Monte Carlo method, which generates multiple realizations of the parameters and runs the simulator hundreds of times to determine the average estimate (the 50^{th} percentile) for the concentration field of tritium (reported as mass fraction, or mass of tritiated water per total mass of the particular phase per unit volume) in the gas and liquid phases. Uncertainty (the 5^{th} and 95^{th} percentiles) associated with the average estimate were also evaluated from the Monte Carlo results.

The simulations were run such that tritium transport away from the chimney was modeled in the absence of an external pressure gradient for 38 years (from the time of the nuclear test in1969 until 2007). During this time, tritium transport was controlled by molecular diffusion, phase exchange, and radioactive decay. The maximum travel distance of tritium during the 38 years was approximately 80 m away from the nuclear emplacement well. This is also the overall maximum distance of diffusion through time because radioactive decay reduces concentrations to below background as diffusion past 80 m occurs. The results were similar irrespective of the particular permeability and porosity field, indicating that the permeability field has little effect on diffusive transport of tritiated water in either phase. In fact, molecular diffusion is controlled primarily by the porosity and tortuosity, which were varied in the simulations. The fact that diffusion distances were similar irrespective of the permeability and porosity realization suggests that the calculations of diffusion-controlled transport, prior to 38 years, are fairly certain. The result that tritium diffusion is limited to 80 m suggests that tritium will be contained within the boundaries of Lot 11, where future drilling is excluded in perpetuity, in the absence of a pressure gradient.

After 38 years of ambient conditions, the model introduces a hypothetical gas-production well, located 258 m from the nuclear emplacement well. The well is located in the direction most vulnerable to migration, outside the DOE drilling restriction. This is due west of the nuclear test because anisotropy in the permeability field favors flow in an east-west direction, and the Lot 11 boundary is closer west of the nuclear test than east. Gas production induces a pressure gradient such that tritium transport during production is controlled by both gas diffusion and advection. Once gas production begins 38 years following the detonation,

transport can be greatly enhanced in the location of the producing well, depending on the flow conditions of each permeability and porosity realization. Gas production lasts for 30 years, that is, between 38 and 68 years after the nuclear detonation.

Results of the Monte Carlo simulations suggest that the production well will not capture tritium from the nuclear test above background values at the 95^{th} percentile. The peak mass fraction of tritium in the gas phase at the 95^{th} percentile is 1.01×10^{-21} g of THO per g of gas, occurring at 68 years. Concentrations of tritium are above background, within an order of magnitude, at the 99^{th} percentile during the gas-production period. The peak mass fraction of tritium in the gas phase at the 99^{th} percentile is 2.33×10^{-19} g of THO per g of gas at 68 years. Note that the total mass fraction decreases through time due to radioactive decay of tritium (which in 2007 has already decayed over three half-lives since the detonation). Other gas phase radionuclides could be expected to have different transport behavior because some of these would not partition as readily into liquid phases, and the radionuclide half-lives vary. However, tritium is the only gas-phase radionuclide with substantial mass remaining after Rulison production testing.

The mass fractions reported here represent mass fractions introduced at one simulated pumping interval. An actual gas production well is likely to have many perforated intervals in one production well, such that mixing and dilution occurs in the wellbore. When brought to the surface, gas volumes expand approximately 135 times while the liquid phase is nearly incompressible at the pressure and temperature considered here. Because tritium mass fractions simulated here are normalized to the mass of either phase, gas expansion should not be a factor, such that the values reported remain constant regardless of pressure and temperature changes. Expansion of the gas phase when brought to the land surface could, however, be important in models of dose assessments where exposure to members of the public are concerned, as well as processes of mixing and dilution. The model presented here only simulates subsurface flow and transport and does not represent processes and factors critical to exposure and dose.

The most important variables affecting tritium migration are the spatial distribution of sandstone and shale units in the subsurface and their intrinsic permeabilities and porosities. Uncertainty in these features and parameters, and in the length and permeability of hypothetical hydrofractures at the pumping well, are directly included in the Monte Carlo analysis. Only one gas-production scenario is examined by the Monte Carlo analysis and it is hypothetical and designed to represent production from the location most vulnerable to transport. Other production scenarios (different well locations and different production rates) and other conditions (such as a regional pressure gradient or nonisothermal conditions) could undergo Monte Carlo analysis if risk calculations suggest additional analysis is warranted. These features were examined for a single realization, the one at the 78^{th} percentile of the Monte Carlo results, but they did not alter the outcome of essentially no breakthrough of tritium at the production well(s) above background conditions. Including heat generated by the nuclear tests, increasing gas pumping rates, and reducing hydrofracture porosity were observed to increase radionuclide transport distances, though not in significant concentrations to the distance of the production well in the one realization tested.

Tritium migration is only influenced by the production well if the well's drainage radius intercepts the tritium diffusing from the chimney. The location of wells other than in the most vulnerable location modeled here can be anticipated to be of little importance, because wells located off the direction of maximum intrinsic permeability (i.e., those located to north and south of the production well in the Monte Carlo simulations) are unable to capture tritium due to the strong anisotropy favoring flow in the east-west direction. In addition, wells located further away from the detonation point than the modeled hypothetical production well used in the Monte Carlo simulations, may not induce a large enough drainage radius to enhance tritium transport. The simulations all assume that the gas production interval is at the elevation of the nuclear chimney. Anisotropy in the *z*-direction would confine vertical transport in the same manner that *y*-direction anisotropy limits transport, that is transverse to the predominant (*x*-direction) flow field.

7.1 Conclusions

The following conclusions can be drawn regarding the specific objectives identified for analysis with the Rulison model:

- Objective 1: Calculate the nature and extent of tritium contamination in the subsurface from the Rulison test, from the time of the test to present day (2007)

Migration of tritium from the Rulison test in the absence of nearby gas-field production is driven by diffusion. Diffusion is rapid through the region fractured by the nuclear test, but is slow in the surrounding region. Maximum migration of tritium (meaning tritium above background levels) is estimated to be no more than 80 m from the nuclear test working point, with radioactive decay eliminating the radionuclide mass prior to any further migration. The extent of tritium migration is nearly the same for each permeability and porosity realization, as diffusion is affected only by porosity, through the tortuosity term. Note that other gas-phase radionuclides, such as ^{85}Kr and ^{14}C, are recorded as largely removed from the subsurface during Rulison production testing. If they were present, their transport behavior would be different from tritium because they would not be expected to partition as significantly into the relatively immobile liquid phase.

- Objective 2: Determine the most vulnerable natural-gas production well location, outside the DOE drilling restriction, in terms of inducing tritium migration from the Rulison test and evaluate migration under gas-production conditions.

Subsurface formation properties and site geography indicate that the production well location likely to promote maximum transport from the Rulison test is due west 258 m from the nuclear emplacement well. Anisotropy in *k* causes preferential flow in the east-west direction. The edge of Lot 11 (which defines the DOE drilling restriction) is 185 m west of the nuclear test, as compared to 225 m to the eastern boundary. Current COGCC requirements for set-backs from drilling boundaries add another 73 m of distance, resulting in a location 258 m west of the Rulison test. Vertically, the gas-production zone is assumed to be in the sandstone unit that is closest to the elevation of the center of the nuclear chimney. This zone is further assumed to be hydraulically fractured. Gas production is assumed to occur for 30 years and constitutes volumes consistent with one-tenth of the production of an average well in the area (thus assuming the well includes 10 perforated intervals, one of which is at the nuclear test elevation). This hypothetical gas-production well impacts migration of tritium from the nuclear chimney in many realizations, significantly enhancing

migration in the direction of the pumping well. Though tritium migration westward is promoted, concentrations above background did not arrive at the production well in over 95 percent of the model realizations. The peak mass fraction of tritiated water vapor contained in the gas phase at the 95th percentile is 1.01 x 10^{-21} g^{THO} g_{gas}^{-1} entering the production well at the pumping interval 68 years after the nuclear test. Concentrations at the wellhead would be lower as a result of mixing with gas from other production intervals. It is important to realize that the model reported here is limited to an examination of subsurface flow and transport. This model does not explore impacts of dilution and mixing in the wellbore, nor exposure scenarios and thus the results cannot be extrapolated to doses or compared to regulatory requirements related to either exposure or dose in any manner other than as a point of reference for understanding the mass fraction values.

- Objective 3: Assess the effect of uncertainty in the calculations

Solution of the two-phase flow and transport problem for a complex, sparsely observed, deep subsurface environment requires approximations and assumptions that lead to uncertainty in the outcome. Some of these uncertainties are inherent and difficult to quantify, others can be included directly in the analysis. Unquantified uncertainties include aspects such as the equivalent porous medium and equilibrium assumptions, and the treatment of tortuosity. Uncertainties directly included through the use of Monte Carlo techniques are values for permeability, porosity, hydrofracture length, and hydrostratigraphy. Additional conceptual uncertainties were addressed by discrete alternative scenario analysis.

Despite significant uncertainty in hydrostratigraphy and formation properties, the uncertainty is small in the Monte Carlo results of the simulation of tritium migration under natural conditions from the time of the test until present day. Transport under the non-stressed conditions is by diffusion, which is insensitive to the uncertain permeability field. Uncertainty increases once the hypothetical production well begins pumping and advection becomes a dominant transport process. The random permeability and porosity fields, as well as varying vertical location of production, result in mass fraction values several orders of magnitude higher at the 95th percentile as compared to the 50th percentile. However, given the limited transport observed, this level of uncertainty does not affect the conclusion of no tritium transport to the hypothetical production well above background levels, at the 95th confidence interval. Alternative scenario analyses performed for a single realization found that the production well location, multiple production wells, production rate, regional pressure gradient, hydrofracture porosity, and temperature effects did not result in breakthrough at the hypothetical production well essentially above the estimated background level. Production rate, hydrofracture porosity, and temperature effects were found to promote transport in the single realization tested. Rigorous assessment of the uncertainty contributed by those scenarios would require additional Monte Carlo analysis, which can be performed if future risk evaluations indicate the information could be important.

8.0 REFERENCES

Anspaugh, L.R., J.J. Koranda, and W.L. Robison, 1971. Environmental Aspects of Natural Gas Stimulation Experiments with Nuclear Devices, in Nelson, D.J. (ed.) Radionuclides in Ecosystems. National Technical Information Service, Springfield, Virginia, pp.37-52.

Austral Oil Company and CER, 1966. Project Rulison Feasibility Study. Prepared for the U.S. Atomic Energy Commission, report PNE-R-12, 38p. plus figures and appendices.

Bear, J., 1988. Dynamics of Fluids in Porous Media. Dover reprint of 1972 Elsevier edition, 764 pp.

Borg, I.Y., 1970. Survey of Piledriver Results and Preliminary Interpretation of Three Postshot Cores In and Near the Cavity. Lawrence Livermore National Laboratory, report UCRL-50865, 66p.

Borg, I.Y., 1973. Extent of pervasive fracturing around underground nuclear explosions. *Int. J. Rock Mech. Min. Sci.*, 10:11-18.

Borg, I.Y., 1975. Radioactivity trapped in melt produced by a nuclear explosion. *Nuclear Technology*, 26, 88-100.

Borg, I.Y., R. Stone, H.B. Levy, and L.D. Ramspott, 1976. Information Pertinent to the Migration of Radionuclides in Ground Water at the Nevada Test Site Part 1: Review and Analysis of Existing Information. UCRL-52078 pt.1, Lawrence Livermore National Laboratories, 216p.

Bowen, W.M. and C.A. Bennett, 1988. Statistical Methods for Nuclear Material Management. Battelle Pacific Northwest Laboratory, NUREG/CR-4604.

Bowen, S.M., D.L. Finnegan, J.L. Thompson, C.M. Miller, P.L. Baca, L.F. Olivas, C.G. Geoffrion, D.K. Smith, W. Goishi, B.K. Esser, J.W. Meadows, N. Namboodiri, and J.F. Wild, 2001. Nevada Test Site Radionuclide Inventory, 1951-1992. Los Alamos National Laboratory Report LA-13859-MS, 28 p.

Brooks, R.H. and A.T. Corey, 1964. Hydraulic properties of porous media. Hydrology paper No. 3, Colorado State University, Ft. Collins, CO.

Burger, L.L., 1979. Distribution and reactions of tritiated hydrogen and methane. *In*, International Atomic Energy Agency, Behavior of tritium in the environment, Proceedings Series, Vienna IAEA-SM-232/54, STI/PUB/498, pp.47-64.

Carle, S.F., 1999. T-PROGS: Transition Probability Geostatistical Software, Version 2.1, University of California, Davis.

Carsel, R.F. and R.S. Parrish, 1988. Developing joint probability distribution of soil water retention characteristics. *Water Resour. Res*., 24(5):755-769.

CER Corp., 1969. Project Rulison Definition Plan. Report prepared for U.S. Atomic Energy Commission, PNE-R-11, 178p.

Coffer, H.F., G.W. Frank, and B.G. Bray, 1971. Project Rulison and the Economic Potential of Nuclear Gas Stimulation. In Drilling and Production Practice 1970. American Petroleum Institute, Washington, D.C., pp.165-180.

Cole, R.D. and S. Cumella, 2004. Fluvial sand-body dimensions in the Lower Williams Fork Formation (Upper Cretaceous), Southwestern Piceance Basin, Colorado. Rocky Mountain Section AAPG Meeting, August 9-11, 2004, Abstracts. Denver, Colorado.

Cooper, C.A., M. Ye, J. Chapman, and C. Shirley, 2005. Radionuclide Migration at the Rio Blanco Site, A Nuclear-stimulated Low-permeability Natural Gas Reservoir, Desert Research Institute Report No. 45215, DOE/NV/13609-45, 94 pp. plus 3 appendices.

Corey, A.T., 1954. The interrelation between gas and oil relative permeabilities. *Producer's Monthly*, Vol. XlX, No. 1, November, pp. 38-44.

Cumella, S.P. and D.B. Ostby, 2003. Geology of the Basin-Centered Gas Accumulation, Piceance Basin, Colorado, Denver. *In* Peterson, K., T. Olson, and D. Anderson (eds.), Piceance Basin 2003 Guidebook, Rocky Mountain Association of Geologists, Denver, Colorado, pp. 171-193.

Cussler, E.L., 1997. Diffusion Mass Transfer in Fluid Systems. 2nd edition, Cambridge University Press, 580 pp.

Dai, Z., R.W. Ritzi, Jr., and D.F. Dominic, 2005. Improving permeability semivariograms with transition probability models of hierarchical sedimentary architecture derived from outcrop analog studies, *Water Resour. Res*., 41, W07032, doi:10.1029/2004WR003515.

Dahlberg, E.C., 1995. Applied Hydrodynamics in Petroleum Exploration. Springer-Verlag, 295 pp.

DeGolyer and MacNaughton Co., 1971. Report on Interpretation of Test Data for Project Rulison in the Rulison Field, Garfield County, Colorado. Prepared for Austral Oil Company, Inc.

Dupuis, M., 1970. Distribution and evolution of radioelements after a nuclear explosion. Bull. Infor. Sci. Tech. 149. Lawrence Livermore National Laboratory, 1972, UCRL-Trans-10617-5.

Ferronsky and Polyakov, 1982, Environmental Isotopes in the Hydrosphere, John Wiley and Sons.

Frank, G.W., 1971. The nuclear stimulation of a natural gas reservoir – Project Rulison. World Petroleum Congress, 8(3), 355-363.

Frink, R.O. and J.A. Wethington, Jr., 1971. Tritium exchange between hydrocarbons and steam. Transactions of the American Nuclear Society, 1971 Winter Meeting, Miami Beach, pp. 467-468.

Furbish, D.J., 1997. Fluid Physics in Geology. Oxford Univ. Press. 476 pp.

Helton, J.C. and F.J. Davis, 2000. Sampling-based Methods. Saltelli, A., K. Chan, and E.M. Scott (eds.), Sensitivity Analysis, John Wiley, Hoboken, N.J. pp.101-152.

Hettinger, R.D. and M.A. Kirschbaum, 2002. Stratigraphy of the Upper Cretaceous Mancos Shale (Upper Part) and Mesaverde Group in the Southern Part of the Uinta and Piceance Basins, Utah and Colorado. U.S Geological Survey, Geologic Investigations Series I-2764, 21p.

Hill, J.H., 1971. Chemical Analysis of Preshot Rock from the Rulison Experiment. Lawrence Livermore Laboratory report UCID-15943, 13p.

Holzer, A., 1970. Gasbuggy in Perspective. American Nuclear Society, Proceedings of Symposium on Engineering with Nuclear Explosives 1:662-697.

Hubbert, M.K., 1953. Entrapment of petroleum under hydrodynamic conditions. *American Assoc. Petroleum Geol*., 37(8):1954-2026.

Iman, R.L. and W.J. Conover, 1982. A distribution-free approach to inducing rank correlation among input variables. *Commun. Statist.-Simula. Computa.*, 11(3), 311-334.

International Atomic Energy Agency (IAEA), 1998. The radiological situation at the atolls of Mururoa and Fangataufa. Technical Report in six volumes, Radiological assessment report series, Vienna, Austria.

Iuzzolino, H., 2003. Users Manual (Rev 00) for LHS, Version 2.51.uzz Civilian Radioactive Waste Management System Management and Operating Contractor, MOL.20040210.0391, Albuquerque, New Mexico

Jacobs, D.G., E.G. Struxness, and C.R. Bowman, 1970. A Preliminary Assessment of the Radiological Implications of Commercial Utilization of Natural Gas from a Nuclear Stimulated Well. American Nuclear Society, Proceedings of Symposium on Engineering with Nuclear Explosives 1:831-849.

Johnson, M.E., 1987. Multivariate Statistical Simulation, John Wiley and Sons, Inc., New York, 230p.

Johnson, R.C., M.P. Granica, and N.C. Dessenberger, 1979. Cross section B-B' of Upper Cretaceous and lower Tertiary rocks, southern Piceance Creek basin, Colorado: U.S. Geological Survey Miscellaneous Field Studies Map MF-1130-B, 2 sheets.

Johnson, R.C., 1989. Geologic History and Hydrocarbon Potential of Late Cretaceous-Age, Low-Permeability Reservoirs, Piceance Basin, Western Colorado. U.S. Geological Survey Bulletin 1787-E, 51p.

Johnson, R.C. and S.B. Roberts, 2003. The Mesaverde Total Petroleum System, Uinta-Piceance Province, Utah and Colorado. Chapter 7 of Petroleum Systems and Geologic Assessment of Oil and Gas in the Unita-Piceance Province, Utah and Colorado. U.S. Geological Survey Digital Data Series DDS-69-B, Version 1.0, 63p.

Koepsell, R., S.P. Cumella, and D. Uhl, 2003. Applications of Borehole Images in the Piceance Basin. Rocky Mountain Association of Geologists. *In* Peterson, K., T. Olson, and D. Anderson (Eds.), Piceance Basin 2003 Guidebook, Rocky Mountain Association of Geologists, Denver, Colorado, pp. 233-251.

Kukal, G.C. and K.E. Simons, 1986. Log analysis techniques for quantifying the permeability of submillidarcy sandstone reservoirs. *SPE Formation Evaluation*, 1(4):609-622.

Kuuskraa, V.A. and J. Ammer, 2004. Tight Gas Sands Development – How to Dramatically Improve Recovery Efficiency. *GasTIPS*, Gas Technology Institute, 10(1):15-20.

Law, B.E. and W.W. Dickinson, 1985. Conceptual model for origin of abnormally pressured gas accumulations in low-permeability reservoirs. *Am. Assoc. Petrol. Geologists Bull.*, 69(8):1295-1304.

Lerche, I. and R.O. Thomsen, 1994. Hydrodynamics of Oil and Gas. Plenum, 308 pp.

Lorenz, J.C., 1990. Reservoir Sedimentology of Rocks of the Mesaverde Group, Multiwell Experiment Site and East-Central Piceance Basin, Northwest Colorado. *In* Law, B.E. and C.W. Spencer (eds.), Geology of Tight Gas Reservoirs in the Pinedale Anticline area, Wyoming and the Multiwell Experiment Site, Colorado. U.S. Geological Survey Bulletin1886, Chapter K, pp.K-1 to K24.

Lorenz, J.C., 2003. Fracture Systems in the Piceance Basin: Overview and Comparison with Fractures in the San Juan and Green River Basins, Denver. *In* Peterson, K., T. Olson, and D. Anderson (eds.), Piceance Basin 2003 Guidebook, Rocky Mountain Association of Geologists, Denver, Colorado, pp. 75-94.

Lorenz, J.C., N.R. Warpinski, P.T. Branagan, and A.R. Sattler, 1989. Fracture characteristics and reservoir behavior of stress-sensitive fracture systems in flat-lying lenticular formations. *Journal of Petroleum Technology,* Vol. 41, pp.615-622.

Mahrer, K.D., 1999. A Review and perspective on far-field hydraulic fracture geometry studies. *Journal of Petroleum Science and Engineering*, 24(1):13-28.

Millington, R.J., 1959. Gas diffusion in porous media. *Science*, 130:100-102.

Millington, R.J. and J.P. Quirk, 1961. Permeability of porous solids. *Trans. Faraday Soc.*, 57:1200-1207.

Mills, R., 1973. Self-diffusion in normal and heavy water in the range 1-45º. *J. Physical Chem.*, 77(5):685-688.

Myal, F.R., E.H. Price, R.E. Hill, G.C. Kukal, P.A. Abadie, and C.C. Riecken, 1989. Geologic and Production Characteristics of the Tight Mesaverde Group: Piceance Basin, Colorado. U.S. Department of Energy, Office of Fossil Energy report DOE/MC/24120--2769, 126p.

Nelson, P.H., 2003. A Review of the Multiwell Experiment, Williams Fork and Iles Formations, Garfield County, Colorado, Chapter 15 of *Petroleum Systems and Geologic Assessment of Oil and Gas in the Uinta-Piceance Province, Utah and Colorado*, U.S. Geological Survey Digital Data Series DDS-69-B, 24p.

Nield, D.A., 1982. Onset of convection in a porous layer saturated by an ideal gas. *International Journal of Heat and Mass Transfer*, 25(10), 1605-1606.

Nield, D.A. and A. Bejan, 2006. Convection in Porous Media, 3rd edition. Springer, 640 pp.

Oldenburg, C.M. and K. Pruess, 2000. Simulation of propagating fronts in geothermal reservoirs with the implicit Leonard total variation diminishing scheme. *Geothermics* 29:1-25.

Parrington, J.R., H.D. Knox, S.L. Breneman, E.M. Baum and F. Feiner, 1996. Nuclides and Isotopes. Fifteenth Edition. General Electric Co., San Jose, CA, 64p.

Patterson, P.E., K. Kronmueller, and T.D. Davies, 2003. Sequence Stratigraphy of the Mesaverde Group and Ohio Creek Conglomerate, Northern Piceance Basin, Colorado, Denver. *In* Peterson, K., T. Olson, and D. Anderson (eds.), Piceance Basin 2003 Guidebook, Rocky Mountain Association of Geologists, Denver, Colorado, pp. 115-128.

Perry, R.H. and D.W. Green, 1997. Perry's Chemical Engineers' Handbook. McGraw-Hill, 7th edition.

Peterson, R.E. and J.B. Kohout, 1982. An Approximation of Continuity of Lenticular Mesaverde Sandstone Lenses, Utilizing Close Well Correlations, Piceance Basin, N.W. Colorado. U.S. Department of Energy, Bartlesville Energy Technology Center report DOE/NV 10249-3, 32p.

Phillips, W.S., J.T. Rutledge, L.S. House, and M.C. Fehler, 2002. Induced microearthquake patterns in hydrocarbon and geothermal reservoirs: Six case studies. *Pure and Applied Geophysics*, 159: 345-369.

Pruess, K., 1991. TOUGH2 – A General Purpose Numerical Simulator for Multiphase Fluid and Heat Flow. Lawrence Berkeley Laboratory Report LBL-29400, Berkeley, CA.

Pruess, K., 1995. Proceedings of the TOUGH Workshop '95. Lawrence Berkeley Laboratory Report LBL-37200, Berkeley, CA.

Pruess, K., 1998. Proceedings of the TOUGH Workshop '98. Lawrence Berkeley Laboratory Report LBNL-41995, CONF-980559, Berkeley, CA.

Pruess, K., C. Oldenburg and G. Moridis, 1999. TOUGH2 User's Guide, Version 2.0. Lawrence Berkeley Laboratory Report LBNL-43134, Berkeley, CA.

Pruess, K., 2002, Numerical simulation of multiphase tracer transport in fractured geothermal reservoirs, *Geothermics*, v. 31, pp. 475-499.

Quong, R., 1972. Permeability of Mesaverde Sandstone Samples: Project Rulison. Lawrence Livermore National Laboratories report UCID-16243, 7p.

Randolph, P.L., 1983. Porosity and permeability of Mesaverde sandstone core from the U.S. DOE Multiwell Experiment, Garfield County, Colorado. Proceedings paper SPE 11765 presented at the 1983 SPE/DOE Symposium on Low Permeability Gas Reservoirs, Denver, CO, March 4-6, 1983, pp.449-460.

Reeves, S.R., D.G. Hill, R.L. Tiner, P.A. Bastian, M.W. Conway, and S. Mohaghegh, 1999. Restimulation of Tight Gas Sand Wells in the Rocky Mountain Region. Society of Petroleum Engineers paper SPE 55627, proceedings paper presented at the 1999 SPE Rocky Mountain Regional Meeting, Gillette, WY, 16p.

Reid, R.C., J.M. Prausnitz, and B.E. Poling, 1987. The Properties of Gases and Liquids, McGraw Hill, 741 pp.

Reynolds, M., B.G. Bray, and R.L. Mann, 1970. Project Rulison: A Status Report. Society of Petroleum Engineers paper SPE 3191, proceedings paper presented at the 1970 Eastern Regional Meeting, Pittsburgh, PA, 16p.

Reynolds Jr., M., 1971. Project Rulison - Summary of Results and Analyses. Presented at American Nuclear Society Winter Meeting, Miami Florida, October 1971, 23p.

Robison, W.L., and L.R. Anspaugh, 1969, Assessment of Potential Biological Hazards from Project Rulison. Lawrence Livermore National Laboratory, UCRL-50791.

Rogers, L. and M. Reynolds, Jr., 1972. Summary of Project Rulison. Unnumbered report prepared by El Paso Natural Gas and Austral Oil Company, in U.S. DOE/NV Technical Information Resource Center, 6p.

Rubin, B., L. Schwartz, and D. Montan, 1972. An Analysis of Gas Stimulation Using Nuclear Explosives. Lawrence Livermore Laboratory Report UCRL-51226, 68p.

Rutledge, J.T. and W.S. Phillips, 2003. Case History: Hydraulic stimulation of natural fractures as revealed by induced micro-earthquakes, Carthage Cotton Valley gas field, east Texas. *Geophysics*, 68(2):441-452.

Sandia National Laboratories and CER Corporation, 1989. Multiwell Experiment Final Report: III. The Coastal Interval of the Mesaverde Formation. Sandia National Laboratories Report SAND88-3284, variable paging.

Sandia National Laboratories and CER Corporation, 1990. Multiwell Experiment Final Report: IV. The Fluvial Interval of the Mesaverde Formation. Sandia National Laboratories Report SAND89-2612/A, 468 pp.

Sharma, M.M., P.B. Gadde, D. Copeland, R. Sigal, R. Fielder, and R. Sullivan, 2003. The impact of propant placement on the productivity of tight gas wells. *GasTIPS*, 9(4):19-24.

Slattery, M.W., 1993. Exchange of oxygen and hydrogen isotopes between water and water vapor: experimental results. University of Nevada, Las Vegas, Masters Thesis, 121 p.

Smith, C.F. Jr., 1971. Gas analysis results for Project Rulison production testing samples. Lawrence Livermore Laboratory report UCRL-51153, 25p.

Smith, C. F., 1975. Rio Blanco Gas Composition LLL Data Summary Calibration and Production Testing of RB-AR-02. Lawrence Livermore National Laboratory Report UCID-16762.

Smith, D.K., B.K. Esser, and J.L. Thompson, 1995. Uncertainties Associated with the Definition of a Hydrologic Source Term for the Nevada Test Site. Lawrence Livermore National Laboratory Report UCRL-ID-120322, 21p.

Soeder, D.J. and P.L. Randolph, 1987. Porosity, permeability, and pore structure of the tight Mesaverde Sandstone, Piceance Basin, Colorado. *SPE Formation Evaluation* 2(3):129-136.

Tompson, A. F. B., C. J. Bruton, and G.A. Pawloski, 1999. Evaluation of the Hydrologic Source Term from Underground Nuclear Tests in Frenchman Flat at the Nevada Test Site: The Cambric Test, Lawrence Livermore National Laboratory Report UCRL-ID-132300, 319 pp.

Toman, J. and H.A. Tewes, 1972. Project Rio Blanco: Phase I Technical Studies. Lawrence Livermore Laboratory Report UCID-15968, 138 pp.

U.S. Atomic Energy Commission (AEC), 1972a. Project Rulison Final Operational Radioactivity Report Production Tests. Nevada Operations Office Report NVO-112, PNE-R-57, 71p.

U.S. Atomic Energy Commission (AEC), 1972b. Environmental Statement ~~Project~~ Rio Blanco Gas Stimulation Project, Rio Blanco County, Colorado. Nevada Operations Office, PNE-RB-1, WASH-1519, variable paging.

U.S. Atomic Energy Commission (AEC), 1973a. Rulison Site Cleanup Report. Nevada Operations Office Report NVO-136, 21p.

U.S. Atomic Energy Commission (AEC), 1973b. Project Rulison: Managers Report. Nevada Operations Office report NVO-71, PNE-R-63, 247p.

U.S. Department of Energy (DOE), 1984. Long-term Hydrologic Monitoring Program Rulison Event Site Grand Valley, Colorado. Nevada Operations Office Report NVO-273, 25p.

U.S. Department of Energy (DOE), 2000a. United States Nuclear Tests, July 1945 through September 1992, DOE/NV209 REV-15, 162p.

U.S. Department of Energy (DOE), 2000b. Site Characterization Work Plan for the Rio Blanco Site, Colorado. Nevada Operations Office report DOE/NV-607, 59p.

U.S. Department of Energy (DOE), 2005. Rulison site environmental management end state vision, Report DOE/NV-95 (www.nv.doe.gov/library/publications/Environmental/DOENV_950.pdf).

U.S. Energy Research and Development Agency (ERDA), 1977. Project Rulison Well Plugging and Site Abandonment Final Report. Nevada Operations Office Report NVO-187, PNE-R-70, variable paging.

U.S. Environmental Protection Agency (EPA), 1992. Offsite Environmental Monitoring Report: Radiation Monitoring Around United States Nuclear Test Areas Calendar Year 1990. EPA 600/4-91/030, 171p.

Verbeek, E.R. and M.A. Grout, 1997. Relation between Basement Structures and Fractured Systems in Cover Rocks, Northeastern and Southwestern Colorado Plateau. *In* Friedman, J.D. and A.C. Huffman (eds.), Laccolith Complexes of Southeastern Utah: Time of Emplacement and Tectonic Setting – Workshop Proceedings. U.S. Geological Survey Bulletin 2158, pp.111-149.

Voegeli, P.T.S., and S.W. West, 1970. Geohydrology: Project Rulison, Garfield County, Colorado. U.S. Geological Survey Report USGS-474-68, Rulison-5, 52p.

Wang, J.S.Y. and T.N. Narashimhan, 1985. Hydrologic mechanisms governing fluid flow in a partially saturated, fractured, porous medium, *Water Resources Research*, 21:1861-1874.

Warpinski, N.R., T.B. Wright, J.E. Uhl, B.P. Engler, P.M. Drozda, R.E. Peterson, and P.T. Branagan**,** 1996. Micro-seismic monitoring of the B-sand hydraulic fracture experiment at the DOE/GRI multi-site project. SPE Paper 36450, proceedings paper presented at the 1996 SPE Annual Technical Conference and Exhibition, Denver, CO, 9p.

Warpinski, N.R., P.T. Branagan, R.E. Peterson, J.E. Fix, J.E. Uhl, B.P. Engler, and R. Wilmer, 1997. Micro-seismic and deformation imaging of hydraulic fracture growth and geometry in the C-sand interval, GRI/DOE M-site project. SPE Paper 38573, proceedings paper presented at the 1997 SPE Annual Technical Conference and Exhibition, San Antonio, TX, 12p.

Wethington, J.A. Jr., 1970. Possible techniques for decontamination of natural gas from gas wells stimulated by a nuclear explosion. *In* American Nuclear Society and U.S. Atomic Energy Agency, Proceedings from Symposium on Engineering with Nuclear Explosives, Las Vegas, Nevada, CONF-700101, Vol. 2., pp.1589-1596

Weissmann, G.S., S.F. Varle, and G.E. Fogg, 1999. Three-dimensional hydrofacies modeling based on soil surveys and transition probability geostatistics, *Water Resources Research*, 35(6): 1761-1770.

Zheng, C., and G.D. Bennett. 2002. Applied Contaminant Transport Modeling, 2nd edition, Wiley-Interscience, 621 pp.

APPENDIX: TOUGH2 V2.0 Governing Equations

The two fluid phases are gas (water vapor and air) and liquid water. As little is known of the thermodynamic properties of the gas mixtures at the three nuclear-stimulation sites, the gas phase was left as air instead of replacing it with methane properties. The governing mass and heat transport equations are

$$\frac{d}{dt}\int_{V_n} M^\kappa dV_n = \int_{\Gamma_n} \mathbf{F}^\kappa \cdot \mathbf{n} d\Gamma_n + \int_{V_n} q^\kappa dV_n \tag{A1}$$

where the integration is over the domain of the flow system, V_n, which is bounded by the closed surface Γ_n. The quantity M that appears in the accumulation term represents mass or energy per unit volume, where the components (mass and/or heat) are labeled by κ (κ=1 water, κ=2 air, κ=3 heat). **F** denotes mass or heat flux, and q denotes sources and sinks. The normal vector **n** on the surface $d\Gamma_n$ points inward into V_n.

The mass accumulation term is

$$M^\kappa = \phi \sum_\beta S_\beta \rho_\beta X_\beta{}^\kappa \tag{A2}$$

The total mass of component κ is obtained by summing over the fluid phases β (liquid, gas). φ is porosity, S_β is saturation of phase β, ρ_β is the density of phase β, and $X_\beta{}^\kappa$ is the mass fraction of component κ in phase β. The heat accumulation term is

$$M^3 = (1-\phi)\rho_r C_r T + \phi \sum_\beta S_\beta \rho_\beta u_\beta \tag{A3}$$

where ρ_r is the grain density of the porous medium, C_r is the specific heat of the rock, T is temperature, and u_β is the internal energy of phase β.

Mass flux terms are summed over the two mobile phases,

$$\mathbf{F}^\kappa = \sum_\beta X_\beta{}^\kappa \mathbf{F}_\beta{}^\kappa \tag{A4}$$

and the flux of each phase is modeled by the multiphase version of Darcy's law

$$\mathbf{F}_\beta = \rho_\beta \mathbf{u}_\beta = -k \frac{k_{r\beta}\rho_\beta}{\mu_\beta}\left(\nabla P_\beta + \rho_\beta \mathbf{g}\right) \tag{A5}$$

Here, $\mathbf{u}_\beta$ is the Darcy velocity of phase β, k is absolute permeability, $k_{r\beta}$ is the relative permeability to phase β, μ_β is the dynamic viscosity of phase β, and ∇P_β is the pressure gradient across phase β.

Heat flux (conduction and convection) is

$$\mathbf{F}^3 = -\lambda \nabla T + \sum_\beta h_\beta \mathbf{F}_\beta \tag{A6}$$

where λ is thermal conductivity, and h_β is the specific enthalpy of phase β.

Mass diffusion for both solutes and gases is modeled with Fick's law

$$\mathbf{f}_{\beta}^{\kappa} = -\phi\tau_0\tau_\beta\rho_\beta D_\beta^{\kappa}\nabla X_\beta^{\kappa} \tag{A7}$$

where $\mathbf{f}_{\beta}^{\kappa}$ is the mass flux of component κ in phase β, ϕ is porosity, τ_0 is a tortuosity parameter dependent upon pore geometry, τ_β is a tortuosity parameter dependent upon phase saturation, D_β^{κ} is the diffusion coefficient of component κ in phase β, and X_β^{κ} is the mass fraction of component κ in phase β. The hydrodynamic dispersion module available in TOUGH2 was not implemented in these simulations; there are no data on dispersivities, and since properties of the fractures themselves are largely unknown, dispersion would only contribute to uncertainty. Fortunately, the primary interest is in radionuclide transport in the gas phase, and unlike the case for liquids, mass flux due to gas diffusion in porous media and fractures is more important than gas dispersion. This is explained in the text using a scale analysis.